UNIVERSITY OF OKLAHOMA

GRADUATE COLLEGE

CYLINDRICAL POLARIMETRIC PHASED ARRAY RADAR DEMONSTRATOR: PERFORMANCE ASSESSMENT AND WEATHER MEASUREMENTS

A DISSERTATION

SUBMITTED TO THE GRADUATE FACULTY

in partial fulfillment of the requirements for the

Degree of

DOCTOR OF PHILOSOPHY

By

ZHE LI
Norman, Oklahoma
2020

CYLINDRICAL POLARIMETRIC PHASED ARRAY RADAR DEMONSTRATOR: PERFORMANCE ASSESSMENT AND WEATHER MEASUREMENTS

A DISSERTATION APPROVED FOR THE
SCHOOL OF ELECTRICAL AND COMPUTER ENGINEERING

BY THE COMMITTEE CONSISTING OF

Dr. Guifu Zhang, Chair

Dr. Yan (Rockee) Zhang, Co-Chair

Dr. Hjalti Sigmarsson

Dr. Dusan Zrnić

Dr. Meijun Zhu

Acknowledgments

First, I would like to express my sincere gratitude to my advisors, Dr. Guifu Zhang and Dr. Yan (Rockee) Zhang, for providing guidance and support throughout my Ph.D. studies. I have benefited a lot from their valuable experience and broad knowledge. Their insightful suggestions and encouragement help me persist with my research and get over difficulties encountered along the way. Besides, their rigorous scientific attitude and hard-working spirit have set a good example for me, and their kind instructions will be seared into my memory forever.

I would also like to thank all my Ph.D. committee members, Dr. Dusan Zrnić, Dr. Hjalti Sigmarsson, and Dr. Meijun Zhu, for taking their time to review my dissertation and providing me with insightful suggestions carefully. Especially, I wish to express my sincere thanks to Dr. Richard Doviak and Dr. Dusan Zrnić for their guidance and support on phased array radar system simulator. In addition, I want to extend my appreciation to Matthew Herndon for numerous discussions on the CPPAR radar control software, as well as all the members of the Advanced Radar Research Center, for their help in all respects during my Ph.D. studies. Also, thanks to the National Oceanic and Atmospheric Administration (NOAA) which provides funding support to my Ph.D. studies.

Finally, I would like to express my deep gratitude to my parents for their unconditional support and love. Their care and encouragement make all these possible. Especially, I would like to give my most gracious gratitude to my wife, Jane, who has constantly been supportive and patient throughout my Ph.D. studies.

Table of Contents

Acknowledgments....iv
List of Tables....vii
List of Figures....viii
Abstract....xiii
Chapter 1 Introduction....1
1.1 Overview of Phased Array Weather Radar....1
1.2 Planar Polarimetric Phased Array Radar....3
1.3 Cylindrical Polarimetric Phased Array Radar....5
1.4 Outline of the Dissertation....7
Chapter 2 CPPAR System Description....10
2.1 System Overview....10
2.2 Waveform Design and Measurement....12
2.3 Pattern Optimization and Measurement....13
2.4 System Calibration....16
2.4.1 Calibration with an External Source....16
2.4.2 Calibration with Weather Measurements of Mechanical Scan....19
2.4.3 Calibration using Ground Clutter Returns....23
Chapter 3 System Simulation for Performance Evaluation....28
3.1 Introduction....28
3.2 Simulation Framework....31
3.3 Weather Returns Modeling....35
3.3.1 Monte Carlo Method....35
3.3.2 Covariance Matrix Method....37
3.4 Antenna Pattern....39
3.5 Channel Electronics Modeling....42
3.6 Simulation Results....44
3.6.1 CPPAR System....44
3.6.2 PPPAR System....51
3.7 Limitations and Future Work of PASIM....54
Chapter 4 Weather Measurements and Performance Evaluation with the CPPAR....56

4.1 Data Collection and Scan Mode 56
4.2 Weather Measurements 58
4.2.1 Case 1: Stratiform/Convective Multicell Storms 58
4.2.2 Case 2: Severe Thunderstorms 63
4.2.3 Case 3: Stratiform Precipitation 67
Chapter 5 Clutter Detection with the CPPAR 71
5.1 Introduction 71
5.2 Clutter Characteristics in Electronic Scan 73
5.3 Clutter Detection with the CPPAR 78
5.3.1 Data Sets 78
5.3.2 Discriminant Function and Simple Bayesian Classifier 79
5.3.3 Clutter Detection Using Electronic Scan Data 82
5.3.4 Clutter Detection Using Mechanical Scan Data 98
Chapter 6 Conclusions and Future Work 113
6.1 Conclusions 113
6.2 Future Work 115
References 117

List of Tables

Table 2-1 Technical specifications of the CPPAR demonstrator 11
Table 3-1 Technical specifications of the simulated CPPAR 47
Table 3-2 Assumed values for uniform weather truth fields 47
Table 3-3 Technical specifications of the simulated TPD 52
Table 4-1 CPPAR parameters during data collection 57
Table 4-2 NEXRAD specifications for data quality 58
Table 4-3 Error statistics of CPPAR measurements based on comparison between electronic and mechanical scans 62
Table 4-4 Error statistics of CPPAR measurements based on comparison between electronic and mechanical scans 65
Table 4-5 Error statistics of CPPAR measurements based on comparison between electronic and mechanical scans 69
Table 5-1 The number of TP, FN, FP, TN, POD, PFA, and CSI at various lags with electronic scan in convective precipitation 91
Table 5-2 The number of TP, FN, FP, TN, POD, PFA, and CSI at various lags with electronic scan in stratiform precipitation 98
Table 5-3 The number of TP, FN, FP, TN, POD, PFA, and CSI at various lags with mechanical scan in convective precipitation 105
Table 5-4 The number of TP, FN, FP, TN, POD, PFA, and CSI at various lags with mechanical scan in stratiform precipitation 112

List of Figures

Figure 1-1 Pictures of PPARs. (a) CASA Phase-Tilt Radar. (b) PAWR at Osaka University. (c) NSSL Ten Panel Demonstrator. (d) NSSL Advanced Technology Demonstrator. (e) OU-NSSL CPPAR Demonstrator Version 1. (f) OU-NSSL CPPAR Demonstrator Version 2. 9
Figure 2-1 CPPAR demonstrator. (a) On the ground. (b) On the rooftop of Radar Innovations Laboratory. 11
Figure 2-2 The simplified functional block diagram of the CPPAR demonstrator. 11
Figure 2-3 NLFM waveform in CPPAR. (a) The real component of the designed waveform. (b) Autocorrelation function of the designed waveform. (c) The spectrum of measured waveform. (d) Autocorrelation function of measured waveform. 13
Figure 2-4 Relative positions of the CPPAR (within the red circle on the left) and the far-field horn (within the red circle on the right). 14
Figure 2-5 Normalized power and phase of the calibration offset and beamforming weights in the CPPAR. (a) Normalized power of the calibration offset. (b) Phase of the calibration offset. (c) Normalized amplitude of the beamforming weights. (d) Phase of the beamforming weights. 15
Figure 2-6 Optimized array radiation patterns of the CPPAR. 15
Figure 2-7 CPPAR calibration with an external source (CPPAR transmit pattern). (a) Measured and fitted one-way beam patterns. (b) Estimated 3-dB beamwidth. (c) Estimated system gain. (d) Estimated phase. (e) Mean differences for Z_H, Z_{DR}, and ϕ_{DP}. (f) Gain and beamwidth contribution to Z_H difference. 17
Figure 2-8 CPPAR calibration with an external source (CPPAR receive pattern). (a) Measured and fitted one-way beam patterns. (b) Estimated 3-dB beamwidth. (c) Estimated system gain. (d) Estimated phase. (e) Mean differences for Z_H, Z_{DR}, and ϕ_{DP}. (f) Gain and beamwidth contribution to Z_H difference. 18
Figure 2-9 The sensitivity of CPPAR as a function of range measured in various weather conditions. (a) Reflectivity measured by CPPAR on a rainy day. (b) CPPAR sensitivity as a function of range on a rainy day. (c) Reflectivity measured by CPPAR on a clear air day. (d) CPPAR sensitivity as a function of range on a clear air day. 21
Figure 2-10 CPPAR calibration by single-beam weather measurements. Left column: measurements of CPPAR mechanical scan; middle column: measurements of CPPAR electronic scan; right column: the difference between electronic scan and mechanical scan of the CPPAR. 23
Figure 2-11 Mean differences between electronic scan and mechanical scan for CPPAR calibration. 23
Figure 2-12 CPPAR calibration by clutter. (a) Clutter in reflectivity plot measured by CPPAR. (b) Radial profiles of reflectivity for 25 beams. (c) Image of the ground clutter structure from Google Maps. (d) Image of the ground clutter structure in Apple Maps. (e) Measured and fitted two-way beam patterns. (f) Beam-to-beam mean differences for Z_H, Z_{DR}, and ϕ_{DP} 25
Figure 2-13 Averaged beam-to-beam variations for Z_H, Z_{DR}, and ϕ_{DP} obtained with various calibration methods. (a) Mean Z_H difference. (b) Mean Z_{DR} difference. (c) Mean

ϕ_{DP} difference. 26
Figure 3-1 The role of radar system simulation. 29
Figure 3-2 The framework of PASIM. 33
Figure 3-3 Operations of the key modules of PASIM. (a) Time-domain system simulation. (b) Weather radar data quality prediction. 35
Figure 3-4 The 3D antenna radiating element in PASIM. (a) Copolar component. (b) Cross-polar component. 40
Figure 3-5 Normalized one-way element patterns for a patch antenna radiating element. (a) H copolar power pattern. (b) H cross-polar power pattern. (c) V cross-polar power pattern. (d) V copolar power pattern. (e) H copolar phase pattern. (f) H cross-polar phase pattern. (g) V cross-polar phase pattern. (h) V copolar phase pattern. 41
Figure 3-6 The impact of Saleh nonlinearity model of HPA on an LFM waveform and matched filter output. (a) Waveform envelope with and without nonlinear distortion. (b) Matched filter output with and without nonlinear distortion. (c) Amplitude and phase transfer function. 43
Figure 3-7 The simulated CPPAR beam patterns. (a) Without quantization error. (b) With quantization error based on 5-bit phase shifters. 44
Figure 3-8 The simulated CPPAR and beam patterns. (a) CPPAR cylinder. (b) Element patterns in elevation=0 degrees plane. (c) Element patterns in elevation=7 degrees plane. (d) Beam patterns in elevation=0 degrees plane. (e) Beam patterns in elevation=7 degrees plane. 46
Figure 3-9 Theoretical and simulated polarimetric biases with CPPAR in observation of idealized uniform weather truth fields. The beam was steered 0 degrees (left column) and 7 degrees (right column) in elevation and ±45 degrees in azimuth with a step of 3.75 degrees. (a), (b) Z_{DR}. (c), (d) ρ_{hv}. (e), (f) ϕ_{DP}. 48
Figure 3-10 Reflectivity observed by KTLX at 04:33:45 UTC on May 19th, 2013. . 49
Figure 3-11 Comparison of NEXRAD weather truth fields (left column), and simulated polarimetric radar estimates with CPPAR (middle column) and TPD (right column). 50
Figure 3-12 The simulated TPD and beam patterns. (a) TPD planar array. (b) Beam patterns in elevation=0 degrees plane. (c) Beam patterns in elevation=7 degrees plane. 52
Figure 3-13 Theoretical, simulated, and measured polarimetric biases with TPD in a stratiform precipitation. The beam was steered 0 degrees (left column) and 7 degrees (right column) in elevation and ±45 degrees in azimuth with a step of 3 degrees. (a), (b) Z_{DR}. (c), (d) ρ_{hv}. (e), (f) ϕ_{DP}. 53
Figure 4-1 Reflectivity observed by KTLX at 05:06:10 UTC on 27 August 2019. ... 58
Figure 4-2 Weather measurements collected with CPPAR (SNR ≥ 5 dB) and KTLX on 27 August 2019. Left column: CPPAR mechanical scan at 05:03:40 UTC; middle column: CPPAR electronic scan at 05:04:04 UTC; right column: KTLX mechanical scan at 05:06:10 UTC. 59
Figure 4-3 Scatter plots of CPPAR measurements of precipitation (SNR ≥ 5 dB). 60
Figure 4-4 Histograms of STD of radar estimates in electronic scan (SNR ≥ 20 dB). 62
Figure 4-5 Reflectivity observed by KTLX at 06:48:37 UTC on 8 May 2020. 63

Figure 4-6 Weather measurements collected with CPPAR (SNR ≥ 5 dB) and KTLX on 8 May 2020. Left column: CPPAR mechanical scan at 06:50:21 UTC; middle column: CPPAR electronic scan at 06:50:54 UTC; right column: KTLX mechanical scan at 06:48:37 UTC. 64
Figure 4-7 Scatter plots of CPPAR measurements of precipitation (SNR ≥ 5 dB)..... 65
Figure 4-8 Histograms of STD of radar estimates in electronic scan (SNR ≥ 20 dB). 65
Figure 4-9 Hydrometeor Classification product of KTLX at 06:48:37 UTC on 8 May 2020..... 66
Figure 4-10 Reflectivity observed by KTLX at 20:33:52 UTC on 25 May 2020. 67
Figure 4-11 Weather measurements collected with CPPAR (SNR ≥ 5 dB) and KTLX on 25 May 2020. Left column: CPPAR mechanical scan at 20:30:40 UTC; middle column: CPPAR electronic scan at 20:31:04 UTC; right column: KTLX mechanical scan at 20:33:52 UTC. 68
Figure 4-12 Scatter plots of CPPAR measurements of precipitation (SNR ≥ 5 dB)... 69
Figure 4-13 Histograms of STD of radar estimates in electronic scan (SNR ≥ 10 dB). 69
Figure 5-1 An illustration of changing differential scattering phase in the continuous mechanical scan. 75
Figure 5-2 Comparison of ρ_{hv} under various scan modes in clear air condition. (a) Mechanical scan with single radial. (b) Mechanical scan with combined radials. (c) Electronic scan..... 76
Figure 5-3 Measured ρ_{hv} and histogram in clear air conditions with mechanical scan at 23:00:20 UTC on 17 May 2020 and electronic scan at 22:57:40 UTC on 17 May 2020. (a) ρ_{hv} in mechanical scan. (b) ρ_{hv} in electronic scan. (c) Histogram of ρ_{hv} in mechanical scan. (d) Histogram of ρ_{hv} in electronic scan. 77
Figure 5-4 Clutter measurements with electronic scan at 15:43:08 UTC on 9 May 2020. 83
Figure 5-5 Weather measurements with electronic scan at 18:55:22 UTC on 15 May 2020..... 83
Figure 5-6 Combined clutter and weather measurements with electronic scan..... 84
Figure 5-7 Scatter plots of PSF_h and PSF_v at multiple lags for the measurements in Figure 5-4 and Figure 5-5. (a) Lag=1. (b) Lag=2. (c) Lag=3. (d) Lag=4. 84
Figure 5-8 The joint conditional probability density functions of PSF_h and PSF_v given clutter (left column) and weather (right column) with electronic scan. Figures from top to bottom rows refer to the lag of 1, 2, 3, and 4 respectively..... 86
Figure 5-9 The conditional probability density functions with electronic scan. (a) The conditional probability density function of Z_{DR} given clutter and weather. (b) The joint conditional probability density function of ρ_{12} and ρ_{hv} given clutter. (c) The joint conditional probability density function of ρ_{12} and ρ_{hv} given weather. 87
Figure 5-10 Detected clutter maps obtained using SBC with electronic scan. (a) Lag=1. (b) Lag=2. (c) Lag=3. (d) Lag=4. (e) Ground truth clutter map. 90
Figure 5-11 POD as a function of CSR with electronic scan. (a) Lag=1. (b) Lag=2. (c) Lag=3. (d) Lag=4. 91

Figure 5-12 Clutter measurements with electronic scan at 22:04:19 UTC on 30 May 2020.....92
Figure 5-13 Weather measurements with electronic scan at 20:33:38 UTC on 25 May 2020.....92
Figure 5-14 Combined clutter and weather measurements with electronic scan.....93
Figure 5-15 Scatter plots of PSF_h and PSF_v at multiple lags for the measurements in Figure 5-12 and Figure 5-13. (a) Lag=1. (b) Lag=2. (c) Lag=3. (d) Lag=4. 93
Figure 5-16 The joint conditional probability density functions of PSF_h and PSF_v given clutter (left column) and weather (right column) with electronic scan. Figures from top to bottom rows refer to the lag of 1, 2, 3, and 4 respectively.....95
Figure 5-17 The conditional probability density functions with electronic scan. (a) The conditional probability density function of Z_{DR} given clutter and weather. (b) The joint conditional probability density function of ρ_{12} and ρ_{hv} given clutter. (c) The joint conditional probability density function of ρ_{12} and ρ_{hv} given weather. 96
Figure 5-18 Detected clutter maps obtained using SBC with electronic scan. (a) Lag=1. (b) Lag=2. (c) Lag=3. (d) Lag=4. (e) Ground truth clutter map. 97
Figure 5-19 Clutter measurements with mechanical scan at 23:00:20 UTC on 17 May 2020.....99
Figure 5-20 Weather measurements with mechanical scan at 18:56:43 UTC on 15 May 2020.....99
Figure 5-21 Combined clutter and weather measurements with mechanical scan. ..100
Figure 5-22 Scatter plots of PSF_h and PSF_v at multiple lags for the measurements in Figure 5-19 and Figure 5-20. (a) Lag=1. (b) Lag=2. (c) Lag=3. (d) Lag=4. 100
Figure 5-23 The joint conditional probability density functions of PSF_h and PSF_v given clutter (left column) and weather (right column) with mechanical scan. Figures from top to bottom rows refer to the lag of 1, 2, 3, and 4 respectively.....102
Figure 5-24 The conditional probability density functions with mechanical scan. (a) The conditional probability density function of Z_{DR} given clutter and weather. (b) The joint conditional probability density function of ρ_{12} and ρ_{hv} given clutter. (c) The joint conditional probability density function of ρ_{12} and ρ_{hv} given weather. 103
Figure 5-25 Detected clutter maps obtained using SBC with mechanical scan. (a) Lag=1. (b) Lag=2. (c) Lag=3. (d) Lag=4. (e) Ground truth clutter map. 104
Figure 5-26 POD as a function of CSR with mechanical scan. (a) Lag=1. (b) Lag=2. (c) Lag=3. (d) Lag=4. 105
Figure 5-27 Clutter measurements with mechanical scan at 22:05:51 UTC on 30 May 2020.....106
Figure 5-28 Weather measurements with mechanical scan at 20:35:51 UTC on 25 May 2020.....106
Figure 5-29 Combined clutter and weather measurements with mechanical scan. ..107
Figure 5-30 Scatter plots of PSF_h and PSF_v at multiple lags for the measurements in Figure 5-27 and Figure 5-28. (a) Lag=1. (b) Lag=2. (c) Lag=3. (d) Lag=4. 107
Figure 5-31 The joint conditional probability density functions of PSF_h and PSF_v given clutter (left column) and weather (right column) with mechanical scan. Figures from top to bottom rows refer to the lag of 1, 2, 3, and 4 respectively.....109

Figure 5-32 The conditional probability density functions with mechanical scan. (a) The conditional probability density function of Z_{DR} given clutter and weather. (b) The joint conditional probability density function of ρ_{12} and ρ_{hv} given clutter. (c) The joint conditional probability density function of ρ_{12} and ρ_{hv} given weather. 110
Figure 5-33 Detected clutter maps obtained using SBC with mechanical scan. (a) Lag=1. (b) Lag=2. (c) Lag=3. (d) Lag=4. (e) Ground truth clutter map. 111

Abstract

A desirable candidate for future weather observation is a polarimetric phased array radar (PPAR), which is capable of both using polarimetry for multi-parameter measurements and the fast-scan proficiency of the PAR. However, it is challenging to collect high-quality polarimetric radar data of weather with a planar PPAR (PPPAR), whose beam and polarization characteristics change with the electronic beam direction, causing geometrically induced cross-polarization coupling, sensitivity losses, and measurement biases when the PPPAR beam is steered away from the broadside.

As an alternative to PPPAR, the concept of cylindrical polarimetric phased array radar (CPPAR) was proposed, which has scan-invariant beam characteristics in azimuth and polarization purity in all directions using commutating scan, thus enables high quality polarimetric weather measurements. To validate the CPPAR concept, a small-scale CPPAR demonstrator has been jointly developed by the Advanced Radar Research Center (ARRC) at the University of Oklahoma (OU) and the National Severe Storms Laboratory (NSSL) of NOAA.

This dissertation presents the results of initial weather measurements, shows the performance of the CPPAR demonstrator, and evaluates the polarimetric data quality that has been achieved. The system specifications and field tests of the CPPAR demonstrator are provided, including system overview, waveform design and verification, pattern optimization and far-field tests. In addition, three methods of system calibration are introduced and compared, including calibration with an external source, calibration with weather measurements of mechanical scan, and calibration with

ground clutter. It is found that calibration with weather measurements of mechanical scan has the best performance and it is applied on the CPPAR demonstrator for the first time, which effectively improved the beam-to-beam consistency and radar data quality in commutating beam electronic scan by minimizing gain and beamwidth variations.

Performance of the CPPAR is assessed through system simulation and weather measurements. The CPPAR is evaluated through an end-to-end phased array radar system simulator (PASIM). The simulation framework, weather returns modeling, antenna pattern, channel electronics, and simulation results of CPPAR, as well as comparison with those that would be obtained with a PPPAR, are provided. Also, weather measurements of a few convective precipitation cases and a stratiform precipitation case made with the CPPAR, employing the single beam mechanical scan and commutating beam electronic scan respectively, are presented. First, a qualitative comparison is made between the CPPAR and a nearby operational NEXRAD. Then a quantitative comparison is conducted between the mechanical scan and electronic scan, and error statistics are estimated and discussed. In addition, a theoretical explanation of a feature of the commutating beam electronic scan in clutter detection that is different from mechanical scan is presented and verified by measurements in clear air conditions with the CPPAR. Moreover, clutter detection results based on multi-lag phase structure function, dual-scan cross-correlation coefficient, copolar correlation coefficient, and differential reflectivity obtained from both electronic scan and mechanical scan modes of the CPPAR are compared.

Chapter 1 Introduction

1.1 Overview of Phased Array Weather Radar

In the past few decades, weather radar has been playing an important role in weather observation, forecasting, and warning. A traditional single-polarization Doppler weather radar can measure the reflectivity factor (Z_{H}), radial velocity (v_{r}), and spectrum width (σ_{v}), which are referred to as spectral moments [1]. Specifically, Z_{H} is proportional to the backscattering cross-section per unit volume and provides microphysics information about the weather scatterers in each resolution volume. v_{r} and σ_{v} represent the mean and standard deviation (to which shear and turbulence contribute) of the radial velocity of scatterers in motion, respectively [2-3]. Later it was found that these radar spectral moments were not sufficient to characterize the hydrometeor particles in terms of shapes, sizes, orientations, and phase composition. Therefore, weather radar polarimetry, which could be realized with polarization diversity [1-4], was introduced as a solution to provide more detailed microphysical information of the cloud and precipitation [5-7].

In addition to the radar spectral moments mentioned above, a polarimetric radar can provide further measurements, such as differential reflectivity (Z_{DR}), copolar correlation coefficient (ρ_{hv}), and differential phase (ϕ_{DP}), which are called polarimetric variables [2-3]. Specifically, Z_{DR} refers to the ratio of reflectivity at horizontal and vertical polarizations. Within the Rayleigh regime, Z_{DR} tends to increase for more oblate scatterers. ρ_{hv} reflects the similarity of returned signals between the horizontal and vertical polarizations, which tends to reduce when there is increased

randomness, diversity, and non-Rayleigh scattering of weather scatterers in the resolution volume. ϕ_{DP} is the difference in phase shift between the horizontal and vertical polarization signals, which increases rapidly in heavy rain comprised of oblate scatterers, where the horizontally polarized wave propagates slower than the vertically polarized wave [8]. These three polarimetric variables can be obtained with a radar working in simultaneous transmission and simultaneous reception (STSR) mode, which is widely used in operational weather radars worldwide owing to its several technical advantages and practical considerations [9]. Since 2013, with the polarimetric upgrade of operational Next-Generation Weather Radar (NEXRAD) in the United States, weather radar polarimetry with multi-parameter measurements has matured in applications such as quantitative precipitation estimation, hydrometeor classification, melting layer detection, attenuation correction, microphysics retrieval, etc.

While radar polarimetry provides more microphysical information about the weather scatterers, there is an increasing need for faster data updates [10]. Currently, the NEXRAD radar (with a mechanically scanning dish antenna) takes about 5 minutes to complete a volumetric scan, which is too slow to detect and issue warnings in advance for fast-evolving severe weather such as tornadoes and downbursts lasting for only a few minutes [2]. For better detection of evolutions of such severe weather phenomena in a timely manner, weather radar data with a higher temporal resolution (i.e., less than 1 minute) are desired. In recent years, phased array radar (PAR) with an agile beam that steers electronically has received much attention in the weather community, owing to its capability of faster data update [11]. For demonstrating the

potential of PAR technology in weather surveillance, the National Weather Radar Testbed (NWRT), as the nation's first S-band phased array weather radar, was installed in Norman, Oklahoma in 2003 [12]. Research has demonstrated the potential benefits of faster data updates and adaptive scanning strategies of NWRT in issuing warnings for severe and hazardous weather [13-14].

In addition to faster data updates, PAR also has the potential to serve for multiple missions, which is motivated by MPAR (Multifunction Phased Array Radar) and SENSR (Spectrum Efficient National Surveillance Radar) projects. The concept is to replace the four radar networks in the United States with a single radar network. The four radar networks include (1) National Weather Surveillance Radar (WSR-88D or NEXRAD); (2) Terminal Doppler Weather Radar (TDWR) for detecting low altitude wind shear; (3) Airport Surveillance Radar (ASR) for air traffic control; and (4) Air Route Surveillance Radar (ARSR) for long-range air surveillance [15]. As a result, significant lifetime cost savings and performance improvement in weather and aircraft surveillance are expected. Based on the these considerations, a polarimetric PAR (PPAR) [16] is introduced, which is capable of both the polarimetry for multi-parameter measurements and the fast-scan proficiency of the PAR.

1.2 Planar Polarimetric Phased Array Radar

Currently, there are mainly two candidates for PPAR. The first candidate is a Planar PPAR (PPPAR), which includes two configurations as well. One configuration is a one-dimensional (1D) electronic scan PPPAR with an antenna mounted on a

mechanically steerable platform, such as the Phase-Tilt Radar for the Collaborative Adaptive Sensing of the Atmosphere, which performs electronic beam-steering only in the azimuth plane, while mechanically steering in the elevation plane [17-18], as shown in Figure 1-1(a). Alternatively, the 1D PPPAR can also be mechanically scanned in azimuth and electronically scanned in elevation, such as the X-band phased array weather radar (PAWR) at Osaka University in Japan, as shown in Figure 1-1(b) [19]. The other configuration is a two-dimensional (2D) electronic scan PPPAR, such as the Ten Panel Demonstrator (TPD) and Advanced Technology Demonstrator (ATD) of the National Severe Storms Laboratory (NSSL) as shown in Figure 1-1(c) and Figure 1-1 (d) respectively, which can perform electronic beam-steering in both azimuth and elevation directions [20-21].

Although there has been an extensive experience of PPPAR development in industry, it is challenging to collect high-quality polarimetric radar data of weather with a PPPAR, whose beam and polarization characteristics change with the electronic beam direction. For example, as the PPPAR beam is steered away from array broadside, the beamwidth will become wider, and scan loss is produced due to reduced effective aperture size. Moreover, as the PPPAR beam is steered away from the principal planes, there will be geometrically induced cross-polarization coupling [16, 22-25]. As a result, there will be sensitivity losses and measurement biases, which imposes a lot of difficulties for calibration and accurate polarimetric weather measurements. For example, to obtain a Z_{DR} bias of less than 0.2 dB as required by the NEXRAD specifications, the cross-polarization isolation needs to be better than 40 dB for the

STSR mode currently adopted in operational polarimetric NEXRAD, which is very difficult to achieve in practice [26]. Even if the Z_{DR} bias is correctable through calibration to the scattering matrix or to the radar variables, calibration over thousands of beams is extremely challenging from an operational perspective [16]. Compared with 2D PPPAR, the 1D PPPAR always has its beam in the principal planes without geometrically induced cross-polarization coupling and thus maintains scan-invariant beam characteristics in azimuth or elevation, but its performance in weather observation still needs to be demonstrated. Also, mechanical rotation is not desirable for PPAR, as it doesn't fully utilize the 2D electronic scan capability of PPAR and places constraints on the multi-mission objectives in future.

Due to the issues of PPPAR mentioned above, during the Second MPAR Symposium held in Norman, Oklahoma from November 17-19, 2009, the polarimetric calibration was identified as the most challenging technical issue for the future PPAR [27].

1.3 Cylindrical Polarimetric Phased Array Radar

The concept of cylindrical polarimetric phased array radar (CPPAR) was proposed for future weather measurements and multiple missions [22], which is the second candidate of PPAR. In a CPPAR system, beam-steering in the azimuth is realized by commutating scan, in which the beam direction changes in the azimuth by shifting a column of excited antenna sector and maintaining the weight symmetry about the beam center. As a result, CPPAR has scan-invariant beam characteristics (with the

same beamwidth) in azimuth, which is beneficial for calibration and data interpretation. Besides, wave fields in the horizontal and vertical polarizations are orthogonal in all directions, so cross-polarization isolation and polarization purity is maintained, which allows for high-quality polarimetric weather measurements. Moreover, CPPAR utilizes radiation power with high efficiency. In each azimuth, only certain columns are activated and weighted to form the desired beams, that is, the columns on the broadside are mostly activated and heavily weighted, so there is less scan loss due to the element radiation pattern [22].

Although CPPAR owns such advantages as mentioned above, there is very limited engineering development experience in CPPAR. Currently, the Syracuse Research Corporation (SRC) is known as the only company that has built cylindrical PARs. The radar is called Omni Directional Weapon Location (OWL), which has no dual-polarization capability [28]. To validate the CPPAR concept, a small-scale CPPAR demonstrator has been jointly developed by the staff engineers from Advanced Radar Research Center (ARRC) at the University of Oklahoma (OU) and the National Severe Storms Laboratory of NOAA [29-30], as shown in Figure 1-1(e). Initial weather measurements with CPPAR documented in [31] indicate that the measured copolar correlation coefficient was lower than expected due to the antenna beam mismatch between horizontal and vertical polarizations as well as other system instability issues. The frequency-scan dual-polarization column antennas were redesigned to eliminate the beam mismatch [32]. Besides, the CPPAR channel electronics were also rebuilt to ensure a more stable system, and commutating scan capability is realized. Initial

weather measurements have been made with the upgraded CPPAR demonstrator shown in Figure 1-1(f) since the summer of 2019.

1.4 Outline of the Dissertation

This dissertation presents initial results of weather measurements using the CPPAR demonstrator, and initial results for assessing polarimetric data quality based on these measurements. Chapter 2 summarizes the system specifications and field tests of the CPPAR demonstrator, including system overview, waveform design and verification, pattern optimization and far-field tests. Then the system calibration is discussed in detail, which includes calibration with an external source, calibration with single beam weather measurements, and calibration with ground clutter. Chapter 3 evaluates the CPPAR performance through an end-to-end phased array radar system simulator. It introduces the simulation framework, weather returns modeling, antenna pattern simulations, channel electronics modeling, and provides simulation results and comparison with those that would be obtained with a PPPAR. Chapter 4 presents weather measurements of a few convective precipitation cases and a stratiform precipitation case. Data of these cases are obtained using single beam mechanical scan and commutating beam electronic scan, respectively. Data collection and signal processing methods are discussed. First, the measurements are compared qualitatively with KTLX, which is one of the nearby operational NEXRAD radars. Then a quantitative comparison is made between the CPPAR mechanical scan and its electronic scan data, and error statistics are estimated and discussed. These preliminary comparisons show that the CPPAR can potentially meet the requirements of NEXRAD

specifications for data quality. Chapter 5 explores and verifies a feature of the commutating beam electronic scan in clutter detection. In addition, clutter detection based on multi-lag phase structure function, dual-scan cross-correlation coefficient, copolar correlation coefficient, and differential reflectivity with the CPPAR in both electronic scan and mechanical scan modes are presented and compared. Chapter 6 summarizes the work of the dissertation and discusses future work.

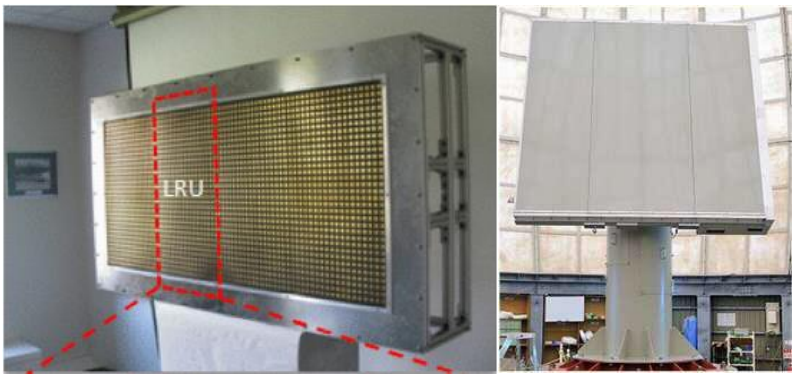

(a) (b)

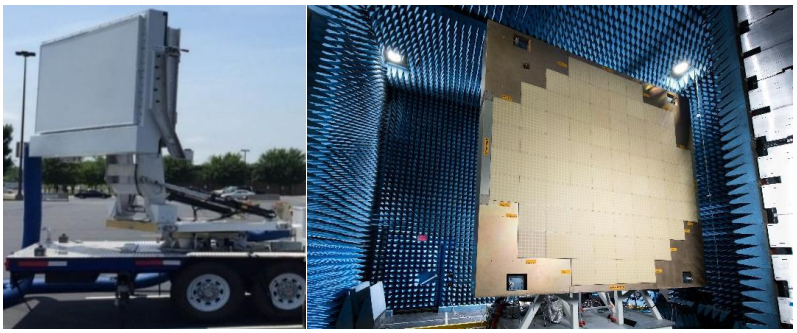

(c) (d)

(e) (f)

Figure 1-1 Pictures of PPARs. (a) CASA Phase-Tilt Radar. (b) PAWR at Osaka University. (c) NSSL Ten Panel Demonstrator. (d) NSSL Advanced Technology Demonstrator. (e) OU-NSSL CPPAR Demonstrator Version 1. (f) OU-NSSL CPPAR Demonstrator Version 2.

Chapter 2 CPPAR System Description

2.1 System Overview

The CPPAR demonstrator consists of a 2-meter diameter, 2-meter height cylinder, inside which there is a server for system control and communication, as shown in Figure 2-1. The cylinder is fully populated with 96 columns of subarrays, whereas currently only 48 of these columns are equipped with channel electronics. Each column is a 19-element linear array of dual-polarization, frequency-scanned, microstrip patch antenna, which is designed to operate over a frequency range from 2.7 to 3.0 GHz, corresponding to a scanning range from 0° to 20° in elevation [29, 32]. The spacing between the columns on the cylinder is 6.5 cm, equivalent to an azimuthal angle of 3.75°. Feed networks are designed to perform analog beamforming while doing commutating scans in azimuth. The technical specifications of the CPPAR demonstrator are listed in Table 2-1. The simplified functional block diagram of the CPPAR is depicted in Figure 2-2. As can be seen, each column has its own transmit/receive (T/R) module that includes a high-power-amplifier (HPA), circulator, limiter, low-noise-amplifier (LNA), etc. And CPPAR makes use of analog beamformers to split (during transmit) and combine (during receive) the signals, which employ attenuator and phase shifter to set the correct amplitude and phase for a desired beam-steering angle. The waveform generator, receiver, and analog-to-digital (A/D) converter are integrated into a single AD9361 radio frequency (RF) transceiver. The processor and controller unit mainly communicates with CPPAR and controls the pedestal.

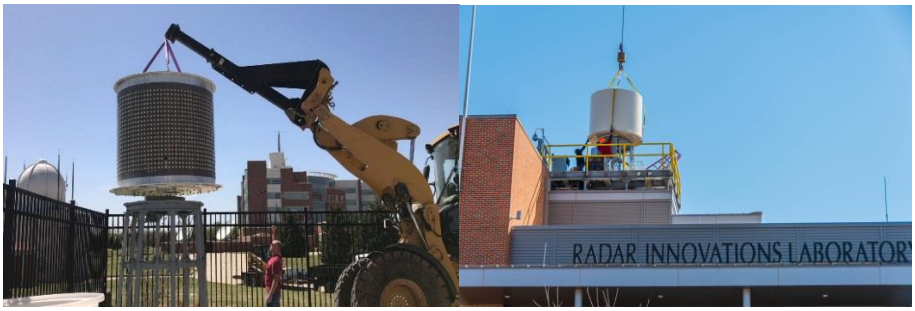

Figure 2-1 CPPAR demonstrator. (a) On the ground. (b) On the rooftop of Radar Innovations Laboratory.

Table 2-1 Technical specifications of the CPPAR demonstrator

Radar Parameters	Values
Frequency	2.7~3.0 GHz
Waveform	LFM/NLFM
Pulse Width	1~100 μs
Pulse Repetition Time	1~100 ms
Antenna Element	Patched column array
Beamwidth	Azimuth: 6.20°, Elevation: 5.35°
Sidelobes	⩽-28 dB
Polarization	Dual-polarization
Peak Power	180 W per column
Receiver Dynamic Range	74 dB
Receiver Noise Figure	2.8 dB
Bandwidth	1~5 MHz
Range Resolution	30~150 m

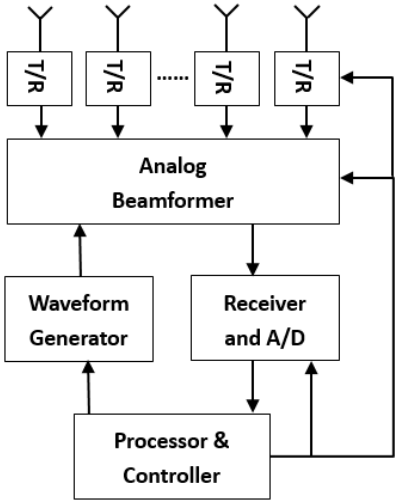

Figure 2-2 The simplified functional block diagram of the CPPAR demonstrator.

2.2 Waveform Design and Measurement

On transmit, the AD9361 RF transceiver uses a baseband synthesizer for waveform generation, including simple rectangular pulse, linear frequency modulation (LFM) waveform, and nonlinear frequency modulation (NLFM) waveform, etc. Based on the maximum sampling rate and available taps of the matched filter in the RF transceiver, an optimized NLFM pulse compression waveform is designed by following the genetic algorithm documented in [33] and implemented in CPPAR. As shown in Figure 2-3, the optimized NLFM waveform has a maximum pulse width of 34 μs, peak sidelobe level below -63 dB and integrated sidelobe level below -41 dB, as well as a power efficiency of 93.66% and a 3-dB range resolution of 80 meters. The actual transmit waveform was measured by a far-field calibration horn mounted on the National Weather Center which is about 225 meters away from the CPPAR. The measured frequency spectrum and autocorrelation function are shown in Figure 2-3. Due to the distortion caused by nonlinearity of the HPA in the CPPAR, range sidelobes of the actual NLFM waveform increase to -53 dB, which is still acceptable for most weather measurements.

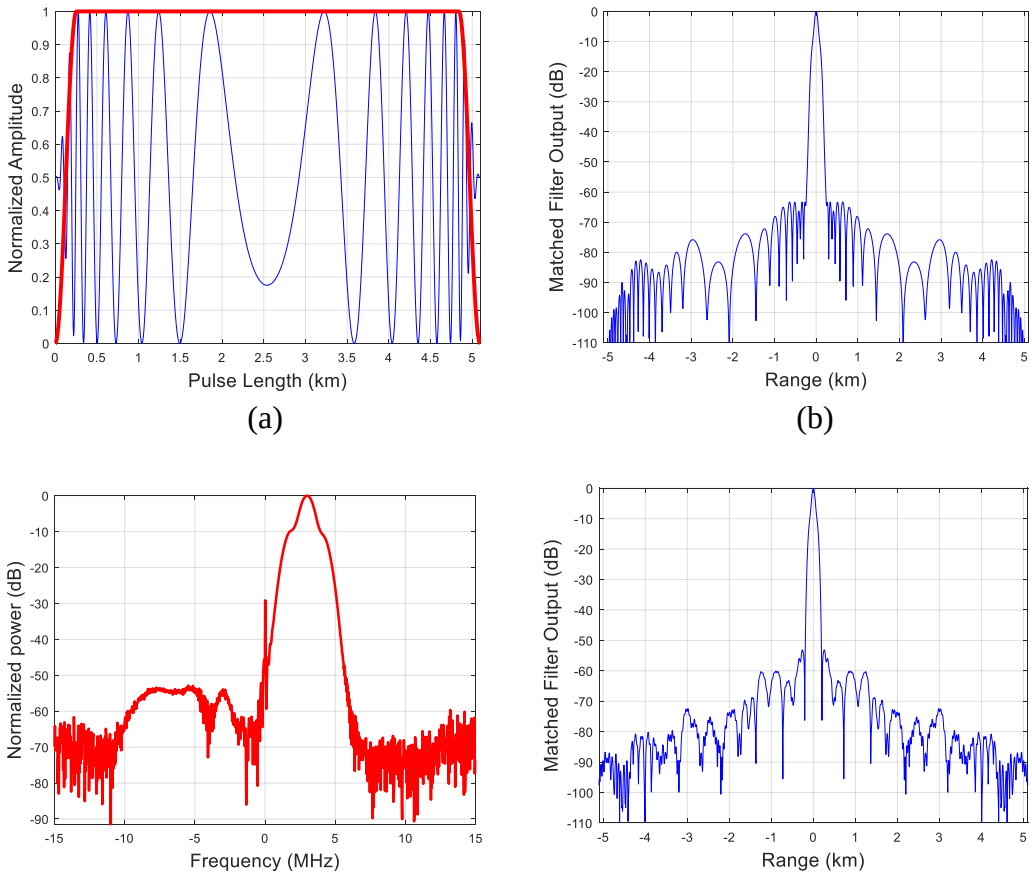

Figure 2-3 NLFM waveform in CPPAR. (a) The real component of the designed waveform. (b) Autocorrelation function of the designed waveform. (c) The spectrum of measured waveform. (d) Autocorrelation function of measured waveform.

2.3 Pattern Optimization and Measurement

For demonstrating of the CPPAR's advantages in polarization purity and scan-invariant beam characteristics in azimuth, the CPPAR beam patterns are measured by the calibration horn mentioned in Section 2.2. The horn height can be adjusted based on the CPPAR beam-steering elevation, which is determined by the frequency of operation. At the frequency of 2.76 GHz, the CPPAR points at 3.3 degrees in elevation, and the horn is mounted at approximately 13 meters above the CPPAR. The CPPAR and the far-field horn are synchronized by the Global Positioning System (GPS) receivers, and their relative positions are shown in Figure 2-4. First, all

the azimuthal element (column) radiation patterns are measured. As in [34], a multi-objective optimization method is used to find the optimum weights to form the beams from the center of each active 90-degree sector (24 columns) of the cylinder. The goal is to match the copolar patterns between horizontal and vertical polarizations for all commutating beams while minimizing the sidelobe levels and maximizing the gain. Then the beamforming weights optimized from the central sector (Column No.13~36) are applied on all the commutating sectors for beamforming. The normalized power and phase of the calibration offset and beamforming weights are plotted in Figure 2-5. Figure 2-6 shows the optimized horizontal and vertical polarization beam patterns of an active 90-degree sector of CPPAR, which have sidelobe levels lower than -28 dB (one-way), and the cross-polarization levels are below -37 dB from the copolar peak.

Figure 2-4 Relative positions of the CPPAR (within the red circle on the left) and the far-field horn (within the red circle on the right).

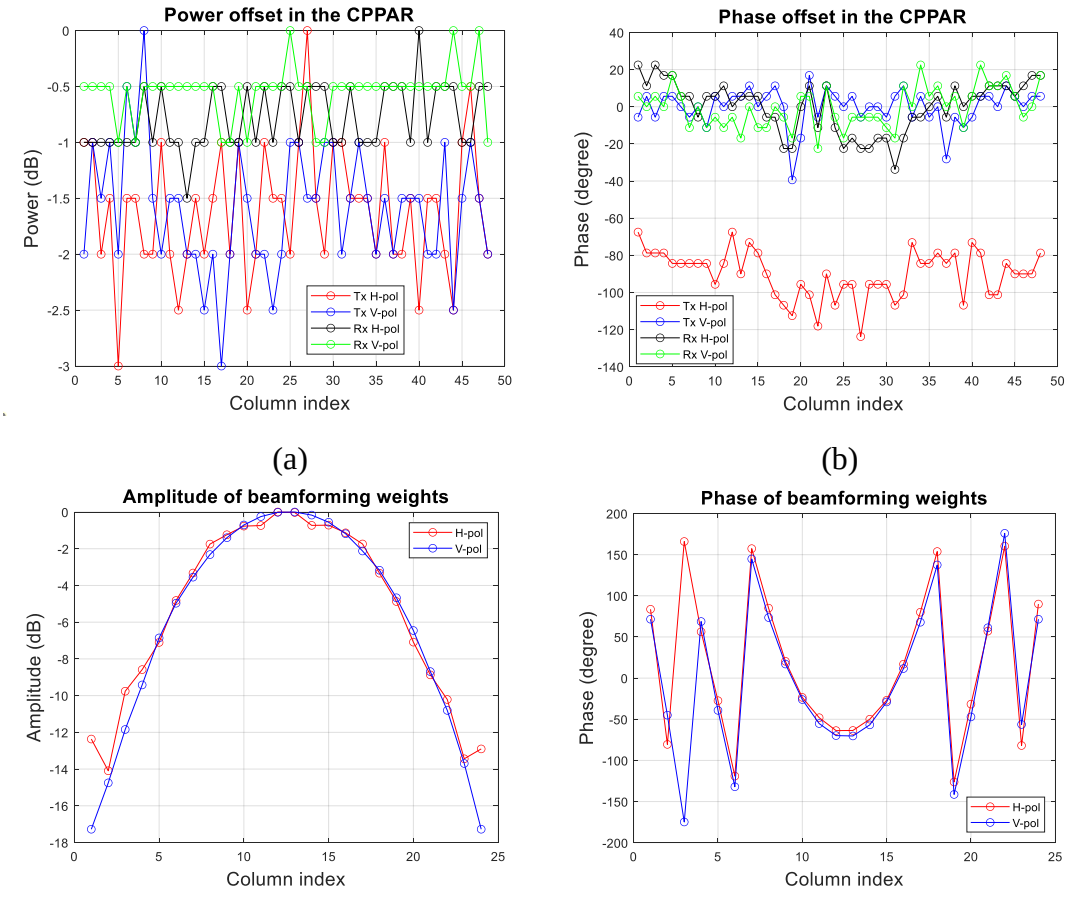

Figure 2-5 Normalized power and phase of the calibration offset and beamforming weights in the CPPAR. (a) Normalized power of the calibration offset. (b) Phase of the calibration offset. (c) Normalized amplitude of the beamforming weights. (d) Phase of the beamforming weights.

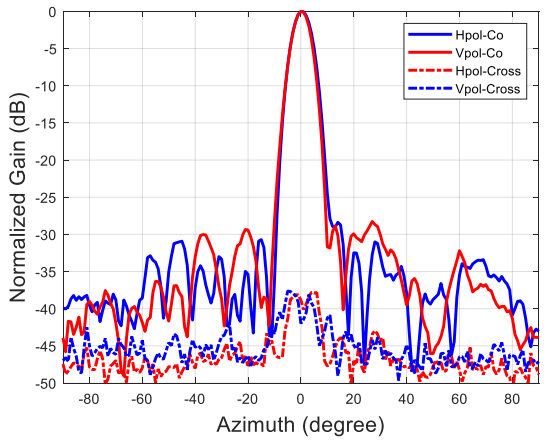

Figure 2-6 Optimized array radiation patterns of the CPPAR.

2.4 System Calibration

In electronic scan mode, due to the variations in element (column) pattern and channel electronics (attenuator, phase shifter, etc.), the system calibration factor (radar constant) may be slightly different from beam to beam. The purpose of radar system calibration is to minimize measurement errors due to system uncertainty, drifting, and instabilities. In this section, three methods are utilized to calibrate the CPPAR, including (1) Calibration with an external source, (2) Calibration with weather measurements of mechanical scan, and (3) Calibration using ground clutter.

2.4.1 Calibration with an External Source

The first approach utilizes the calibration horn as an external source to calibrate the CPPAR. As the main lobe of CPPAR beam patterns can be approximated by a Gaussian shape, the one-way CPPAR beam patterns measured by the calibration horn are fitted using the Gaussian model to find the beamwidth and gain of all the 25 commutating beams. Besides, the phase of the peak point (beam center) in each beam pattern can be obtained. The fitted beam patterns (for one beam), 3-dB beamwidth, system gain (including antenna gain and transceiver gain), and phase of all the 25 commutating beams in horizontal and vertical polarizations for both transmit and receive patterns are plotted in Figure 2-7 (a)-(d) and Figure 2-8 (a)-(d) respectively.

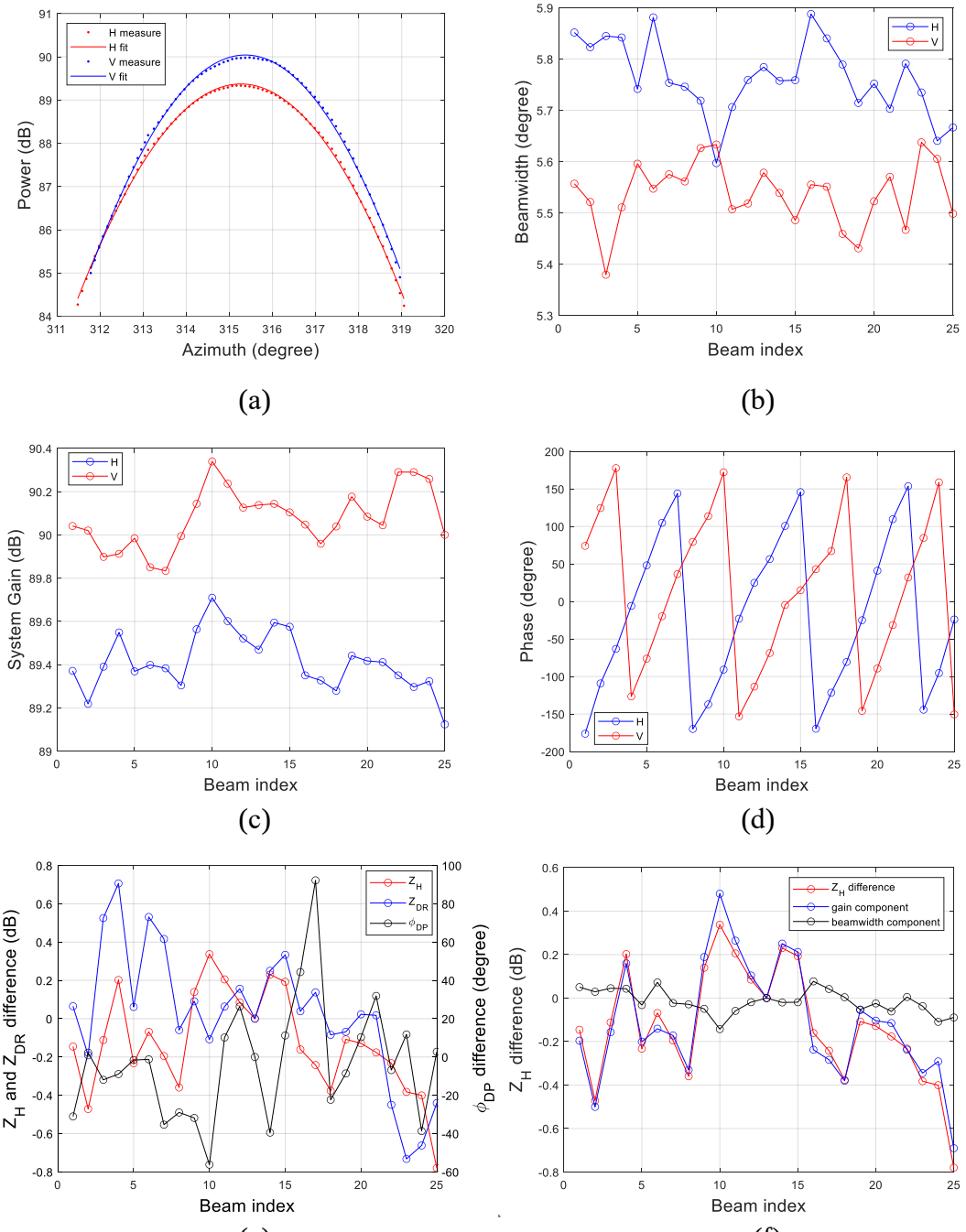

Figure 2-7 CPPAR calibration with an external source (CPPAR transmit pattern). (a) Measured and fitted one-way beam patterns. (b) Estimated 3-dB beamwidth. (c) Estimated system gain. (d) Estimated phase. (e) Mean differences for Z_H, Z_{DR}, and ϕ_{DP}. (f) Gain and beamwidth contribution to Z_H difference.

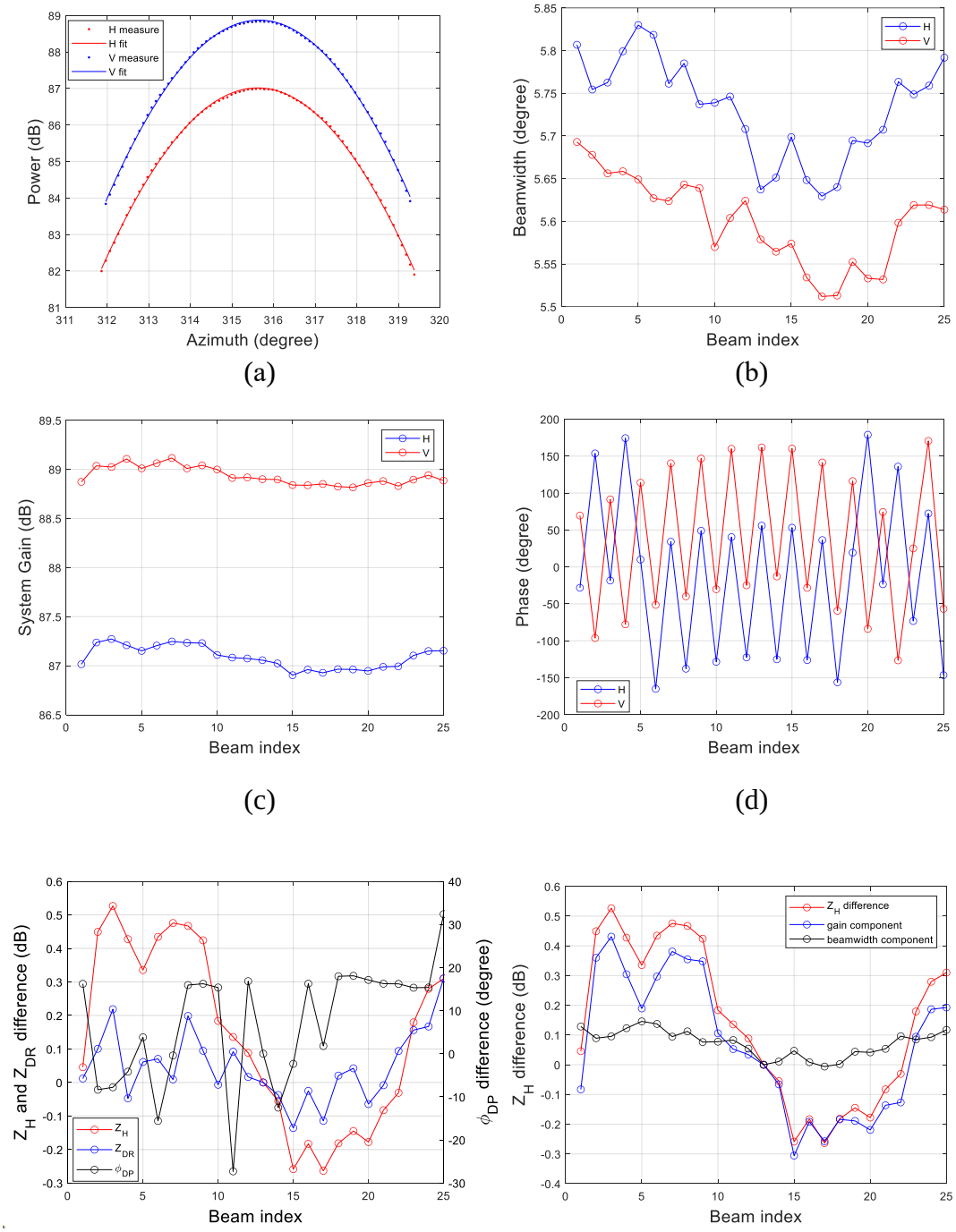

Figure 2-8 CPPAR calibration with an external source (CPPAR receive pattern). (a) Measured and fitted one-way beam patterns. (b) Estimated 3-dB beamwidth. (c) Estimated system gain. (d) Estimated phase. (e) Mean differences for Z_{H}, Z_{DR}, and ϕ_{DP}. (f) Gain and beamwidth contribution to Z_{H} difference.

Based on weather radar equation [1]:

$$P_{\mathrm{r}} = P_{\mathrm{t}} g^2 \eta c \tau \pi \theta \varphi \lambda^2 / ((4\pi)^3 r^2 l^2 16 \ln 2) \tag{2-1}$$

the antenna gain g can be separated into azimuth gain g_{az} and elevation gain g_{el}. As CPPAR is operated at a fixed elevation angle, g_{el} and elevation beamwidth θ are constant for all the commutative beams, while the variable factors are g_{az} and azimuth beamwidth φ. Then the beam-to-beam mean differences for Z_{H}, Z_{DR}, and ϕ_{DP} with source calibration are obtained as below:

$$\Delta Z_{\mathrm{H}} = 10 \cdot \log_{10}\left(g_{\mathrm{h}}^2 \cdot \varphi_{\mathrm{h}}\right) = 2G_h + 10 \cdot \log_{10}(\varphi_{\mathrm{h}}) \tag{2-2}$$

$$\Delta Z_{\mathrm{DR}} = 2 \cdot (G_{\mathrm{h}} - G_{\mathrm{v}}) + 10 \cdot \log_{10}(\varphi_{\mathrm{h}}/\varphi_{\mathrm{v}}) \tag{2-3}$$

$$\Delta \phi_{\mathrm{DP}} = 2 \cdot (\phi_{\mathrm{h}} - \phi_{\mathrm{v}}) \tag{2-4}$$

which are shown in Figure 2-7 (e) and Figure 2-8 (e), respectively. In addition, the contributions of gain and beamwidth variations to Z_{H} difference are shown in Figure 2-7 (f) and Figure 2-8 (f), which indicates that gain variation plays a major role in beam-to-beam Z_{H} difference.

2.4.2 Calibration with Weather Measurements of Mechanical Scan

The second approach is to compensate for the beam-to-beam variation based on weather measurements of single-beam mechanical scan. The first step is to obtain radar constant for the single beam formed by the central sector. It is necessary to find the conversion coefficient (system gain) that relates the input power level and output power level of CPPAR, which is related with CPPAR system components such as the RF transceiver, T/R module, etc. A method based on noise power measurement is employed to find the conversion coefficient. On the one hand, the minimum detectable signal (MDS) power at CPPAR receiver input is calculated as [1]

$$MDS = 10 \cdot \log_{10}(kTB) + NF \tag{2-5}$$

where $k = 1.38 \cdot 10^{-23}$ is the Boltzmann's constant in J/K, T is the temperature of the thermal noise in kelvins, B is the CPPAR receiver bandwidth in Hz, NF is the noise figure of the CPPAR receiver system in dB. On the other hand, the measured noise power at receiver output can be estimated as the minimum power for all the azimuth radials at a specific range bin,

$$N_{out} = 10 \cdot \log_{10}\left(\min\left(\frac{1}{M}\sum_{m=1}^{M}|V_m|^2\right)\right) \tag{2-6}$$

where V_m is voltage sample in volts, M is the number of pulses in the dwell time. Then the conversion coefficient is obtained as

$$C_0 = N_{out} - MDS \tag{2-7}$$

which is subtracted from the Z_{H} estimate.

$$Z_{\mathrm{H}} = Z_{\mathrm{H}} - C_0 \tag{2-8}$$

For validating the accuracy of the conversion coefficient, the theoretical sensitivity of CPPAR as a function of range is calculated as

$$Z_{\min} = MDS + C + 20 \cdot \log_{10} R \tag{2-9}$$

where $C = 98.14$ dB is the radar constant calculated from CPPAR specifications, R is the range of resolution volume in km. Then the measured sensitivity of CPPAR can be found in each range bin and compared with $Z_{\min}$. The comparison results measured on a rainy day and on a clear air day respectively, are shown in Figure 2-9.

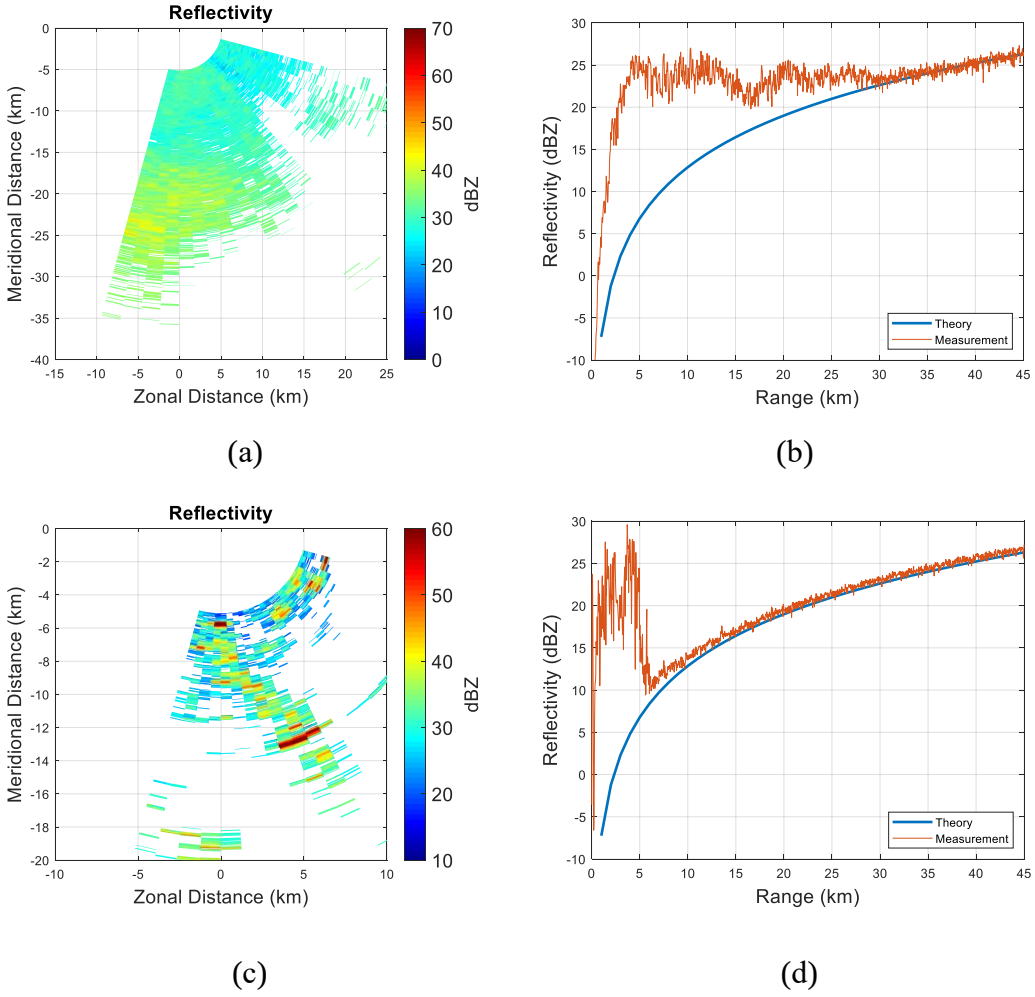

Figure 2-9 The sensitivity of CPPAR as a function of range measured in various weather conditions. (a) Reflectivity measured by CPPAR on a rainy day. (b) CPPAR sensitivity as a function of range on a rainy day. (c) Reflectivity measured by CPPAR on a clear air day. (d) CPPAR sensitivity as a function of range on a clear air day.

As shown in Figure 2-9, on a rainy day (clutter filtering was applied), the measured MDS (sensitivity) is generally higher than the theoretical curve until 30 km, which is due to the fact that weather returns overlap with noise in the first 30 km. As a comparison, on a clear air day (no clutter filtering was applied), as there is no weather return overlapped with noise, the two curves are very consistent except for the first 5.1 km where is the blind range of CPPAR corresponding to a pulse width of 34 μs. Therefore, it proves that the estimated C_0 and C are reasonable. Besides, C_0 and C

values are also verified by a visual comparison of reflectivity with KTLX (a nearby operational NEXRAD) measurements. It should be noted that as the CPPAR and KTLX have different locations and resolutions, precise comparisons between them are not practical. Therefore, the following verifications mainly focus on consistency of CPPAR measurements using different scan methods.

The second step is to use the differences between electronic scan and mechanical scan from the previous experiment to calibrate the measurements of the current electronic scan. The measurements used for calibration applied a threshold of signal-to-noise ratio (SNR) ≥ 10 dB to mitigate noise effect. Example measurements from CPPAR mechanical scan, electronic scan and their difference for Z_{H}, Z_{DR}, and ϕ_{DP} are plotted in Figure 2-10.

The mean differences of Z_{H}, Z_{DR}, and ϕ_{DP} along range in each beam used for calibration are shown in Figure 2-11. As can be seen, the Z_{H} differences are typically within 0.4 dB, the Z_{DR} differences are less than 0.3 dB, and the ϕ_{DP} differences are mostly within 5.0 degrees. This shows the consistency of the commutating beams of the CPPAR. After correction of these small variations, the electronic scan measurements become more consistent, which will be discussed in Chapter 4.

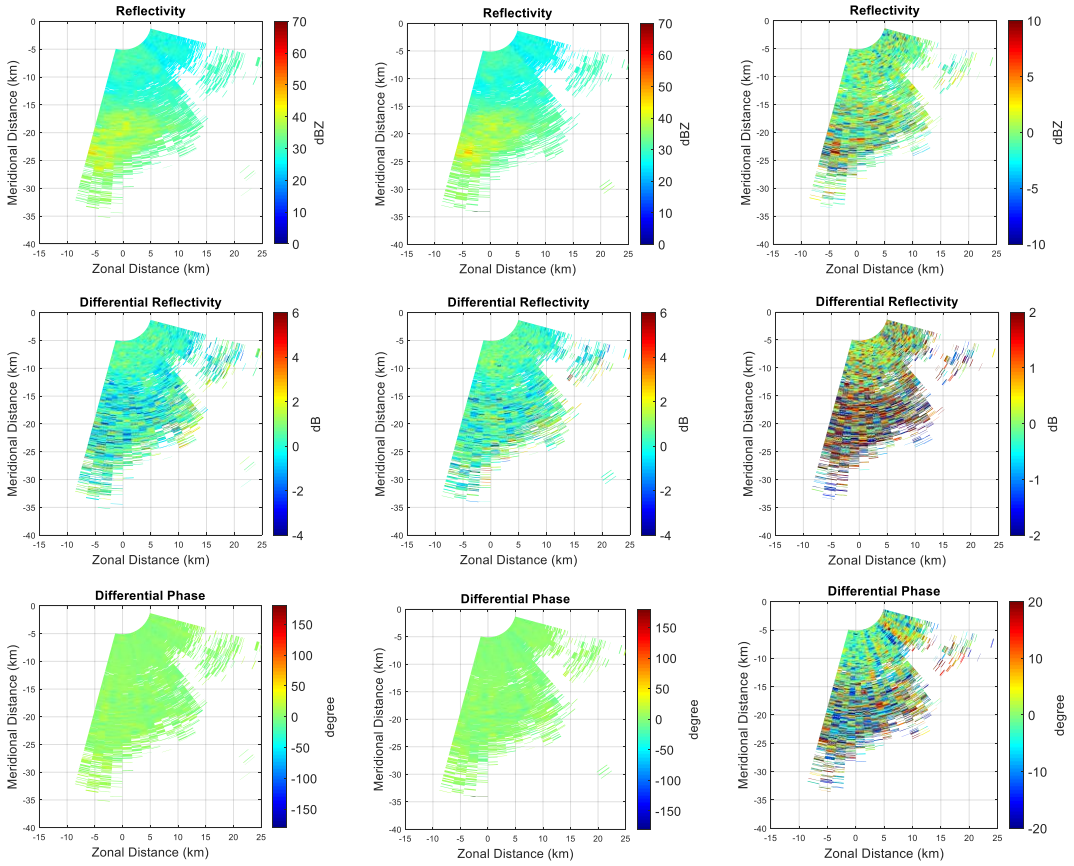

Figure 2-10 CPPAR calibration by single-beam weather measurements. Left column: measurements of CPPAR mechanical scan; middle column: measurements of CPPAR electronic scan; right column: the difference between electronic scan and mechanical scan of the CPPAR.

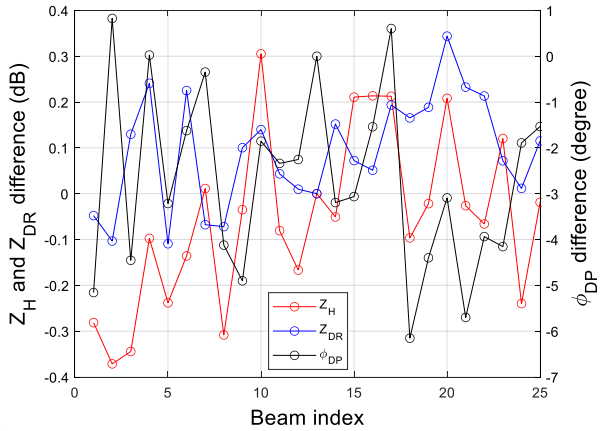

Figure 2-11 Mean differences between electronic scan and mechanical scan for CPPAR calibration.

2.4.3 Calibration using Ground Clutter Returns

The third approach is to calibrate the CPPAR with a stationary ground clutter,

which is a large grain silo located about 6 km to the south (azimuth≈178 degrees) of the CPPAR. During the calibration, each CPPAR beam mechanically scans across the clutter at a slow rate of 0.5 degrees/s to mitigate beam smearing effect. Then a two-way beam pattern centring at the clutter direction can be obtained for each beam. Similar to Section 2.4.1, these patterns are fitted by Gaussian model to estimate the beamwidth, gain, and phase, for both horizontal and vertical polarizations, which are used to calculate the Z_{H}, Z_{DR}, and ϕ_{DP} differences among the 25 beams. It should be noted that for the two-way beam patterns measured with clutter, beamwidth should be selected as the 6-dB beamwidth, gain difference includes transmit and receive components, and the phase difference also contains transmit and receive components. The mean differences for Z_{H}, Z_{DR}, and ϕ_{DP} with clutter calibration are obtained as:

$$\Delta Z_{\mathrm{H}} = 10 \cdot \log_{10}\left(g_{\mathrm{h}}^2 \cdot \varphi_{\mathrm{h}}\right) = G_{\mathrm{h}} + 10 \cdot \log_{10}(\varphi_{\mathrm{h}}) \tag{2-10}$$

$$\Delta Z_{\mathrm{DR}} = G_{\mathrm{h}} - G_{\mathrm{v}} + 10 \cdot \log_{10}(\varphi_{\mathrm{h}}/\varphi_{\mathrm{v}}) \tag{2-11}$$

$$\Delta \phi_{\mathrm{DP}} = \phi_{\mathrm{h}} - \phi_{\mathrm{v}} \tag{2-12}$$

Figure 2-12 (a) and (b) show the clutter in reflectivity plot measured by CPPAR on a clear air day and radial profiles of reflectivity for all the 25 beams; Figure 2-12 (c) and (d) display the images of clutter objects in Google Maps and Apple Maps, respectively; Figure 2-12 (e) plots the measured and fitted two-way patterns for one beam; Figure 2-12 (f) plots the beam-to-beam mean variations for Z_{H}, Z_{DR}, and ϕ_{DP}.

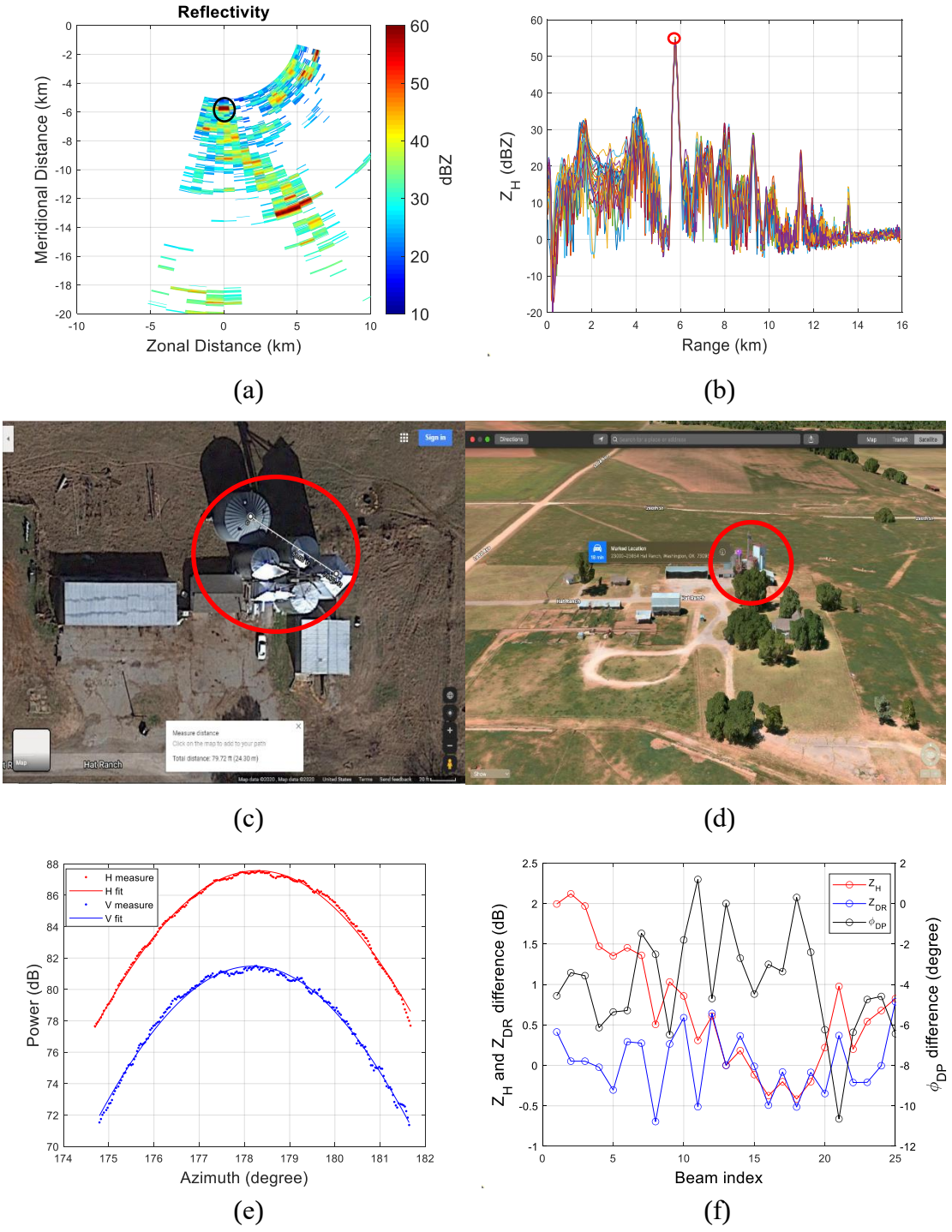

Figure 2-12 CPPAR calibration by clutter. (a) Clutter in reflectivity plot measured by CPPAR. (b) Radial profiles of reflectivity for 25 beams. (c) Image of the ground clutter structure from Google Maps. (d) Image of the ground clutter structure in Apple Maps. (e) Measured and fitted two-way beam patterns. (f) Beam-to-beam mean differences for Z_H, Z_{DR}, and ϕ_{DP}.

For comparison, mean differences of Z_H, Z_{DR}, and ϕ_{DP} obtained with various calibration methods presented above are plotted together in Figure 2-13.

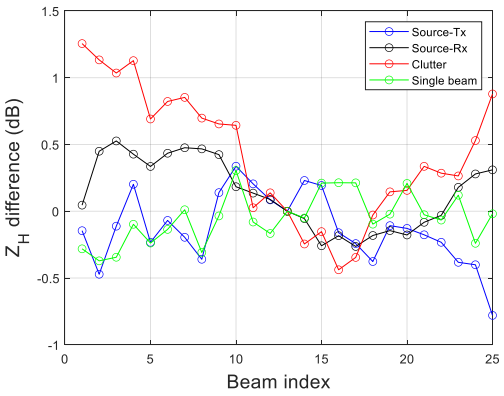

(a)

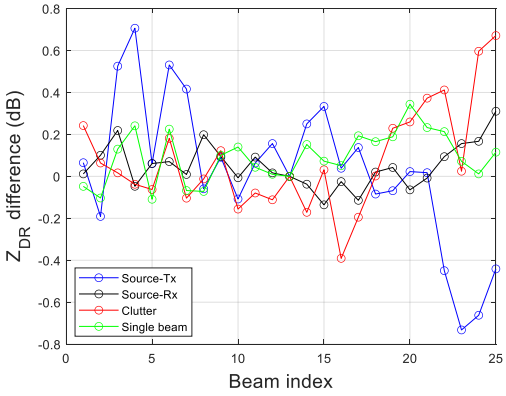

(b)

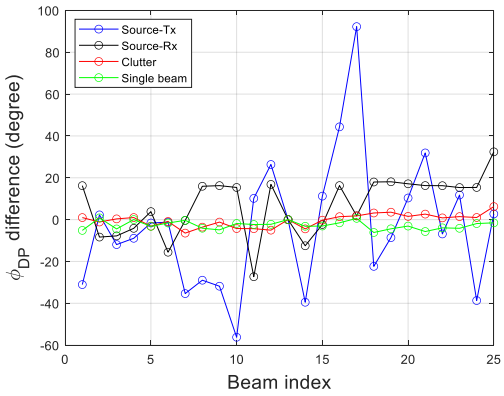

(c)

Figure 2-13 Averaged beam-to-beam variations for Z_H, Z_{DR}, and ϕ_{DP} obtained with various calibration methods. (a) Mean Z_H difference. (b) Mean Z_{DR} difference. (c) Mean ϕ_{DP} difference.

As shown in Figure 2-13, source calibration using CPPAR transmit pattern and calibration using single beam weather measurements have similar mean Z_H difference. As the HPAs in CPPAR are more stable than that in the calibration source, the mean Z_H difference obtained from CPPAR transmit pattern should be more reliable than that obtained from CPPAR receive pattern. Besides, it is found that calibration using single beam weather measurements and calibration using ground clutter have similar mean ϕ_{DP} difference, whereas the results from source calibration have large fluctuations which may be due to the measurement errors in the beam patterns. Generally,

calibration using single beam weather measurements have more reasonable beam-to-beam mean differences for Z_{H}, Z_{DR}, and ϕ_{DP}. Therefore, it is employed in practice.

After calibration, to evaluate the CPPAR performance in weather measurements, an end-to-end phased array radar system simulator is developed, including the simulation framework, weather returns modeling, antenna pattern simulations, channel electronics modeling, and system simulation results, which are introduced in Chapter 3.

Chapter 3 System Simulation for Performance Evaluation

3.1 Introduction

Data quality of polarimetric weather radar measurements is an important factor for the "research to operation" goal of polarimetric phased array radars application to weather surveillance. There have been three existing methods used so far for the evaluation of radar data quality. The first is theoretical analysis [16, 25, 35], in which rigorous mathematical models are used to derive analytical equations about biases and standard deviations of polarimetric weather radar variables. The limitation of this method is that many realistic system factors cannot be modeled due to the complexity, and the assumptions on the radar components, for example, radiating elements and their patterns, are usually ideal. The second method is building and evaluating actual radar systems for data collections. This is usually called proof-of-concept [20-21]. Measurements through proof-of-concept are the most realistic data for performance evaluations. On the other hand, developing a proof-of-concept is a long-term and costly process. It is largely affected by factors beyond principal scientific focuses, such as markets, availability of commercial components, financial resources, and cooperation of the weather conditions. The third method for evaluation is radar data analysis through system simulation. Simulation is an effective method to connect the theoretical analysis and actual weather measurements. It can discover the key system factors that are not fully addressed by either theoretical analysis or actual measurements and provide the results as guidance to radar designers. The block diagram to depict the relationships between radar system simulations, theoretical analysis, radar measurements,

engineering designers, as well as system users and planners is presented in Figure 3-1, in which “radar system simulations” acts as a bridge connecting the other elements.

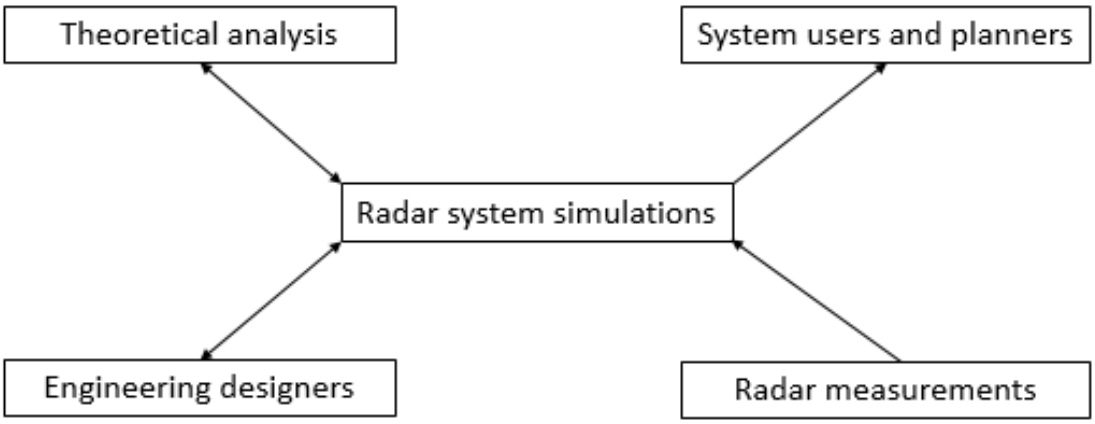

Figure 3-1 The role of radar system simulation.

Various weather radar system simulators were developed before. For example, Zrnić [36] described a procedure for simulating weather like Doppler spectra and signals, in which time series of single-polarization weather radar was generated. Galati and Pavan [37] extended Zrnić’s method to dual-polarized Doppler weather radar by generating two random sequences of horizontal and vertical polarization pairs with an assigned autocorrelation coefficient and a cross-correlation coefficient. Torres [38] presented a method for simulating over-sampled dual-polarization radar signals by combining Zrnić’s method and Galati’s work. Cheong et al. [39] introduced a weather radar simulator which derived time series signals from the output of a numerical weather prediction (NWP) model. Byrd et al. [40] presented a polarimetric phased array weather radar simulator, which evaluated the impacts of cross-polar fields on weather measurements and included various transmit modes. Ivić [41] introduced an approach to simulate the effects of antenna patterns on polarimetric variable estimates. Barcaroli

et al. [42] presented a validation procedure to assess the ability of a polarimetric weather radar simulator to deal with raindrop-size distributions and outputs generated by NWP models. Recently Schvartzman et al. [43] introduced a weather radar simulator which uses existing NEXRAD measurement as truth and it was still based on a traditional frequency-domain method for polarimetric time series generation.

Even with the achievements of prior simulations, data quality prediction and analysis for PPAR remain a challenge due to the limitations such as (1) using NWP model outputs as weather truth fields is limited to specific scenarios and events that are not sufficient for comprehensive and realistic representation for all different operational cases; (2) existing PPAR simulations are based on the traditional "frequency-domain" approach for time-series generation, which focuses on statistical behavior of radar signals in frequency domain; (3) although antenna patterns are widely included in previous simulators, the impacts of phased array radar electronics are as important to data quality in practical applications, such as the distortions caused by amplifier nonlinearity, phase shifter quantization, or any instabilities of the array elements that have been reported to affect the overall system performance and data quality [44-45]. Weather measurements are highly sensitive to such effects, but none of the current weather radar system simulators have taken them into account.

In this Chapter, a phased array radar system simulator (PASIM) [46-48] is presented, which is a time-domain simulation software package that utilizes the operational NEXRAD Level II data as the basis of weather truth fields. Usage of such data is more of an engineering solution rather than meteorological significance. In

PASIM, a Monte Carlo method is applied for weather returns modeling. The simulation process employs time-domain system update and electronics behavior models to address the combined effects of antennas, T/R modules, and pulse compression waveforms. By using the functions in the MATLAB Phased Array System Toolbox and other tools, the software is intrinsically based on time-step simulations. The new simulation approach can address the challenges of large-scale system data quality prediction and adds new insights to the system design validations. Performance evaluation metrics, including bias and standard deviation of the estimated polarimetric weather radar variables compared to the truth fields, are direct outputs from the simulation system. As such, it can evaluate how the data quality differs and what design approaches are recommended for the best tradeoff under different types of weather.

In addition, for the first time, the side-by-side comparisons of the results from the three evaluation methods for a specific PPAR are obtained. The consistency among the results from the three evaluations and some discrepancies are identified. It is further revealed through the system simulations that some potential factors such as the scan-dependent beam characteristics of planar phased array antenna have impacts on generations of these discrepancies. It is concluded that PASIM is an effective solution that could “unify” the different evaluation methods for engineering risk mitigations.

3.2 Simulation Framework

In PASIM, all the basic radar subsystems are modeled as system objects, including a waveform generator, transmitter, antenna, platform, weather returns,

propagation path, receiver, beamformer, etc. The parameters can be defined flexibly to support system-level tradeoff analysis. At each scanning angle, positions of radar and weather scatterers can be updated based on their motions. Then the target (radar resolution cell) angles seen by the radar beams are calculated. After that, a steering vector of the current scan angle is computed, from which a radar beam is formed. During each dwell time, a pulse containing the designed transmit waveform is generated, amplified by the transmitter object and radiated by the antenna ("radiator") object. When the radiated signals interact with the weather scatterers, they are reflected and collected by the antenna ("collector") objects. Then the return signals are amplified by the receiver and beamformed, processed by a matched filter and stored into a three-dimensional (3D) data cube (azimuth × range × pulse). During this process, if the receiver sampling rate is sufficiently high, the transmitted and received signals can be computed based on time-step evolution from a pulse to the next.

Currently, NEXRAD Level II data are used as input into the simulator and sampled as "truth fields". Note that the NEXRAD data here are not meteorological truth fields, but measured radar moments from NEXRAD. Based on phased array radar system specifications, modeling parameters, and antenna pattern measurements, an end-to-end system simulation can be conducted, and the in-phase and quadrature time series (I & Q) data can be obtained and saved as a data cube. Subsequently, the data cube is fed into a signal processing chain to obtain polarimetric estimates. Finally, these estimates are compared with NEXRAD Level II data and error statistics are obtained.

The framework of PASIM with its functional blocks, and how these blocks are implemented using different programming languages are depicted in Figure 3-2. The radar system simulation and the testing scenario are based on NEXRAD Level II data. Additional meteorological data are also obtained through Advanced Weather Interactive Processing System (AWIPS), which can be used to improve the ground truth data of the weather scenarios and provide a data quality visualization. The system component (antenna, T/R module and digital backend) parameters are provided from available commercial products. The core of the implementation is based on MATLAB Phased Array System Toolbox [49-50] and other toolboxes. Customized models include signal processing modules and electronics models. The output of the simulator is data quality analysis report.

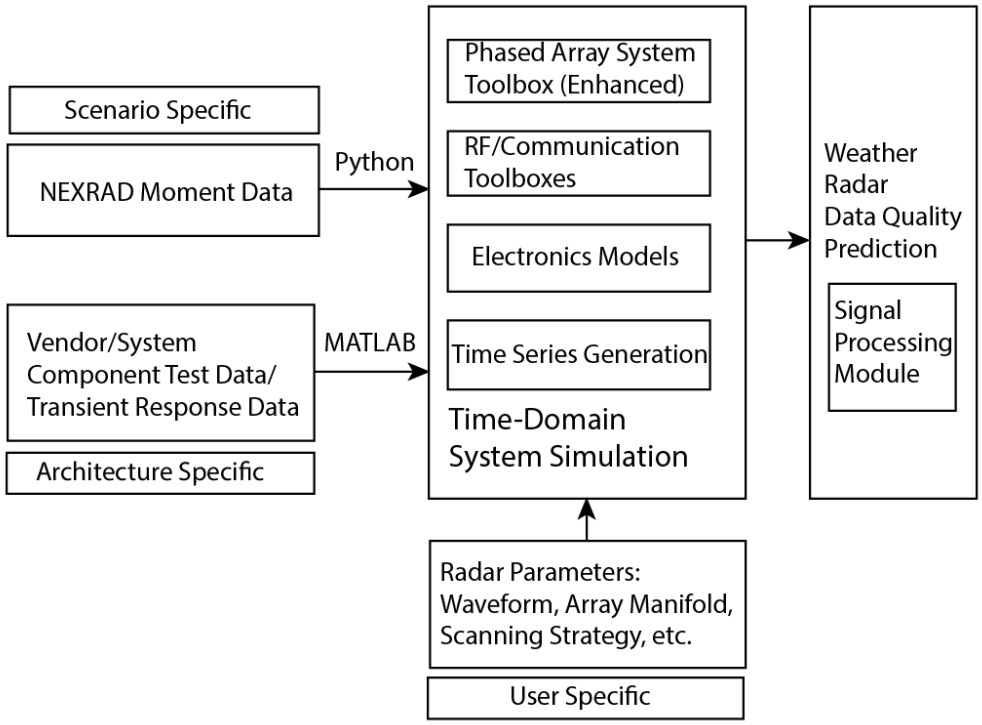

Figure 3-2 The framework of PASIM.

Specifically, in Figure 3-2, the input blocks are comprised of three parts. The "NEXRAD Moment Data" refer to NEXRAD Level II data available from the National Climatic Data Center and are read by the Python ARM Radar Toolkit (Py-ART), which is an open-source software package widely used in weather radar community [51-52]. The "Vendor/System Component Test Data/Transient Response Data" refer to the radar component parameters used in a real phased array radar system, such as the datasheet of AD9361/9371 RF transceiver, the nonlinear response curve of an HPA, etc. The "Radar Parameters" contain user-specific radar system specifications, including waveform (simple rectangular, pulse compression), array manifolds (planar, cylindrical, etc.), scanning strategy (Plan Position Indicator (PPI), Range Height Indicator (RHI), volume scan), etc. The "Time-Domain System Simulation" block is the core of PASIM, which employs the MATLAB Phased Array System Toolbox, RF/Communications Toolbox and electronics models to perform end-to-end time domain radar system simulations, as shown in Figure 3-3 (a), whose output is time series data organized in a 3D data cube. The "Weather Radar Data Quality Prediction" block produces radar data quality analysis report. Figure 3-3 (b) summarizes the overall data flow of weather radar data quality prediction. Time series data for all the radar transceiver channels are organized into a data cube, which is fed into the weather radar signal processing chain to compute spectral moments and polarimetric variables. The radar estimates are compared with the NEXRAD Level-II data to produce data quality report in the form of statistical errors such as bias and standard deviation.

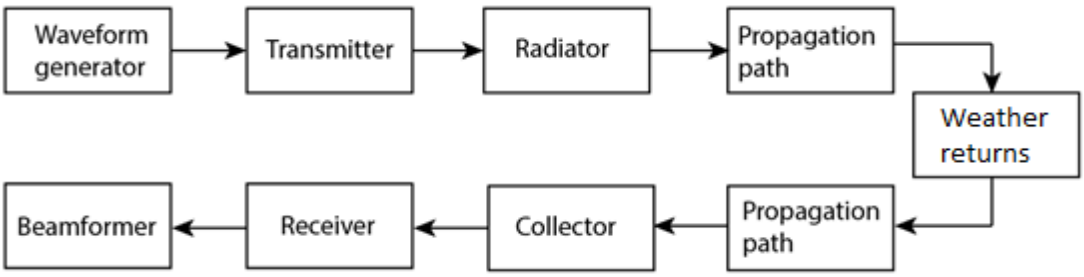

(a)

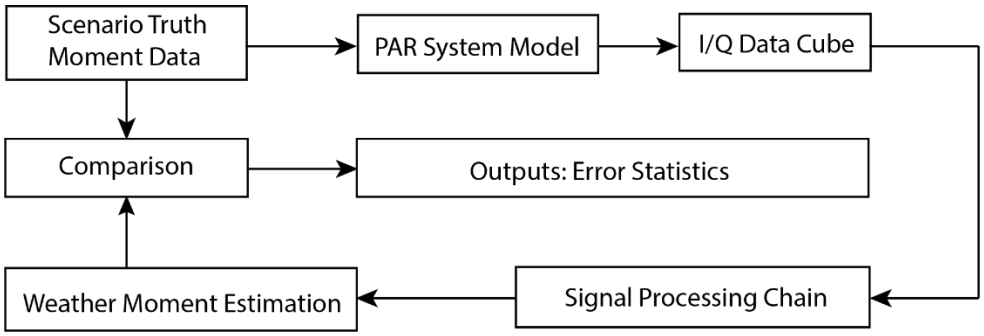

(b)

Figure 3-3 Operations of the key modules of PASIM. (a) Time-domain system simulation. (b) Weather radar data quality prediction.

3.3 Weather Returns Modeling

3.3.1 Monte Carlo Method

In PASIM, weather radar returns are generated in time-domain, i.e., marching from pulse to pulse. Scattering amplitudes of weather returns at every time step (pulse repetition time) are combinations from random multiple scattering centers, which is an extension of the complex scattering theory to distributed volume scatterers. These scatterers have random relative positions in the resolution volume as well as variations of velocities that are updated every pulse repetition time. Each scattering center's backscattering amplitude and phase are determined from the weather truth fields measured by NEXRAD or user-defined weather scenarios. According to the definition of reflectivity factor [2],

$$Z_{\mathrm{hh}} = \frac{4\lambda^4}{\pi^4 |K_{\mathrm{w}}|^2} \int |s_{\mathrm{hh}}|^2 N(D) dD = K \int |s_{\mathrm{hh}}|^2 N(D) dD \tag{3-1}$$

where Z_{hh} is the reflectivity factor for horizontal polarization in mm^6 m^{-3}, λ is radar wavelength in mm, D is drop diameter in mm, $N(D)$ is drop size distribution in mm^{-1} m^{-3}, K_{w} is the dielectric constant factor of water (unitless), s_{hh} is the horizontal backscattering amplitude in mm. For simplicity, in PASIM it is assumed that all the scatterers within the resolution volume have the same size and zero canting angles, so that the off-diagonal terms of their backscattering matrices are zero. Therefore,

$$|s_{\mathrm{hh}}| = \sqrt{Z_{\mathrm{hh}}/K/N} \tag{3-2}$$

where N is the number of scatterers in the resolution volume, which is set at 100 in the simulation. This is sufficient to generate Gaussian random signals. Accordingly, the vertical scattering amplitude of each scatterer can be calculated as

$$|s_{\mathrm{vv}}| = s_{\mathrm{hh}}/\sqrt{Z_{\mathrm{dr}}} \tag{3-3}$$

where Z_{dr} is the differential reflectivity on a linear scale.

In addition, the copolar correlation coefficient ρ_{hv} is assumed to be reduced by a factor of $e^{-\sigma_\delta^2/2}$ due to the random scattering phase difference, where σ_δ is the standard deviation of random scattering phase difference (see Eq. (4.86) in [2]), that is, $\rho_{\mathrm{hv}} = e^{-\sigma_\delta^2/2}$. Then

$$\sigma_\delta = \sqrt{-2\ln(\rho_{\mathrm{hv}})} = \sqrt{\sigma_{\delta\mathrm{h}}^2 + \sigma_{\delta\mathrm{v}}^2} \tag{3-4}$$

For simplicity, it is assumed that $\sigma_{\delta\mathrm{h}} = \sigma_{\delta\mathrm{v}} = \sigma_\delta/\sqrt{2}$, where $\sigma_{\delta\mathrm{h}}$ and $\sigma_{\delta\mathrm{v}}$ are standard deviations of the backscattering phase δ_{h} in horizontal polarization and the backscattering phase δ_{v} in vertical polarization, respectively. Then the complex scattering amplitudes for each scatterer can be expressed as

$$s_{\mathrm{hh}} = |s_{\mathrm{hh}}| \cdot e^{-\mathrm{j}\delta_{\mathrm{h}}} \cdot e^{-\mathrm{j}\phi_{\mathrm{DP}}} \tag{3-5}$$

$$s_{\mathrm{vv}} = |s_{\mathrm{vv}}| \cdot e^{-\mathrm{j}\delta_{\mathrm{v}}} \tag{3-6}$$

where ϕ_{DP} is the differential phase. Therefore, the total complex backscattering amplitudes of the resolution volume are

$$S_{\mathrm{hh}} = \sum_{l=1}^{N} s_{\mathrm{hh}} \cdot e^{-\mathrm{j}2\mathrm{k_i}\cdot\mathrm{r}_l} \tag{3-7}$$

$$S_{\mathrm{vv}} = \sum_{l=1}^{N} s_{\mathrm{vv}} \cdot e^{-\mathrm{j}2\mathrm{k_i}\cdot\mathrm{r}_l} \tag{3-8}$$

where k_{i} is incident wave vectors, r_l is the random position of each scatterer.

The end-to-end array signals in PASIM is modeled as

$$\boldsymbol{V} = \boldsymbol{F}^{\mathbf{R}}\boldsymbol{S}\boldsymbol{F}^{\mathbf{T}}\boldsymbol{X} + \boldsymbol{N} \tag{3-9}$$

where $\boldsymbol{V}$ is received complex baseband voltage, $\boldsymbol{X}$ is excitation voltage on the antenna port, $\boldsymbol{F}^{\mathbf{T}}$ and $\boldsymbol{F}^{\mathbf{R}}$ refer to transmit and receive antenna patterns, respectively, $\boldsymbol{S}$ is scattering matrix of weather scatterers, $\boldsymbol{N}$ includes noise and interference present at receiver output.

3.3.2 Covariance Matrix Method

Weather returns modeling based on the statistical correlation among pulses and polarizations is the second method in PASIM. Firstly, two independent random signals V_1 and V_2 are generated, which follow Gaussian distribution with zero-mean and their standard deviations are derived from reflectivity values. According to [1], the autocorrelation function of the received signals in each polarization is given by

$$R(mT_s) = S \cdot e^{-8\left(\frac{\pi\sigma_{\mathrm{v}}mT_{\mathrm{s}}}{\lambda}\right)^2} \cdot e^{-j\frac{4\pi\bar{v}mT_{\mathrm{s}}}{\lambda}} + N \cdot \delta_m \tag{3-10}$$

where S is the average signal power, $\bar{v}$ and σ_{v} refer to mean radial velocity and spectrum width of the radar resolution volume filled by precipitation, m is the index

of the pulse ($0 \leq m \leq M-1$, where M is the number of pulses in the dwell time), and T_s is pulse repetition time, N is the mean white noise power, and δ_m is 1 for $m = 0$ and zero otherwise. Based on (3-10), a complex covariance matrix C, which is a M-by-M Hermitian positive-definite matrix, can be constructed. Using Cholesky decomposition, C may be decomposed as

$$C = P \cdot P^* \tag{3-11}$$

where P is a M-by-M upper triangular matrix from the diagonal and upper triangle of covariance matrix C. Then P is multiplied with V_1 and V_2 respectively as

$$V_1 = V_1 \cdot P \tag{3-12}$$

$$V_2 = V_2 \cdot P \tag{3-13}$$

Finally, the complex scattering amplitudes of the resolution volume are generated as

$$S_{\mathrm{hh}} = V_1 \tag{3-14}$$

$$S_{\mathrm{vv}} = \left[\rho_{\mathrm{hv}} \cdot V_1 + \sqrt{1-\rho_{\mathrm{hv}}^2} \cdot V_2\right] \cdot \frac{e^{j\phi_{\mathrm{DP}}}}{\sqrt{Z_{\mathrm{dr}}}} \tag{3-15}$$

As a comparison, both Monte Carlo method and covariance matrix method are statistical methods. Generally, Monte Carlo method is more representative of the physical process in the real world, as it assumes that there are multiple scatterers within each resolution volume. A large number of simulations show that both methods can achieve similar accuracy for radar estimates when other radar system parameters are the same.

3.4 Antenna Pattern

In PASIM, the phased array radar is placed on a platform, whose position, velocity and acceleration can be defined. The orientation axes of the platform can be manipulated by a rotation matrix, making it suitable for both ground-based and airborne applications. Besides, effects of electronic scanning such as beam broadening and scan loss are incorporated. Both element radiation pattern and array pattern can be imported from electromagnetic (EM) simulations or chamber measurements. Moreover, the antenna element is modeled to have polarization diversity by specifying polarized radiation patterns. For instance, realistic dual-polarized patch and crossed-dipole elements have been included, whose horizontal and vertical polarization components can be transmitted simultaneously or alternately to measure the target scattering matrix. Array axis can be specified flexibly so that array elements are located along the selected coordinate system axis. The computation of array factor supports linear array, planar array, circular array, and conformal array (i.e., cylindrical array), while beam-steering and beamforming are implemented by applying complex weights to the individual elements of the array. To accelerate the computations, a full array can be partitioned into one or more subarrays, and each subarray can be steered independently. Furthermore, both copolar and cross-polar components of antenna pattern are modeled in PASIM. As an example, Figure 3-4 shows the 3D radiation pattern of a dual-polarized patch element used in system simulations.

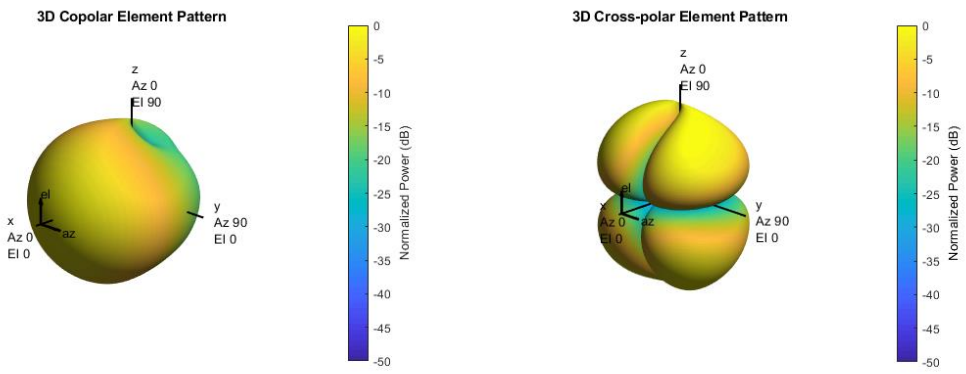

(a) (b)

Figure 3-4 The 3D antenna radiating element in PASIM. (a) Copolar component. (b) Cross-polar component.

The radiation patterns of the dual-polarized patch antenna element are generated using the High Frequency Structural Simulator (HFSS), which is a commercial solver for EM problems. The normalized power patterns and phase patterns for both copolar and cross-polar components of the patch element are plotted in Figure 3-5, where the subscripts h and v denote horizontal and vertical polarizations, respectively. The first index i of F_{ij} refers to the polarization of the radiated electric field, and the second index j refers to the antenna's excitation port.

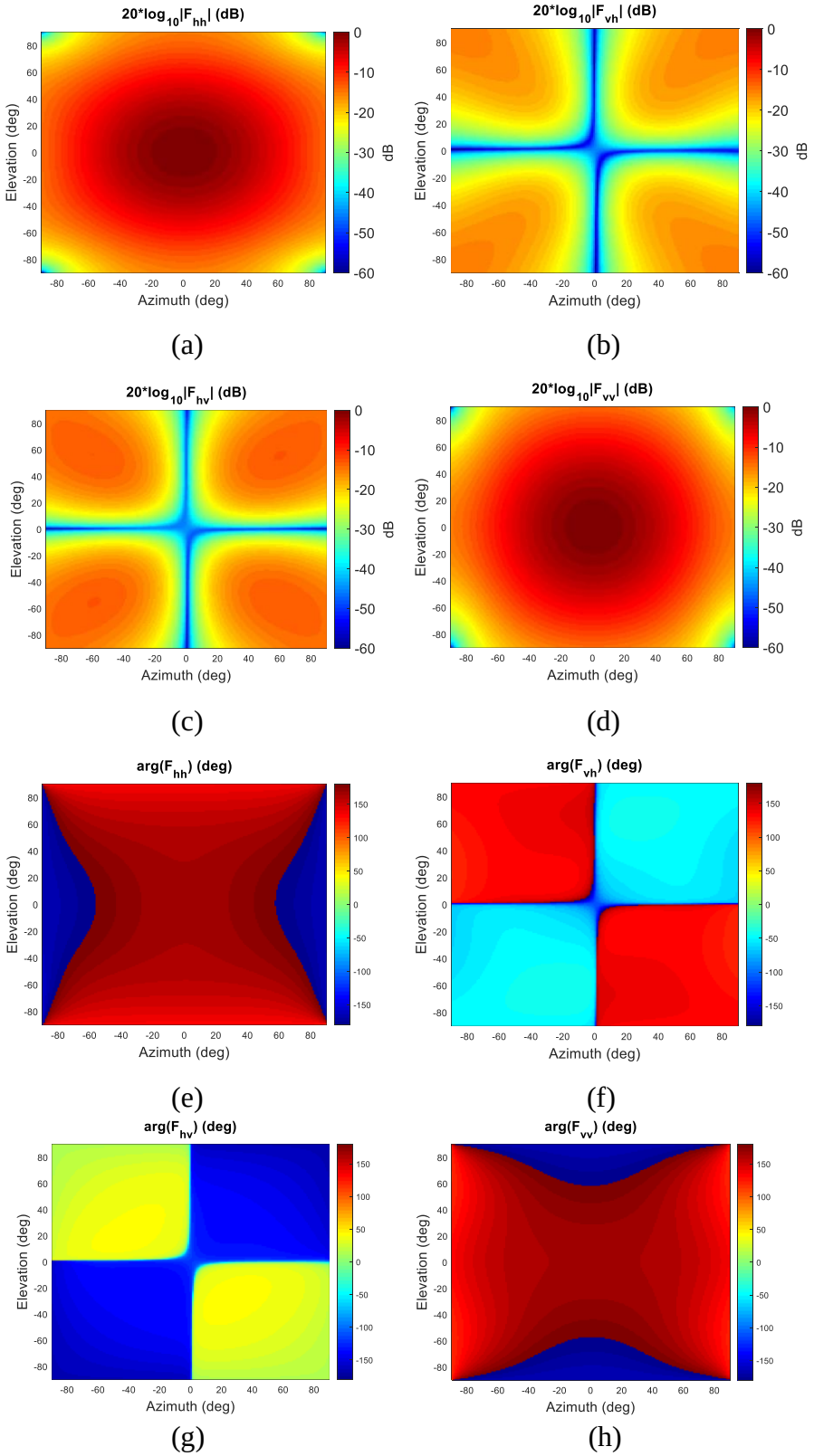

Figure 3-5 Normalized one-way element patterns for a patch antenna radiating element. (a) H copolar power pattern. (b) H cross-polar power pattern. (c) V cross-polar power pattern. (d) V copolar power pattern. (e) H copolar phase pattern. (f) H cross-polar phase pattern. (g) V cross-polar phase pattern. (h) V copolar phase pattern.

3.5 Channel Electronics Modeling

For a multi-channel polarimetric phased array radar system such as CPPAR, electronics instability from pulse-to-pulse (P2P) and channel-to-channel (C2C) needs to be modeled, including HPA distortions and instabilities in RF transceiver channels, quantization error of phase shifters and attenuators in T/R modules, imbalance of the power combiners and splitters in each channel, fluctuation in receiver noise floor, phase variations caused by local oscillator and reference clock instability, etc. Among all these factors, HPA complex gain (including amplitude and phase) variation due to thermal effects, which may reduce the system coherency [53], is a major source of electronics instability. Accordingly, several mathematical models have been developed to characterize the nonlinear behavior of HPA, such as Saleh model, Volterra series model, complex power series model, and Hammerstein-Wiener model [44]. In this study, Saleh model is used as a simple two-parameter function to depict the AM-to-AM and AM-to-PM characteristics of nonlinear amplifiers. Ideally, the input signal to the amplifier is expressed as [54]

$$x(t) = r(t)\cos[\omega_0 t + \varphi(t)] \tag{3-16}$$

where ω_0 is carrier frequency; $r(t)$ and $\varphi(t)$ are respectively the amplitude and phase of the modulated signal. The distorted output of the nonlinear amplifier is

$$y(t) = A[r(t)]\cos\left[\omega_0 t + \varphi(t) + \Phi[r(t)]\right] \tag{3-17}$$

where $A[r(t)]$ refers to AM-to-AM conversion, and $\Phi[r(t)]$ refers to AM-to-PM conversion. Specifically, these two functions can be expressed as

$$A(r) = \alpha_a r/(1 + \beta_a r^2) \tag{3-18}$$

$$\Phi(\mathrm{r}) = \alpha_\phi r^2/(1+\beta_\phi r^2) \tag{3-19}$$

As an example, the optimum parameters for a solid-state power amplifier (SSPA) are selected as $\alpha_\mathrm{a} = 2.1587$, $\beta_\mathrm{a} = 1.1517$, $\alpha_\phi = 4.0033$, $\beta_\phi = 9.1040$. Figure 3-6 (a) shows the ideal and distorted envelope of a 30 dB Taylor-windowed LFM waveform, and Figure 3-6 (b) compares their autocorrelation functions (ACF). As can be seen, after Saleh nonlinearity model is incorporated in the amplifier, the LFM waveform is distorted, and the matched filter output shows increased range sidelobes which are undesirable.

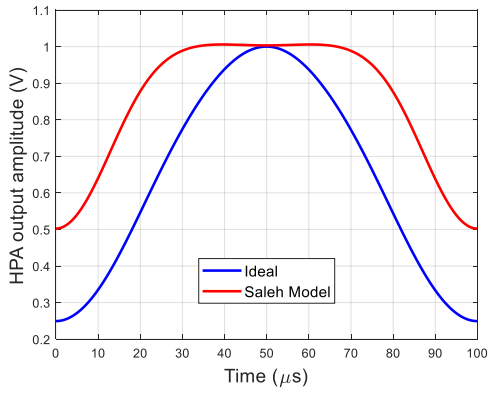

(a)

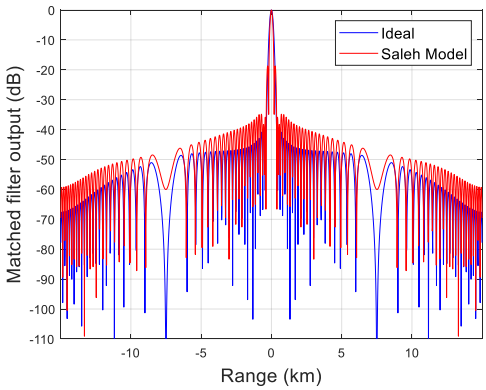

(b)

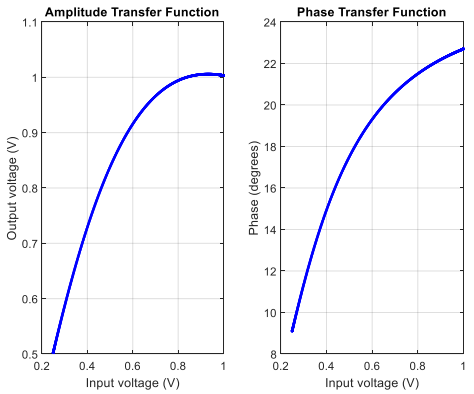

(c)

Figure 3-6 The impact of Saleh nonlinearity model of HPA on an LFM waveform and matched filter output. (a) Waveform envelope with and without nonlinear distortion. (b) Matched filter output with and without nonlinear distortion. (c) Amplitude and phase transfer function.

On the other hand, the C2C spatial instability in a PAR can be evaluated in

PASIM as well. The C2C amplitude instability mainly distorts antenna pattern, while C2C phase instability will both distort antenna pattern and increase phase noise. Another C2C error comes from T/R module failure, which distorts antenna pattern by raising sidelobe and reducing gain. Also, the impact of quantization error introduced by digital phase shifter can also be assessed using PASIM. These errors are included during the beamforming process. As an example, a 2-meter diameter CPPAR demonstrator comprised of 96 columns and 19 rows is constructed in PASIM. It is assumed that 5-bit phase shifters are used. Figure 3-7 shows the comparison of CPPAR transmit beam patterns without quantization error and those with quantization error based on 5-bit phase shifters. It shows that the sidelobes of CPPAR beam patterns increase as a result of the quantization error caused by 5-bit phase shifters.

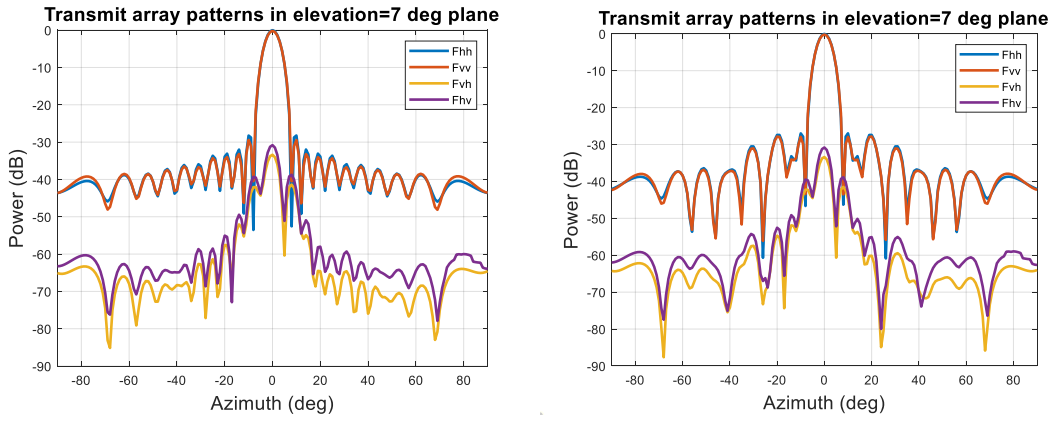

(a) (b)

Figure 3-7 The simulated CPPAR beam patterns. (a) Without quantization error. (b) With quantization error based on 5-bit phase shifters.

3.6 Simulation Results

3.6.1 CPPAR System

A 2-meter diameter CPPAR demonstrator comprised of 96 columns and 19 rows is constructed in PASIM. In each dwell time, CPPAR commutates by 1 column,

which shifts 3.75 degrees in azimuth. Both transmit array and receive array are tapered to have sidelobes below -30 dB. The technical specifications of the simulated CPPAR demonstrator are listed in Table 3-1, which are nearly the same as the configuration during actual weather measurements to be shown in Chapter 4. The simulated CPPAR cylinder, element (column) pattern, and beam patterns are shown in Figure 3-8. The selected weather scenario is a 90 degrees azimuthal sector of user-defined, idealized uniform weather truth fields without reflectivity gradient, whose radar variables are listed in Table 3-2. This configuration suppresses the impacts from range sidelobes of pulse compression waveforms and antenna sidelobes of beam patterns, so that the simulated polarimetric biases can truly reflect the effects of the radar system components, such as the differences between the copolar fields as well as the coupling of cross-polar fields. At each azimuth angle, 64 pulses are transmitted. For both principal plane (0 degrees elevation) and non-principal plane (7 degrees elevation), the simulated biases for Z_{DR}, ρ_{hv}, and ϕ_{DP} along beam-steering angle in azimuth are presented in Figure 3-9. Besides, the computed polarimetric biases based on analytical equations in [25] are also provided in Figure 3-9 for comparison.

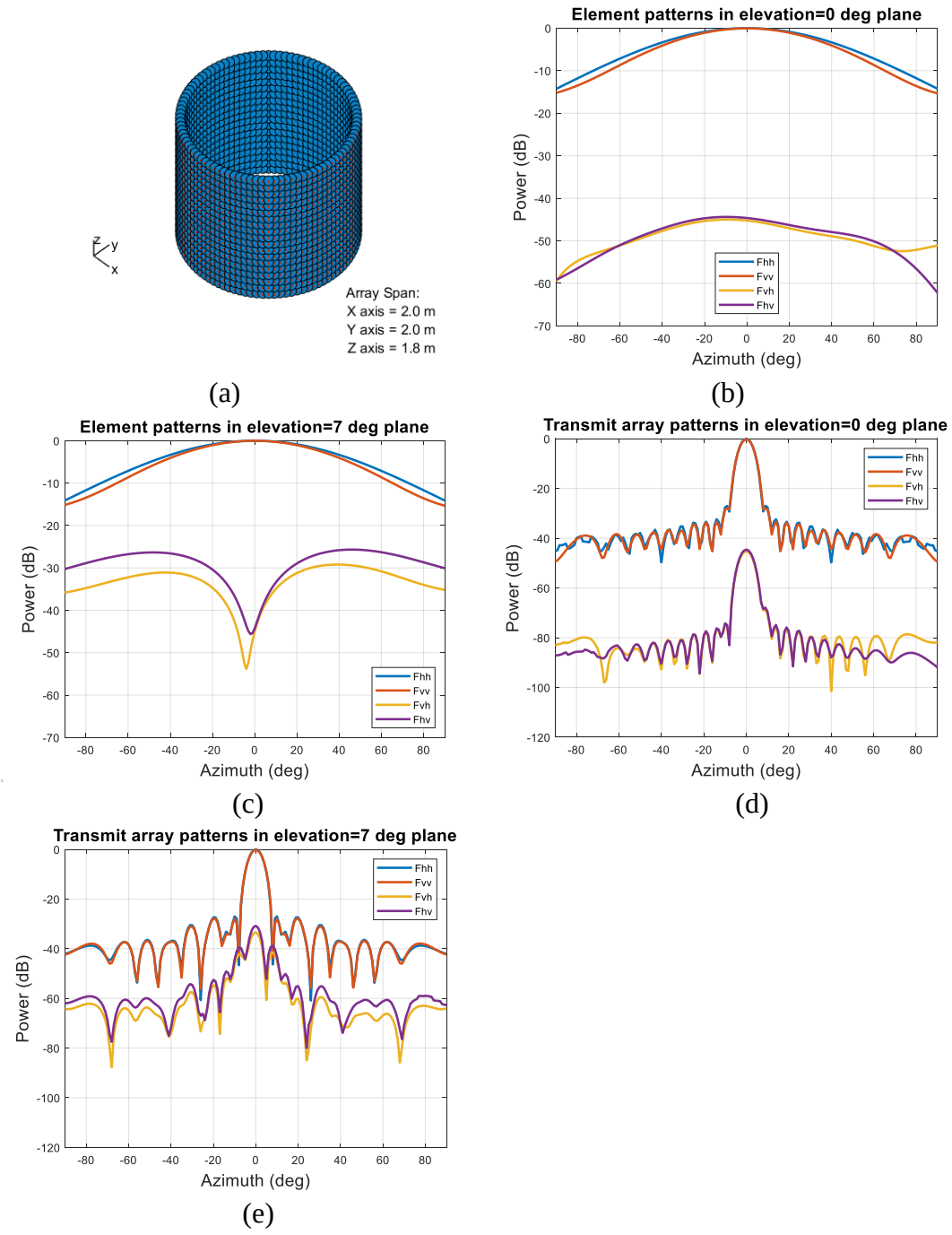

Figure 3-8 The simulated CPPAR and beam patterns. (a) CPPAR cylinder. (b) Element patterns in elevation=0 degrees plane. (c) Element patterns in elevation=7 degrees plane. (d) Beam patterns in elevation=0 degrees plane. (e) Beam patterns in elevation=7 degrees plane.

Table 3-1 Technical specifications of the simulated CPPAR

Parameters	**Values**
Frequency	2760 MHz
Waveform	LFM
Peak Power	180 W per column
Pulse Width	34 μs
Pulse Repetition Time	1 ms
Pulses Per Dwell	64
Receiver Bandwidth	1 MHz
Noise Figure	2.8 dB
Beamwidth	Azimuth: 6.20°, Elevation: 5.35°
Radiating Element	Patched column array
Beam Sectors	25
Selected Beam Sector	Columns No.1~24, 2~25, …, 25~48.
Azimuth Sampling Rate	3.75° per dwell

Table 3-2 Assumed values for uniform weather truth fields

Radar Variables	Values
Z_{H} (dBZ)	30
v_{r} (m/s)	10
σ_{v} (m/s)	4
Z_{DR} (dB)	0
ρ_{hv}	0.99
ϕ_{DP} (degree)	0

As shown in Figure 3-9, all the biases of the simulated CPPAR's polarimetric radar estimates are close to zero in both elevation=0 degrees and elevation=7 degrees planes, which can potentially satisfy NEXRAD requirements for data quality, and the fluctuations of the estimates are mainly due to sampling error.

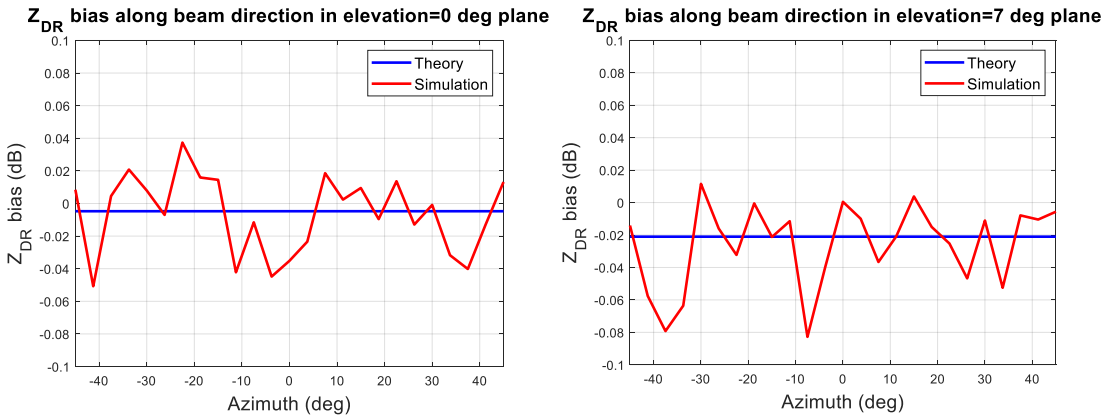

(a)

(b)

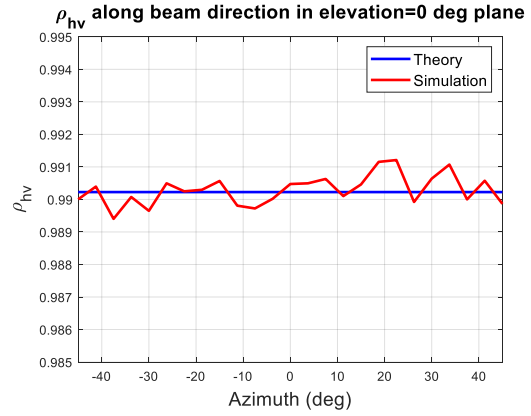

(c)

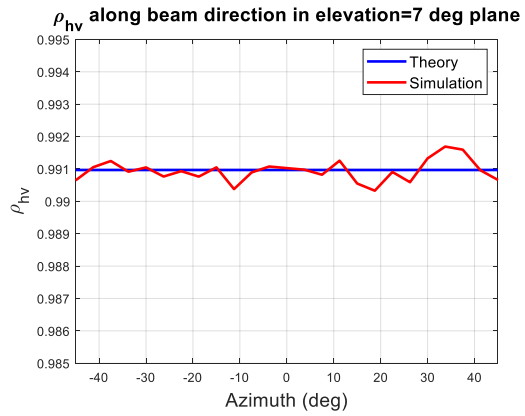

(d)

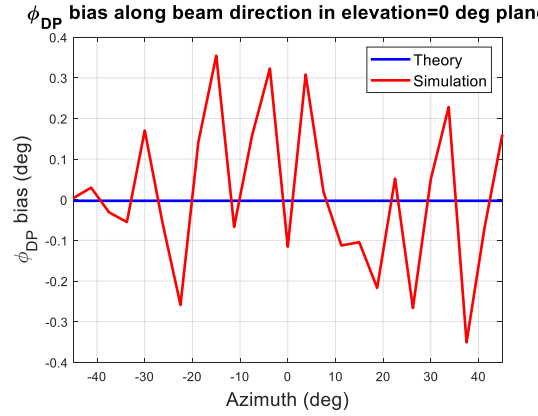

(e)

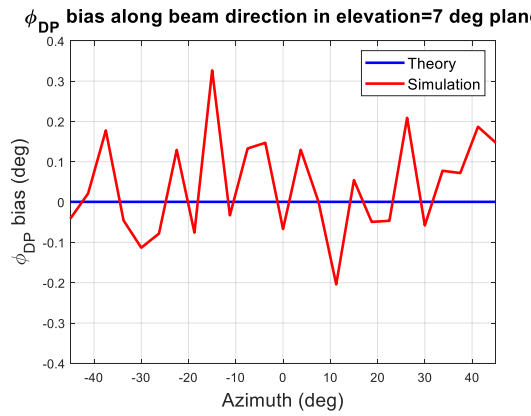

(f)

Figure 3-9 Theoretical and simulated polarimetric biases with CPPAR in observation of idealized uniform weather truth fields. The beam was steered 0 degrees (left column) and 7 degrees (right column) in elevation and ±45 degrees in azimuth with a step of 3.75 degrees. (a), (b) Z_{DR}. (c), (d) ρ_{hv}. (e), (f) ϕ_{DP}.

In addition, convective precipitation with a large reflectivity gradient is simulated, which was observed by KTLX radar (an operational NEXRAD) on 04:33:45 UTC on May 19th, 2013. A complete PPI image of reflectivity observed by KTLX is shown in Figure 3-10. The Level-II data at 0.5° elevation from KTLX radar are used as weather truth fields, and a sector spanning 90° in azimuth (45°~135°) which mainly consists of precipitation area is selected for CPPAR simulations. In principal plane (0 degrees elevation), the simulated sector images for Z_{H}, v_{r}, σ_{v}, Z_{DR}, ρ_{hv}, and ϕ_{DP} are presented in Figure 3-11. Besides, NEXRAD sector images are also provided as the ground truth for comparison. As shown in Figure 3-11, all the simulated CPPAR polarimetric radar estimates are generally consistent with KTLX measurements except for the difference in resolution, as a result of the much broader beamwidth.

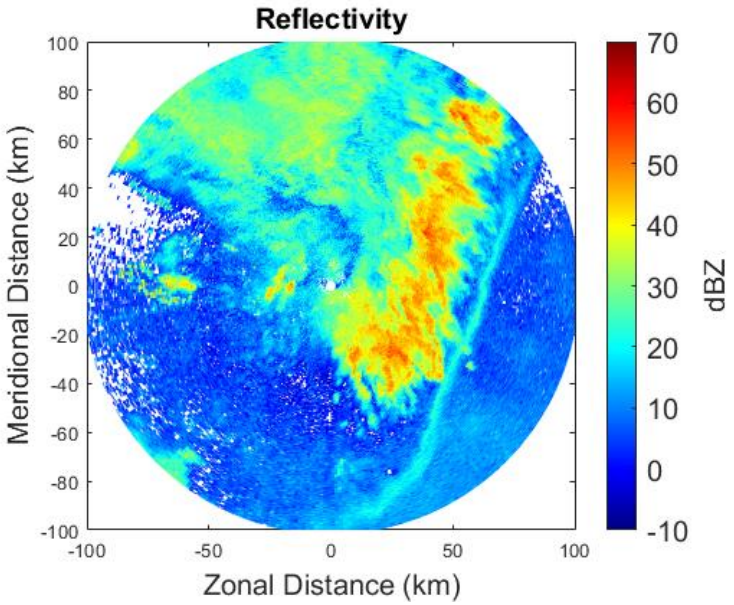

Figure 3-10 Reflectivity observed by KTLX at 04:33:45 UTC on May 19th, 2013.

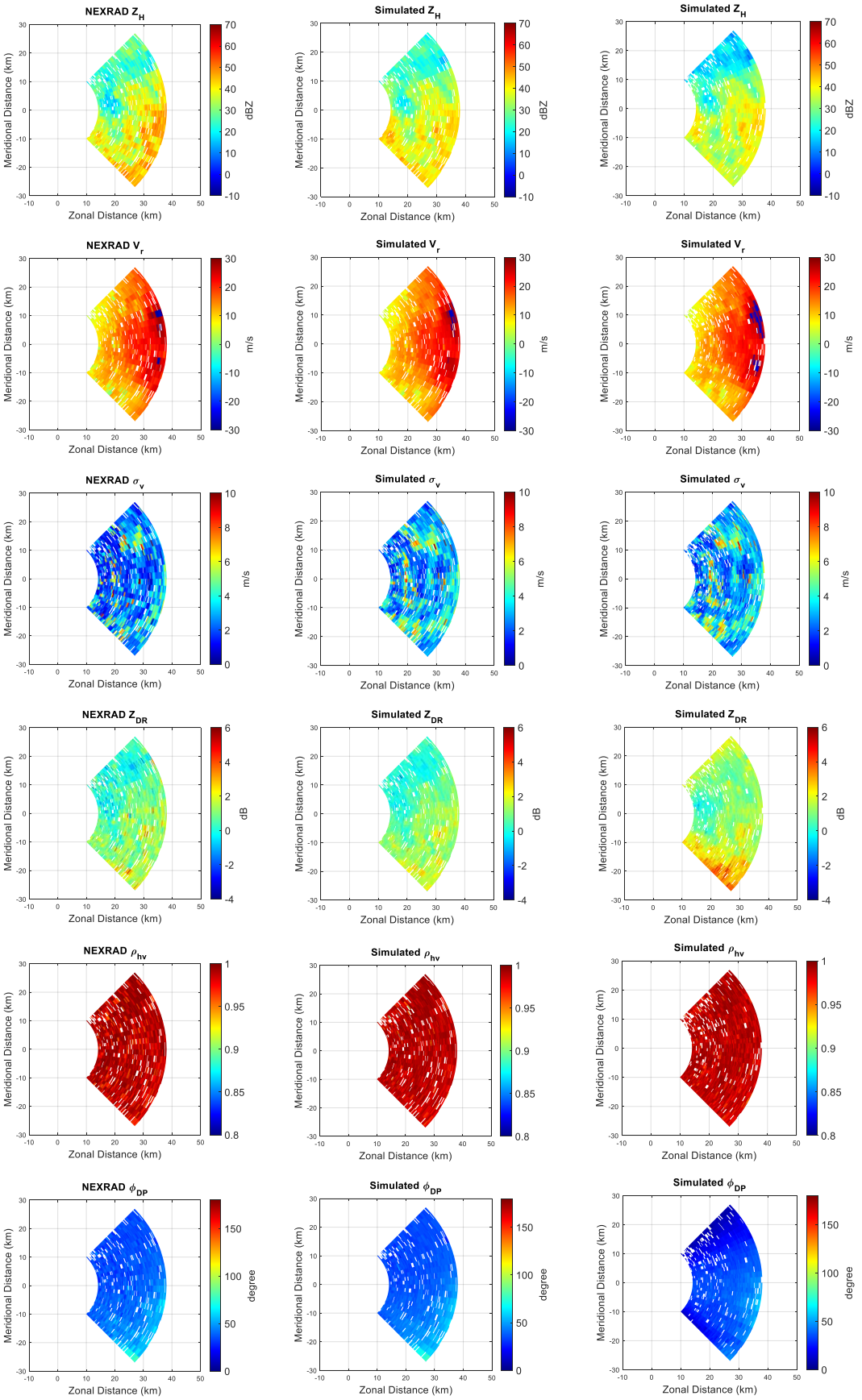

Figure 3-11 Comparison of NEXRAD weather truth fields (left column), and simulated polarimetric radar estimates with CPPAR (middle column) and TPD (right column).

3.6.2 PPPAR System

Simulation results of Ten Panel Demonstrator (TPD), which is a planar PPAR comprised of 40-by-16 elements, are also presented [55]. The technical specifications of the simulated TPD are listed in Table 3-3. The simulated TPD planar array and beam patterns are shown in Figure 3-12. For a fair comparison, the employed element patterns of TPD are the same as those used in CPPAR system simulation. The theoretical and simulated biases for Z_{DR}, ρ_{hv}, and ϕ_{DP} along beam-steering angle in azimuth are presented in Figure 3-13, for both principal plane (0 degrees elevation) and non-principal plane (7 degrees elevation). In addition, an example of actual weather measurements from the TPD proof-of-concept in stratiform precipitation on April 13th, 2017 are also provided in Figure 3-13. The weather fields were assumed to have similar parameters as $Z_{\mathrm{DR}} \approx 0\ dB$, $\rho_{\mathrm{hv}} \approx 0.99$, $\phi_{\mathrm{DP}} \approx 0^{\circ}$, in which case all the measured departures from these values were induced by the TPD radar system. These measurements were obtained in 0 degrees (array broadside points at the zenith) and 7 degrees (array broadside points at 7 degrees off the zenith) elevation plane, respectively. At each electronic beam-steering direction in azimuth, the mean values of estimates over range bins are calculated. The averaging in range was applied to reduce the standard deviation of estimates as it was assumed that the statistical properties of the scatterers were uniform along range.

Table 3-3 Technical specifications of the simulated TPD

Parameters	Values
Frequency	2870 MHz
Waveform	LFM
Peak power	6 W per element
Pulse width	20~80 μs
Pulse repetition time	1 ms
Receiver bandwidth	1 MHz
Noise figure	4.7 dB
Azimuth beamwidth	Transmit: 6.3°, Receive 7.4°
Elevation beamwidth	Transmit: 2.5°, Receive 3.0°
Radiating element	Patch
Array size	40 × 16
Sensitivity at 40km	11 dBZ

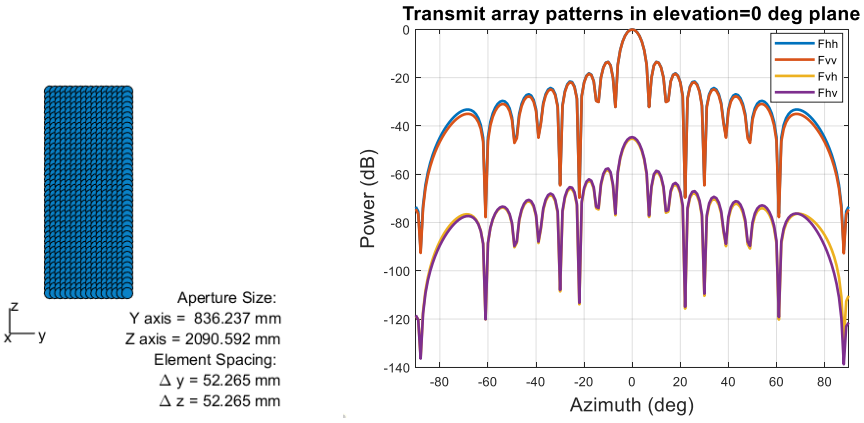

(a) (b)

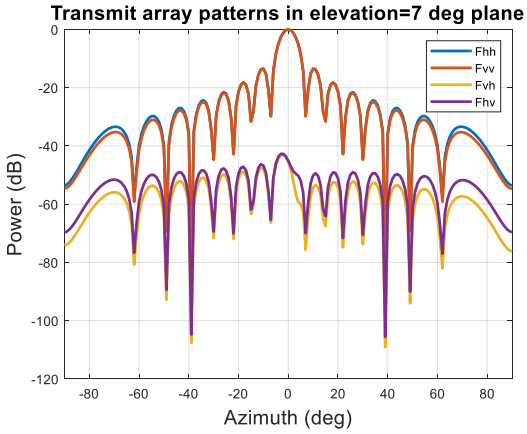

(c)

Figure 3-12 The simulated TPD and beam patterns. (a) TPD planar array. (b) Beam patterns in elevation=0 degrees plane. (c) Beam patterns in elevation=7 degrees plane.

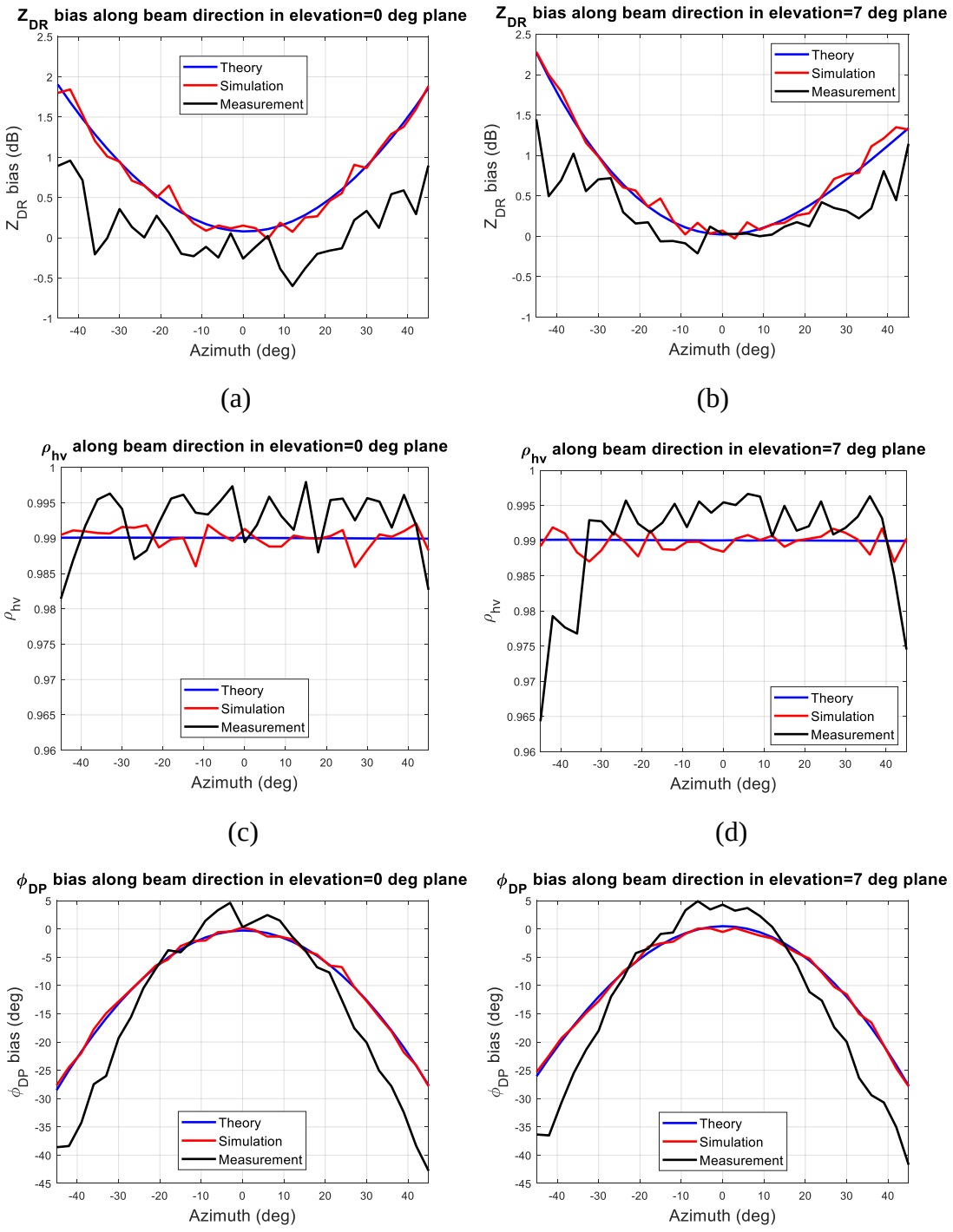

Figure 3-13 Theoretical, simulated, and measured polarimetric biases with TPD in a stratiform precipitation. The beam was steered 0 degrees (left column) and 7 degrees (right column) in elevation and ±45 degrees in azimuth with a step of 3 degrees. (a), (b) Z_{DR}. (c), (d) ρ_{hv}. (e), (f) ϕ_{DP}.

As shown in Figure 3-13, as the TPD beam is steered away from the broadside, both Z_{DR} and ϕ_{DP} biases increase a lot, while ρ_{hv} fluctuates around 0.99. In addition,

TPD proof-of-concept measurements exhibit comparable trends as theoretical predictions and simulation results, while their differences in magnitude may be due to the fact that the actual weather fields in these measurements are not ideally uniform as assumed. And the main reason for variations in measured results are the instabilities in the TPD hardware. It should be noted in Figure 3-13 (e) and (f) that the radome mounted on TPD proof-of-concept introduces an additional differential phase, which is larger than differential phase caused by array itself, and it has been documented in [56].

In addition, TPD simulation results in the observation of the convective precipitation used in Section 3.6.1 are also presented in Figure 3-11. As can be seen, when the TPD beam steers away from the broadside, Z_{DR} is overestimated while Z_{H} and ϕ_{DP} are underestimated, compared to the NEXRAD weather truth fields. These simulation results are consistent with those in Figure 3-13 and further validate that TPD requires calibration at each beam direction except the broadside.

In summary, the end-to-end system simulation results of CPPAR and TPD are both consistent with the theoretical predictions, which show that PASIM can accurately assess the impacts of system components, such as antenna patterns and channel electronics, on polarimetric radar data quality. Therefore, PASIM is an effective tool that connects the theoretical analysis and actual measurements for radar data quality evaluation.

3.7 Limitations and Future Work of PASIM

Currently, there are still some limitations of the PASIM simulations. First, for

simplicity, uniform drop size is assumed in weather returns modeling. However, to characterize the microphysical properties of precipitation, more realistic drop size distribution model such as Gamma distribution may be used. Second, for radar transceiver nonlinearity model, only the simple Saleh model is used in the current simulation, while a more accurate model for solid-state transceivers will be incorporated in the future, based on specific hardware designs and laboratory characterizations of them. In the next step, to further improve the fidelity of PASIM, better modeling of beam and channel mismatch between horizontal and vertical polarizations will be included. Besides, optimized nonlinear frequency modulation (NLFM) waveform and super-resolution algorithm can be studied. Further validation of PASIM using more measured weather data under various weather scenarios will be investigated.

In addition to system simulations, actual weather measurements of a few convective precipitation cases and a stratiform precipitation case made with the CPPAR, employing the single beam mechanical scan and commutating beam electronic scan respectively, are presented in Chapter 4 and the CPPAR performance is assessed.

Chapter 4 Weather Measurements and Performance Evaluation with the CPPAR

4.1 Data Collection and Scan Mode

Since summer 2019, CPPAR has been operated for testing and weather measurements, using the single beam mechanical scan and commutating beam electronic scan, respectively. Currently, the enabled observation sector in azimuth for the CPPAR ranges from 84 degrees to 212 degrees. During the scan, the CPPAR first rotates mechanically from 212 degrees to 84 degrees, stops scan, moves back to the specified beam position that is selected based on the area of interest of the weather scenario, and then steers the commutating beams electronically. Typically, the data sets of the two consecutive scans are collected 30 seconds apart. The key scanning parameters during these data collections are listed in Table 4-1, which were utilized in all the weather cases in Section 4.2. For the CPPAR demonstrator, each beam sector is comprised of 24 columns corresponding to 90 degrees in azimuth. During the electronic scan, the beam direction changes in azimuth by shifting a column of active elements. As a result, CPPAR has an azimuth sampling rate of 3.75 degrees. Compared with its azimuth beamwidth of 6.20 degrees, CPPAR has already realized “azimuth oversampling”. A pulse repetition time of 1 ms was chosen to achieve a maximum unambiguous range of 150 km and a maximum unambiguous velocity of 27 m/s. To mitigate the clutter effect on weather measurements, a notched filter was used to remove ground clutter. Besides, to reduce noise effects, one-lag estimators were employed [57]. Weather measurements of two convective precipitation cases and a

stratiform precipitation case are presented in Section 4.2. The weather returns from these three cases have different gradients of reflectivity and SNR, which are helpful for evaluating the performance of the CPPAR under various weather scenarios, such as the impacts from range sidelobes of pulse compression waveforms and antenna sidelobes of beam patterns.

As a baseline of data quality requirements for a polarimetric phased array radar such as the CPPAR, the NEXRAD specifications for data quality are listed in Table 4-2, which have mostly been accepted by the weather community. The accuracy and precision of weather radar estimates depend on several factors such as SNR, spectrum width, spatial resolution, etc. For example, the accuracy in the estimate of reflectivity shall be less than or equal to 1 dB at SNR greater than 10 dB, averaged over 1 km range bins [58-59].

Table 4-1 CPPAR parameters during data collection

Radar Parameters	**Mechanical Scan**	**Electronic Scan**
Frequency	2760 MHz	2760 MHz
Waveform	NLFM	NLFM
Pulse Width	34 μs	34 μs
Pulse Repetition Time	1 ms	1 ms
Pulses Per Dwell	64	64
Beam Sectors	1	25
Selected Beam Sector	Columns No.13~36	Columns No.1~24, 2~25, …, 25~48
Rotation Speed	11.75°/s	N/A
Azimuth Sampling Rate	0.75° per dwell	3.75° per dwell
Elevation Angle	3.3°	3.3°

Table 4-2 NEXRAD specifications for data quality

Radar Variable	Bias	Standard Deviation
Z_{H} (dB)	1	1
v_{r} (m/s)	1	1
σ_{v} (m/s)	1	1
Z_{DR} (dB)	0.1	0.2
ρ_{hv}	0.005	0.01
ϕ_{DP} (deg)	1	2

4.2 Weather Measurements

4.2.1 Case 1: Stratiform/Convective Multicell Storms

On 27 August 2019, measurements of a mixture of stratiform and convective multicell storms passing through Norman, Oklahoma were collected by the CPPAR. To see a larger picture of this weather case, a PPI image of reflectivity observed by KTLX is shown in Figure 4-1 for the same storm. Weather measurements including Z_{H}, v_{r}, σ_{v}, Z_{DR}, ρ_{hv}, and ϕ_{DP} collected by the CPPAR are presented in Figure 4-2. For visual comparison, corresponding measurements in the same area from KTLX are also shown as reference [60-61].

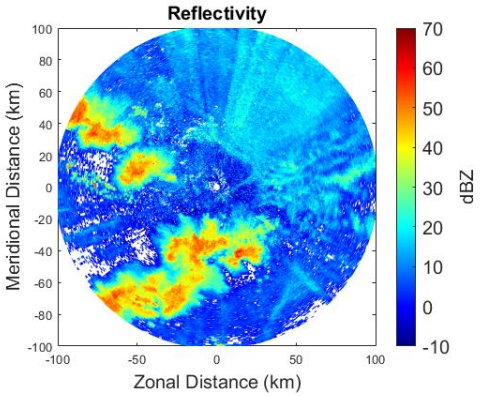

Figure 4-1 Reflectivity observed by KTLX at 05:06:10 UTC on 27 August 2019.

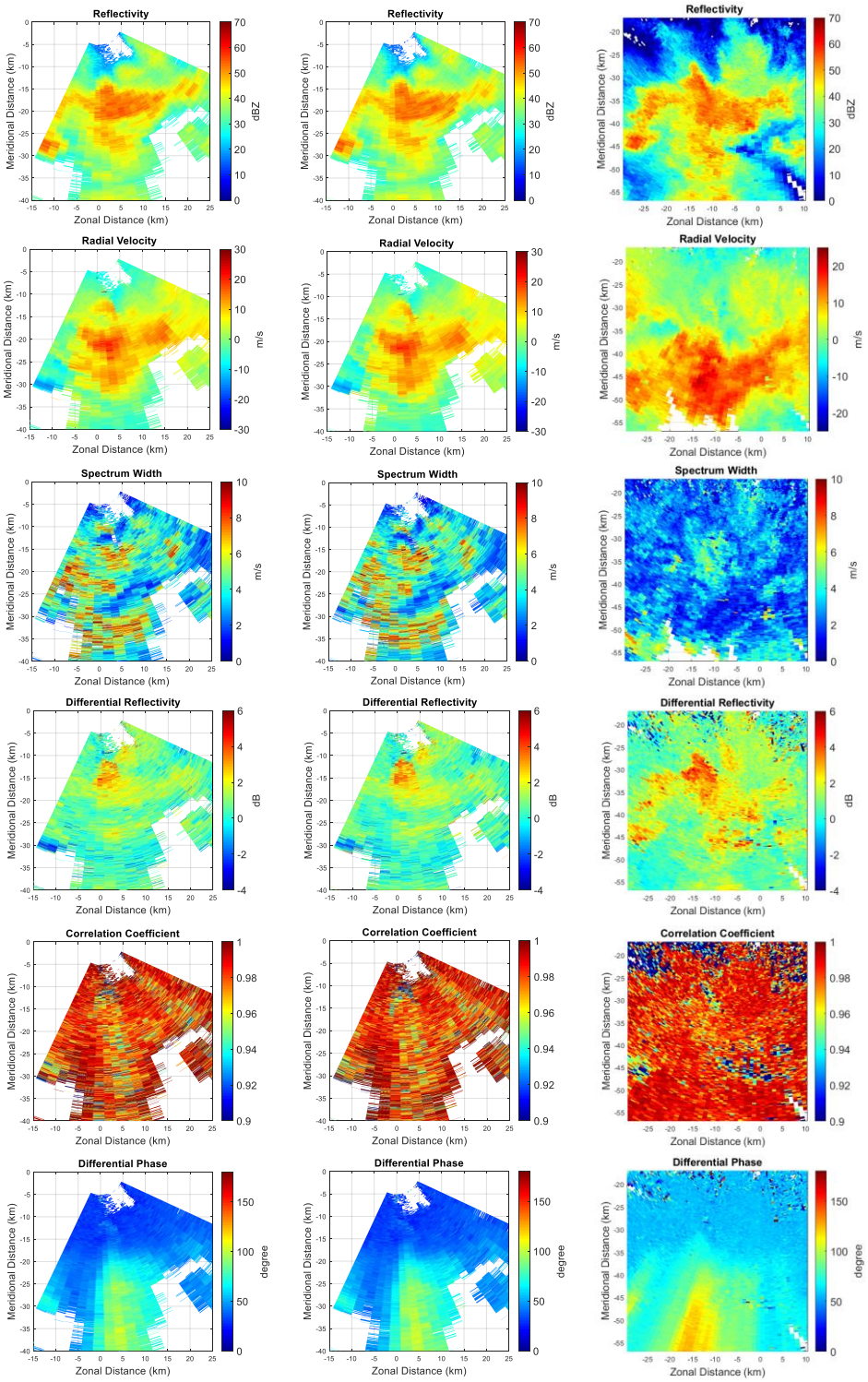

Figure 4-2 Weather measurements collected with CPPAR (SNR ≥ 5 dB) and KTLX on 27 August 2019. Left column: CPPAR mechanical scan at 05:03:40 UTC; middle column: CPPAR electronic scan at 05:04:04 UTC; right column: KTLX mechanical scan at 05:06:10 UTC.

As shown in Figure 4-2, the CPPAR electronic scan produces visually identical measurements as the mechanical scan. Moreover, CPPAR measurements are generally

consistent with KTLX observations except for the difference in resolution. It should be noted that the difference in v_{r} and ϕ_{DP} measurements is because the resolution volumes in precipitation are seen by CPPAR and KTLX from different radial directions. Furthermore, CPPAR produces higher estimates of σ_{v} due to its wider beam, which illuminates more weather scatterers in motion. In addition, one-one scatter plots between CPPAR mechanical scan and electronic scan are shown in Figure 4-3.

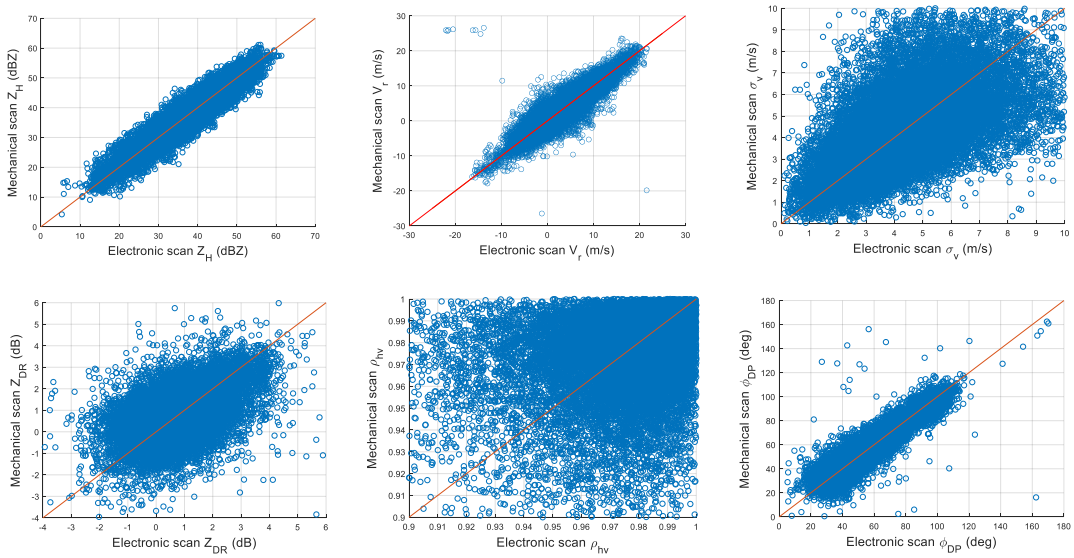

Figure 4-3 Scatter plots of CPPAR measurements of precipitation (SNR ≥ 5 dB).

For quantitative comparison of CPPAR measurements between electronic scan and mechanical scan, it is more straightforward to reduce noise effects by using high SNR data (see Fig. 8 in [62]), thus a threshold of SNR ≥ 20 dB was used to filter the raw data for error analysis. Error statistics are listed in Table 4-3, in which the mean bias (MB) and "global" standard deviation (STD) are defined as

$$\mathrm{MB} = \frac{1}{\mathrm{N}}\sum_{\mathrm{n}=1}^{\mathrm{N}}(e_{\mathrm{n}} - m_{\mathrm{n}}) \tag{4-1}$$

$$\mathrm{STD} = \sqrt{\frac{1}{\mathrm{N}}\sum_{\mathrm{n}=1}^{\mathrm{N}}(e_{\mathrm{n}} - m_{\mathrm{n}})^2} \tag{4-2}$$

where e is the measurement value from electronic scan, and m is the measurement

value from mechanical scan. It should be noted that the global STD includes two sources of error, one comes from random fluctuation due to sampling error, the other results from the inhomogeneity of weather scatterers due to temporal and spatial difference of the two scans. In this weather case, two CPPAR scans were made with the 24 seconds apart imposed by the scan mode switch time, during which the positions and velocities of weather scatterers in the resolution volume may have changed. The random fluctuation due to sampling error of the CPPAR is more important for system data quality analysis, which is referred as "Local STD". The local STD is estimated from radar estimates over 11 gates (range gate No.1-11, 2-12, 3-13, ……) in each beam and corresponding histograms for the electronic scan are shown in Figure 4-4. Then the estimated local STD of each radar estimate can be obtained from the median value of corresponding histogram. The theoretical STD of radar estimates can also be calculated using the measured median value of σ_{v} and ρ_{hv}, based on the equations in [1-2, 57], which are simplified based on high SNR and listed below, where the subscript 1 of radar estimate refers to one-lag estimator.

$$\mathrm{SD}(\hat{Z}_{\mathrm{H1}}) = 10\log_{10}(1 + 1/\sqrt{M_{\mathrm{I}}}) \tag{4-3}$$

$$\mathrm{SD}(\hat{v}_{\mathrm{r}}) = \frac{\lambda}{4\pi\rho(T_{\mathrm{s}})T_{\mathrm{s}}\sqrt{2M_{\mathrm{I}}}}[1 - \rho^2(T_{\mathrm{s}})] \tag{4-4}$$

$$\mathrm{SD}(\hat{\sigma}_{\mathrm{v1}}) = \sqrt{\frac{\lambda^2}{576\pi^4 T_{\mathrm{s}}^2 \sigma_{\mathrm{vn}}^2}(A + B + C)} \tag{4-5}$$

$$\mathrm{SD}(\hat{Z}_{\mathrm{DR1}}) = \frac{10}{\rho(T_{\mathrm{s}})\ln 10}\sqrt{\frac{(1-\rho_{\mathrm{hv}}^2)(1+\rho^2(T_{\mathrm{s}}))}{M_{\mathrm{I1}}}} \tag{4-6}$$

$$\mathrm{SD}(\hat{\rho}_{\mathrm{hv1}}) = \frac{1-\rho_{\mathrm{hv}}^2}{2\rho(T_{\mathrm{s}})}\sqrt{\frac{(1+\rho^2(T_{\mathrm{s}}))}{M_{\mathrm{I1}}}} \tag{4-7}$$

$$\mathrm{SD}(\hat{\phi}_{\mathrm{DP}}) = \frac{180}{\pi\rho_{\mathrm{hv}}}\sqrt{\frac{1-\rho_{\mathrm{hv}}^2}{2M_{\mathrm{I}}}} \tag{4-8}$$

where $M_{\mathrm{I}} = MT_{\mathrm{s}}/(\tau_{\mathrm{c}}\sqrt{\pi})$ is the number of independent samples within the dwell

time, M is the number of samples (pulses), T_s is pulse repetition time, and τ_c is the correlation time defined as $\tau_c = \lambda/(4\pi\sigma_v)$, the time correlation term is expressed as $\rho(nT_s) = e^{-(nT_s)^2/(2\tau_c^2)}$, and σ_{vn} is the normalized spectrum width defined as $\sigma_{vn} = 2\sigma_v T_s/\lambda$, the expression of A, B, and C can be found in Eq. (6.33) in [1], M_{I1} is the number of independent samples within the dwell time for one-lag estimator, defined as $M_{I1} = (M-1)T_s/(\tau_c\sqrt{\pi})$. It should be noted that Eq.(4-8) is valid for a large number of samples M.

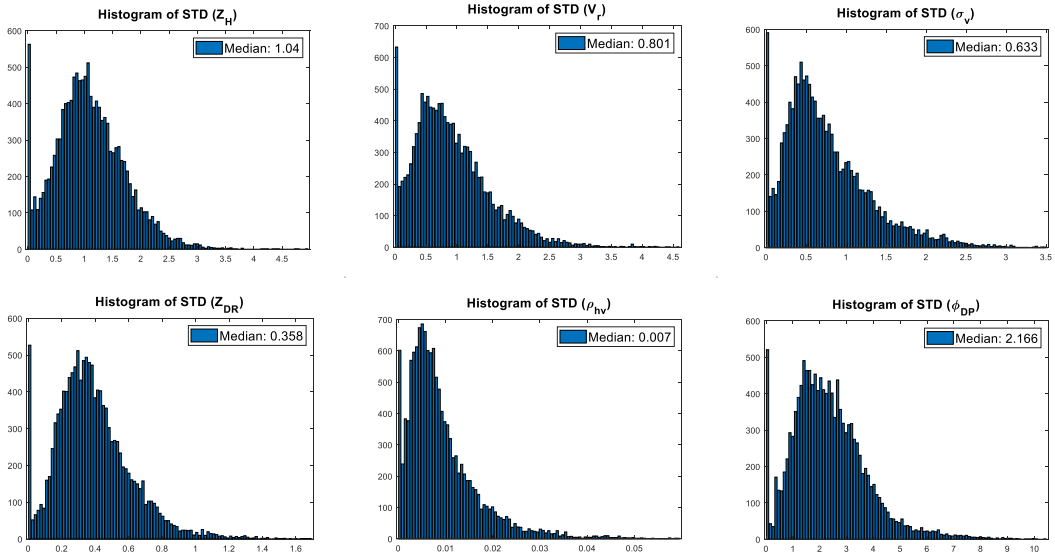

Figure 4-4 Histograms of STD of radar estimates in electronic scan (SNR ≥ 20 dB).

Table 4-3 Error statistics of CPPAR measurements based on comparison between electronic and mechanical scans

Moment	Mean Bias	Global STD	Local STD	STD of Estimates	STD in theory
Z_H (dB)	0.23	2.52	1.54	1.04	0.94
v_r (m/s)	-0.15	2.10	1.19	0.80	0.76
σ_v (m/s)	-0.04	1.75	0.96	0.63	0.56
Z_{DR} (dB)	-0.01	0.82	0.51	0.36	0.31
ρ_{hv}	0.001	0.021	0.011	0.007	0.007
ϕ_{DP} (deg)	-0.18	5.08	3.16	2.17	1.94

As shown in Table 4-3, the STD of the CPPAR estimates (second column from right) and STD in theory (last column) are generally very consistent for electronic scan, which may potentially meet the requirements of NEXRAD specifications for data quality.

4.2.2 Case 2: Severe Thunderstorms

On 8 May 2020, measurements of a severe thunderstorm were collected with the CPPAR. A PPI image of reflectivity observed by KTLX is shown in Figure 4-5 for the same storm. Weather measurements with the CPPAR and corresponding observations in the same area from KTLX are presented in Figure 4-6. In addition, scatter plots between CPPAR mechanical scan and electronic scan are shown in Figure 4-7. The histograms of the local STD of radar estimates for the electronic scan are shown in Figure 4-8. And the error statistics are listed in Table 4-4.

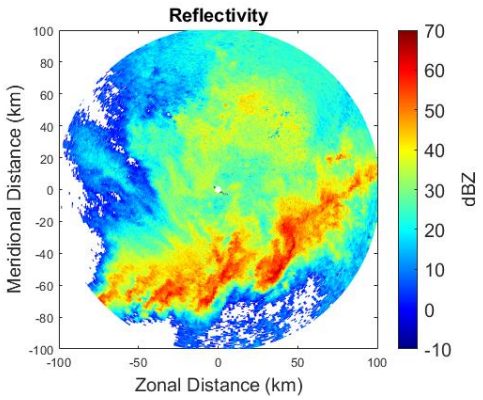

Figure 4-5 Reflectivity observed by KTLX at 06:48:37 UTC on 8 May 2020.

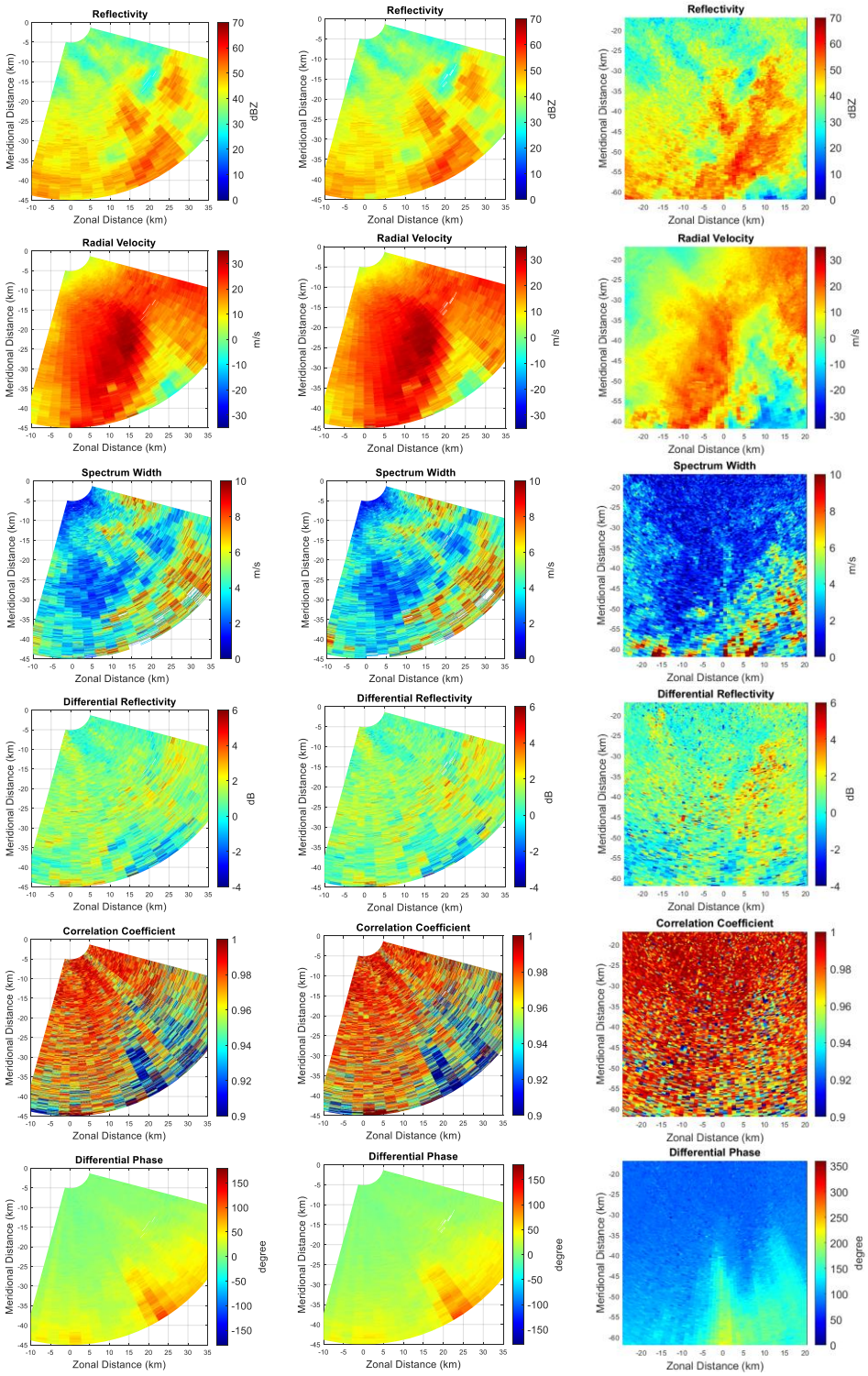

Figure 4-6 Weather measurements collected with CPPAR (SNR ≥ 5 dB) and KTLX on 8 May 2020. Left column: CPPAR mechanical scan at 06:50:21 UTC; middle column: CPPAR electronic scan at 06:50:54 UTC; right column: KTLX mechanical scan at 06:48:37 UTC.

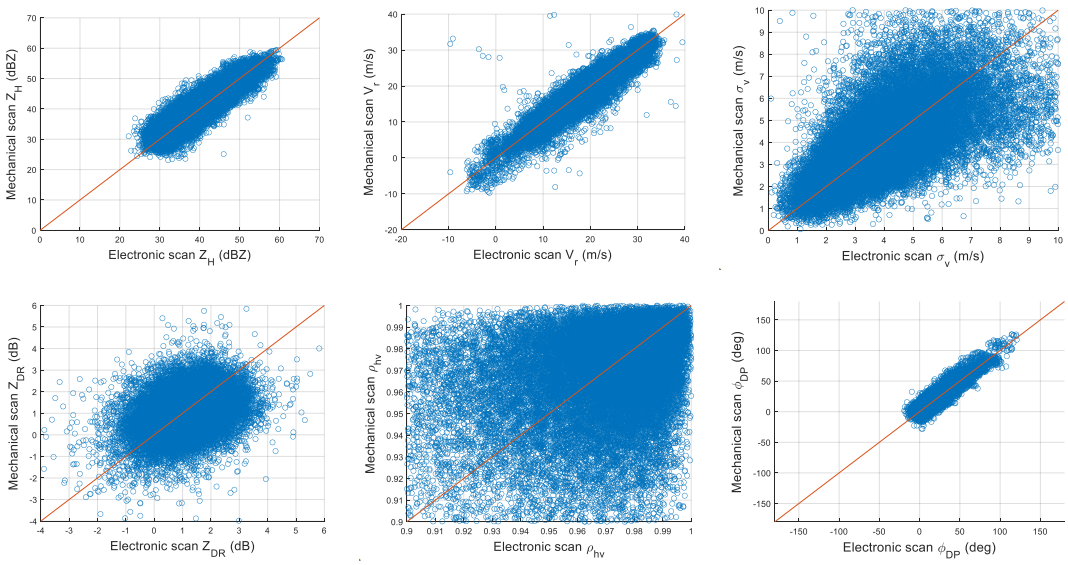

Figure 4-7 Scatter plots of CPPAR measurements of precipitation (SNR ≥ 5 dB).

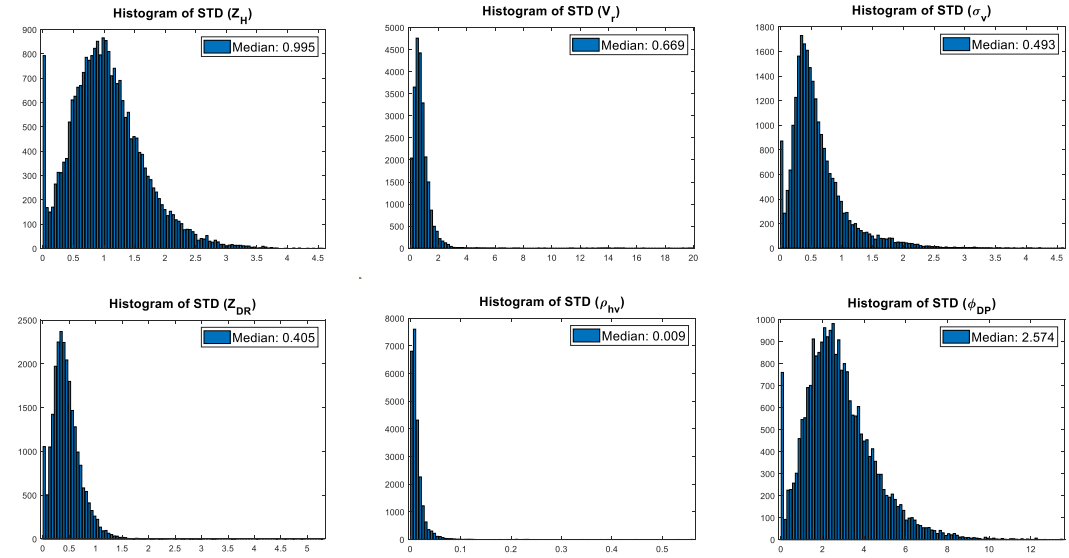

Figure 4-8 Histograms of STD of radar estimates in electronic scan (SNR ≥ 20 dB).

Table 4-4 Error statistics of CPPAR measurements based on comparison between electronic and mechanical scans

Moment	Mean Bias	Global STD	Local STD	STD of Estimates	STD in theory
Z_H (dB)	-0.07	2.56	1.45	1.00	1.03
v_r (m/s)	0.50	2.34	0.95	0.67	0.66
σ_v (m/s)	-0.02	1.45	0.71	0.49	0.46
Z_{DR} (dB)	0.07	1.01	0.57	0.41	0.37
ρ_{hv}	0.002	0.048	0.015	0.009	0.009
ϕ_{DP} (deg)	-1.00	6.95	3.67	2.57	2.36

As shown in Table 4-4, the STD of the CPPAR estimates (second column from right) and STD in theory (last column) are very consistent for electronic scan, which may potentially meet the requirements of NEXRAD specifications for data quality.

In addition, it is found that in the southeastern region of CPPAR images, the weather returns have low ρ_{hv}, which might be caused by non-uniform beam filling where the CPPAR beam captures a gradient of precipitation types within the beam. To validate, the hydrometeor classification product from NEXRAD Level-III data are presented in Figure 4-9, which confirms that the corresponding returns in black circle are mainly comprised of hail, graupel, and heavy rain. It should be noted that in the black circle, the measured ρ_{hv} with the CPPAR is lower than that with KTLX. This is because the CPPAR's wide beam illuminates more weather scatterers and the effect of non-uniform beam filling is even larger.

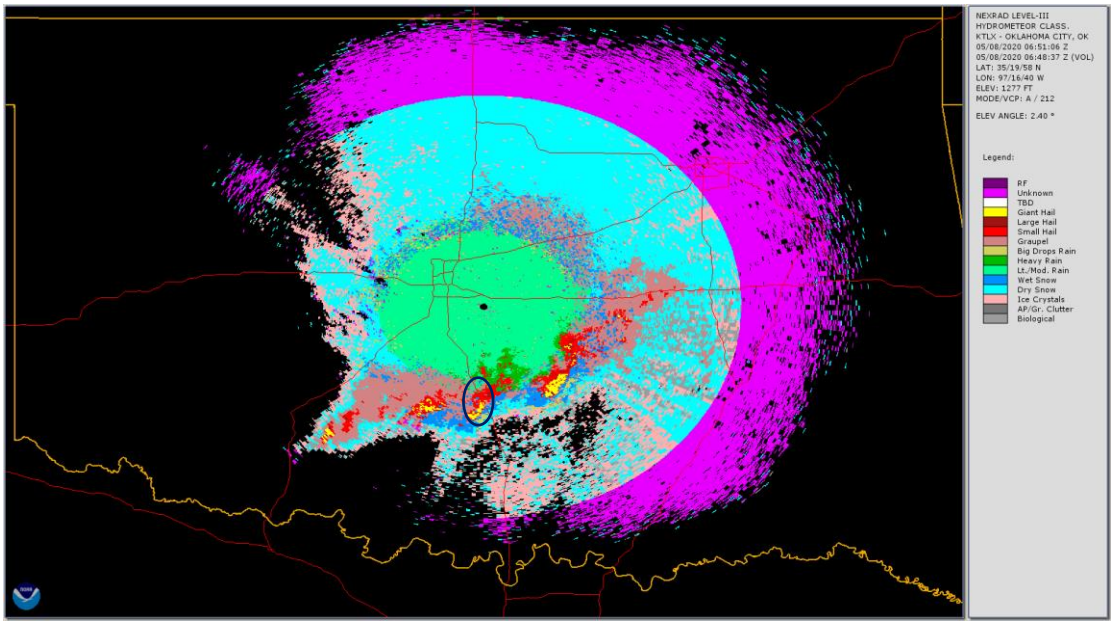

Figure 4-9 Hydrometeor Classification product of KTLX at 06:48:37 UTC on 8 May 2020.

4.2.3 Case 3: Stratiform Precipitation

On 25 May 2020, measurements of a stratiform precipitation were collected with the CPPAR. A PPI image of reflectivity observed by KTLX is shown in Figure 4-10. Weather measurements with the CPPAR and corresponding observations in the same area from KTLX are presented in Figure 4-11. In addition, scatter plots between CPPAR mechanical scan and electronic scan are shown in Figure 4-12. The histograms of the local STD of radar estimates for the electronic scan are shown in Figure 4-13. And the error statistics are listed in Table 4-5.

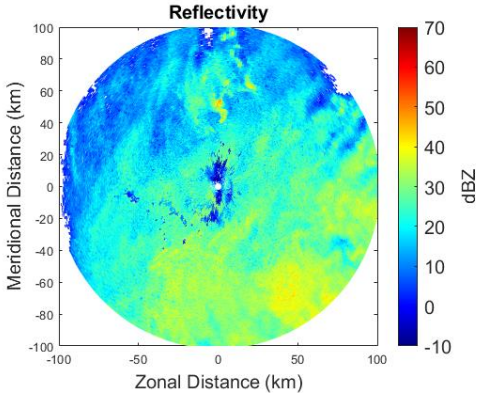

Figure 4-10 Reflectivity observed by KTLX at 20:33:52 UTC on 25 May 2020.

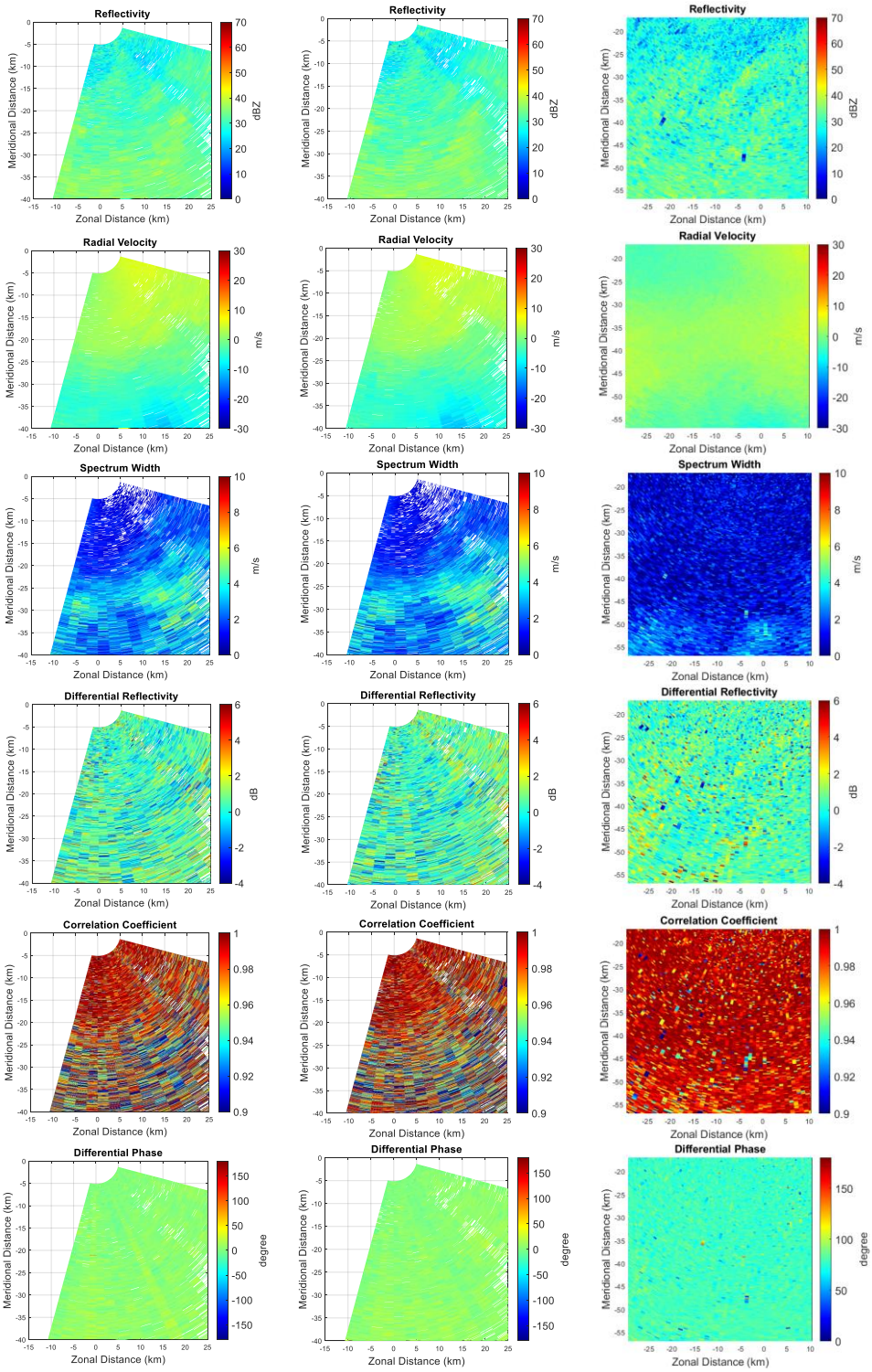

Figure 4-11 Weather measurements collected with CPPAR (SNR ≥ 5 dB) and KTLX on 25 May 2020. Left column: CPPAR mechanical scan at 20:30:40 UTC; middle column: CPPAR electronic scan at 20:31:04 UTC; right column: KTLX mechanical scan at 20:33:52 UTC.

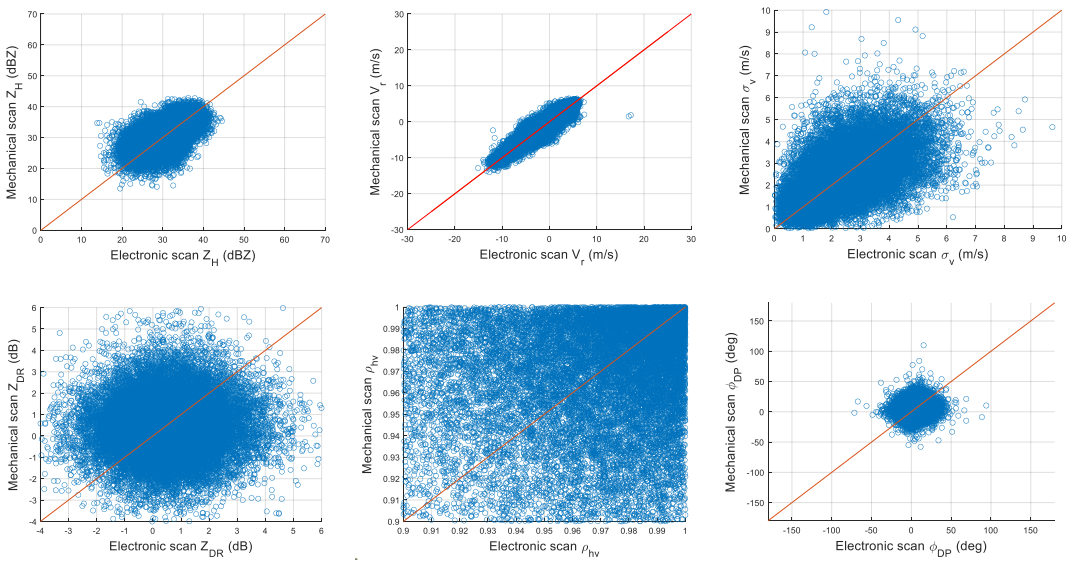

Figure 4-12 Scatter plots of CPPAR measurements of precipitation (SNR ≥ 5 dB).

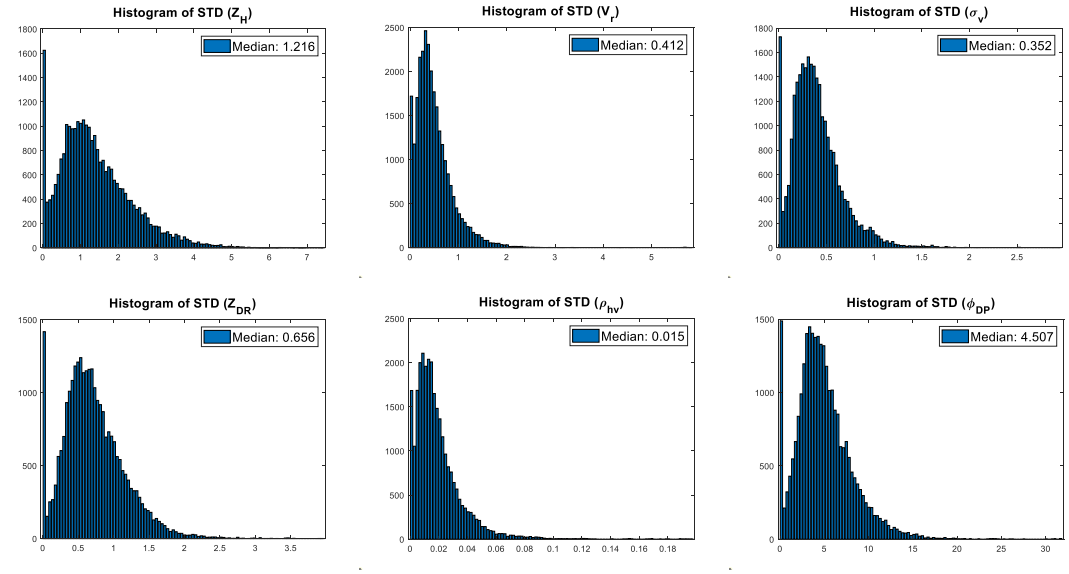

Figure 4-13 Histograms of STD of radar estimates in electronic scan (SNR ≥ 10 dB).

Table 4-5 Error statistics of CPPAR measurements based on comparison between electronic and mechanical scans

Moment	Mean Bias	Global STD	Local STD	STD of Estimates	STD in theory
Z_H (dB)	-0.11	3.39	1.84	1.22	1.31
v_r (m/s)	0.02	1.15	0.55	0.41	0.46
σ_v (m/s)	0.01	0.82	0.45	0.35	0.33
Z_{DR} (dB)	0.05	1.56	0.91	0.66	0.39
ρ_{hv}	0.001	0.045	0.022	0.015	0.008
ϕ_{DP} (deg)	0.17	10.99	6.18	4.51	2.51

As shown in Table 4-5, the STD of the CPPAR polarimetric estimates (second column from right) are generally higher than corresponding STD in theory (last column) for electronic scan. A possible reason is that the low SNR of the radar returns in the stratiform precipitation results in higher estimation error.

According to the error statistics of the three weather cases, it can be found that low SNR and large reflectivity gradient have more impact on polarimetric radar variables than spectral moments, as radar estimates from both horizontal and vertical polarizations are affected simultaneously.

Next, a theoretical explanation of a feature of the commutating beam electronic scan in clutter detection that is different from mechanical scan is presented and verified with the CPPAR in Chapter 5. Also, clutter detection results in both electronic scan and mechanical scan modes are also compared.

Chapter 5 Clutter Detection with the CPPAR

5.1 Introduction

In weather radar observations, ground clutter degrades radar data quality by biasing Doppler and polarimetric radar measurements and hence affect quantitative precipitation estimation. Therefore, it is important to detect clutter and mitigate its effects as much as possible. For weather radar, ground clutter refers to the undesired returns from natural or man-made objects on the ground, which typically have zero mean Doppler velocity and narrow spectrum width. A conventional clutter filtering method utilizes a band-stop filter with a fixed notch width to mitigate the clutter effects [63]. However, this method will remove some spectral components of narrow-band weather signals with near-zero radial velocity and thus bias Doppler and polarimetric radar estimates [64]. In addition, it is acknowledged that clutter filtering should not be applied at all the range bins, especially for radar signals without clutter contamination but having a small Doppler velocity [62]. Therefore, it is better to first identify if a radar resolution volume has been contaminated by ground clutter, and then apply a proper filter to mitigate the clutter effect.

Traditionally, a static clutter map obtained in clear-air conditions is used to identify the locations of resolution volumes contaminated by ground clutter and mitigate its impact on the weather measurements by filtering [65]. While the clutter map works for a stable clutter environment, it cannot adapt to the temporal variations in the clutter and the presence of anomalous propagation due to super-refractivity in the lower atmosphere. Therefore, an adaptive ground clutter detection algorithm is required

to detect ground clutter. Hubbert et al. [66-67] introduced a clutter mitigation decision (CMD) algorithm by combining clutter phase alignment (CPA), texture of reflectivity, and spatial variability of reflectivity field (SPIN), which is currently used in the radar data acquisition (RDA) subsystem of NEXRAD. Torres and Warde [68-69] proposed the Clutter Environment Analysis using Adaptive Processing (CLEAN-AP) filter, which automates the detection and mitigation of ground clutter contamination using the autocorrelation spectral density, which is being tested for inclusion in the NEXRAD radar network [2].

In recent years, weather radar polarimetry is widely utilized in clutter detection and mitigation, as ground clutter and weather scatterers have different polarimetric properties. Li et al. [70] proposed a simple Bayesian classifier (SBC) to distinguish ground clutter from weather signals, according to their different statistical properties in terms of power ratio, differential reflectivity, and copolar correlation coefficient. In addition, based on the difference in spectral properties between clutter and weather signals, Li et al. [71] introduced a spectrum clutter identification (SCI) algorithm that utilizes spectral power distribution, spectral phase fluctuation, power texture, and spectrum width texture as discriminants for clutter detection.

Most recently, based on the observations that the phase fluctuations of ground clutter are typically slower than those of the randomly distributed hydrometeors, phase information of time series samples for each radar resolution volume is utilized in clutter detection. Golbon-Haghighi et al. [72] introduced the phase fluctuation index (PFI) and employed the polynomial fitting function to discriminate clutter from weather signals.

Further, it is found that the phase structure function (PSF) of horizontal and vertical polarizations, in combination with the dual-scan cross-correlation coefficient which is based on the difference in correlation time between weather and clutter, has a good separation between clutter and weather probability density functions even under low clutter-to-signal ratio (CSR) [73].

While there have been numerous research work conducted in clutter detection and filtering mentioned above, nearly all of them are designed for weather radar with mechanical scan. In this chapter, clutter detection methods are explored and compared for the CPPAR with electronic scan and mechanical scan, respectively.

5.2 Clutter Characteristics in Electronic Scan

Normally, individual stationary ground clutter such as water towers will have very high ρ_{hv}. According to the definition of ρ_{hv} [2],

$$\rho_{\mathrm{hv}} = |\langle n s_{\mathrm{hh}}^{*}(\pi) s_{\mathrm{vv}}(\pi)\rangle| / \sqrt{\langle n|s_{\mathrm{hh}}(\pi)|^2\rangle\langle n|s_{\mathrm{vv}}(\pi)|^2\rangle} \tag{5-1}$$

where $s_{\mathrm{hh}}(\pi)$ and $s_{\mathrm{vv}}(\pi)$ are backscattering amplitudes for horizontal and vertical polarizations, and the angular brackets $\langle\cdots\rangle$ denote the ensemble average. The first item in (5-1) can be further expanded as

$$\langle n s_{\mathrm{hh}}^{*}(\pi) s_{\mathrm{vv}}(\pi)\rangle = \langle n|s_{\mathrm{hh}}(\pi)||s_{\mathrm{vv}}(\pi)|\rangle e^{-\sigma_{\delta}^2/2} e^{j\delta} \tag{5-2}$$

where the mean scattering phase difference is $\delta = \langle \delta_{\mathrm{h}} - \delta_{\mathrm{v}} \rangle$ that can bias the ϕ_{DP} estimate, and its standard deviation is $\sigma_{\delta} = STD(\delta_{\mathrm{h}} - \delta_{\mathrm{v}})$ that causes decorrelation. Therefore, ρ_{hv} is reduced by a factor of $e^{-\sigma_{\delta}^2/2}$ due to random scattering phase difference in the case of melting snow, hail, and biological scatterers, as well as distributed ground clutter such as mountain, trees, etc. [2].

In the mechanical scan mode, there is always the beam smearing effect and the change of the scattering phase difference due to the fast rotation of the antenna, which will increase σ_δ of ground clutter. As a result, the measured ρ_{hv} of ground clutter will be reduced. As an explanation, Figure 5-1 illustrates the changing differential scattering phase of distributed ground clutter in the mechanical scan. At the initial instant T1, scatterers (represented as solid black circles) are assumed to move horizontally towards the east, while the radar beam is pointing vertically to the north. Therefore, in the radar field of view, these scatterers' radial velocity is zero. However, as the antenna rotates mechanically, at the next instant T2, there is a radial component of velocity shown as blue arrow appearing, as a result, the radial velocity of the scatterers seen by the radar becomes nonzero, so the measured spectrum width will increase. Besides, as the scatterers observed by the radar are not the same at these two instants, their contribution to the returned signals change, and hence differential scattering phase $\delta_{\mathrm{h}} - \delta_{\mathrm{v}}$ changes, ρ_{hv} reduces. In addition, the extent to which ρ_{hv} reduces in the mechanical scan is closely related with antenna rotation speed, beamwidth, and dwell time. On the one hand, as the antenna rotates faster, the radial component of velocity and spectrum width increases more, differential scattering phase changes more violently, the reduction in ρ_{hv} will be more. On the other hand, under the same antenna rotation speed, the wider the beamwidth, the smaller change in differential scattering phase of the scatterers, the reduction in ρ_{hv} will be less. If the dwell time is short, then the change in differential scattering phase is smaller, but the error of the radar estimates will go up as a tradeoff. It should be noted that Figure 5-1 applies to the traditional

continuous mechanical scan mode. If a stepped mechanical scan mode is used, then the reduction in ρ_{hv} will be less.

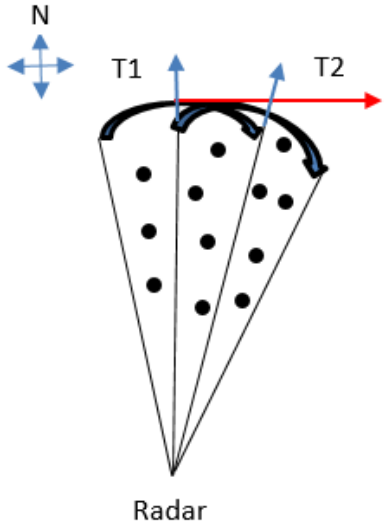

Figure 5-1 An illustration of changing differential scattering phase in the continuous mechanical scan.

In contrast, the commutating scan mode has no beam smearing effect as it electronically steers the beam, hence the σ_δ of ground clutter is much lower, which yields the higher ρ_{hv}. This is fundamentally different from the reduced ρ_{hv} for clutter in mechanical scan measurements. Therefore, attention is needed in interpreting electronic PAR measurements.

To validate this assumption, ρ_{hv} measured in clear air condition are compared as follows [60]. As indicated in Table 4-1, azimuth sampling rate is 0.75° per dwell for mechanical scan and 3.75° per dwell for electronic scan of the CPPAR demonstrator, respectively. To make a fair comparison, azimuth sampling rate should be the same for the two scan modes. A possible solution is to combine every 5 consecutive radials in the mechanical scan into a new radial, which corresponds to an equivalent azimuth sampling rate of 3.75° per dwell. The processed results are presented in Figure 5-2. The

measurements in the clear air condition were collected at 01:09:32 UTC for the mechanical scan and 01:09:54 UTC for the electronic scan on 31 August 2019. For comparison purposes, measurements from the mechanical scan processed with the raw single radial are also included. It should be noted that all the results in Figure 5-2 are before clutter filtering, so that the performances of various scan modes in clutter detection can be compared in a fair way.

As shown in Figure 5-2, due to the change in differential scattering phase during the scan, ρ_{hv} measured from the mechanical scan with combined radials is lower for ground clutter within 10 km, as shown in blue pixels, compared with that from the electronic scan. As a comparison, ρ_{hv} measured from mechanical scan with raw single radial shows some reduction, but not as serious as the combined beam. The reason is that the azimuth sampling rate of 0.75° per dwell for mechanical scan is only about one eighth of the beamwidth of the CPPAR demonstrator, so the change in differential scattering phase of ground clutter during the scan is much smaller.

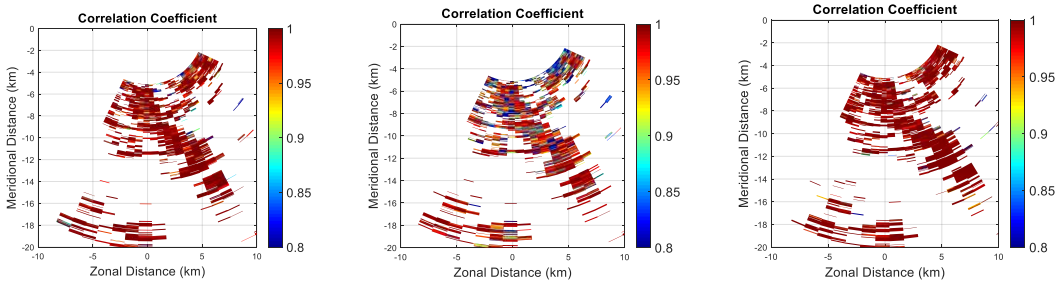

(a) (b) (c)

Figure 5-2 Comparison of ρ_{hv} under various scan modes in clear air condition. (a) Mechanical scan with single radial. (b) Mechanical scan with combined radials. (c) Electronic scan.

To further validate this assumption, ground clutter measurements with the CPPAR are obtained and compared directly. On 17 May 2020, ground clutter

measurements were collected in the clear air condition using a 1 μs simple rectangular pulse without applying notched filter to the received time series. It should be noted that as the CPPAR has a wide beamwidth, to enhance the beam broadening effect of mechanical scan, the number of pulses in the dwell time is set at 256 for both mechanical scan and electronic scan during data collection for the purpose of clutter detection comparison. The measured ρ_{hv} and corresponding histogram in clear air conditions with mechanical scan at 23:00:20 UTC on 17 May 2020 and electronic scan at 22:57:40 UTC on 17 May 2020 are shown in Figure 5-3.

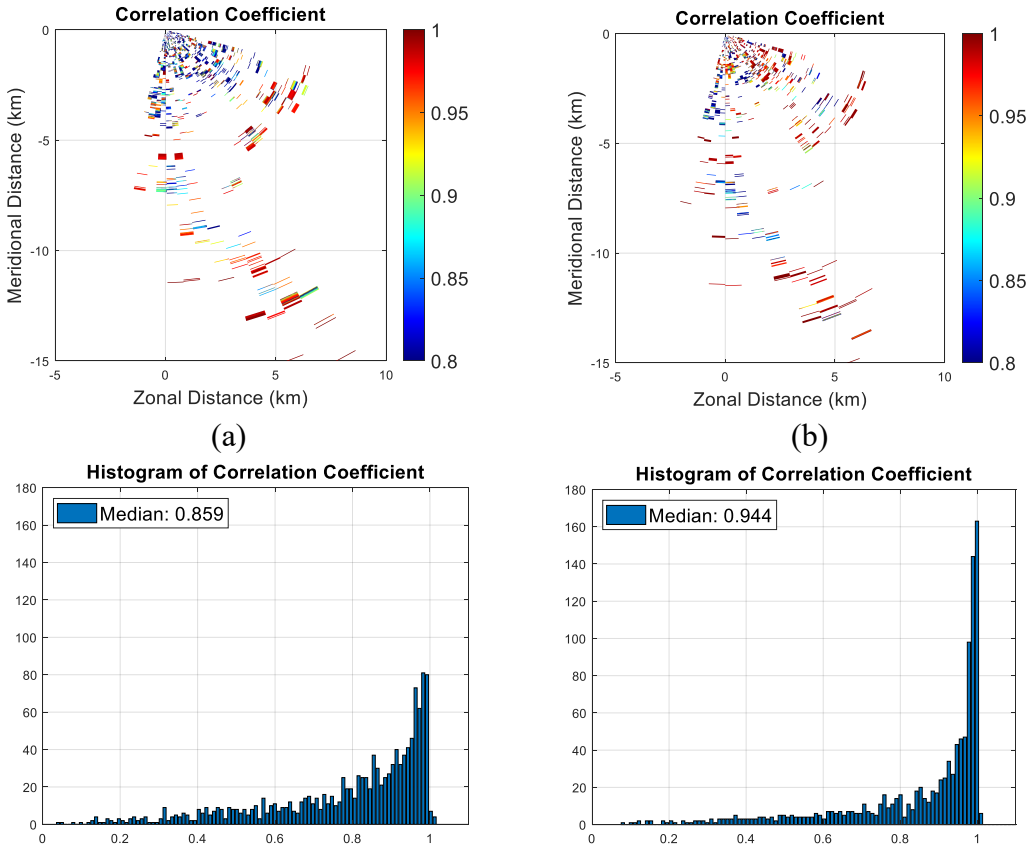

Figure 5-3 Measured ρ_{hv} and histogram in clear air conditions with mechanical scan at 23:00:20 UTC on 17 May 2020 and electronic scan at 22:57:40 UTC on 17 May 2020. (a) ρ_{hv} in mechanical scan. (b) ρ_{hv} in electronic scan. (c) Histogram of ρ_{hv} in mechanical scan. (d) Histogram of ρ_{hv} in electronic scan.

As shown in Figure 5-3, ρ_{hv} measured with mechanical scan is lower for ground clutter within 5 km, as shown in blue pixels, compared with that with the electronic scan. Besides, the median value of corresponding histograms of ρ_{hv} also confirms this. The median value of histogram of ρ_{hv} in mechanical scan is 0.859, whereas the median value of histogram of ρ_{hv} in electronic scan is 0.944. On the one hand, these observations validate the assumption that electronic scan yields higher ρ_{hv} than mechanical scan for ground clutter. On the other hand, it indicates that it is more challenging for clutter detection with electronic scan, as clutter has similar ρ_{hv} as weather returns.

5.3 Clutter Detection with the CPPAR

5.3.1 Data Sets

To evaluate the effectiveness of the discriminant function, controlled data sets, including pure clutter I/Q data and pure weather I/Q data are required. As the CPPAR currently works at a fixed elevation angle of 3.3 degrees, pure clutter data can be collected in clear air conditions using a 1 μs simple rectangular pulse without applying a notched filter to the received time series. In that case, the blind range is only 150 m and hence more near-range ground clutter can be collected. Then the clutter data are edited by retaining those resolution volumes with radial velocity $v_{\mathrm{r}} \leq 1 m/s$ and spectrum width $\sigma_{\mathrm{v}} \leq 1 m/s$. This step is to ensure the clutter field is not contaminated by moving targets such as birds and aircraft. On the other hand, pure weather data can be collected in precipitation using a 34 μs NLFM waveform and applying a notched filter with a large notch width to the received time series to mitigate the clutter effect

as much as possible. In addition, to reduce noise impact on clutter detection, a threshold of SNR ≥ 10 dB is applied to both pure clutter data and pure weather data. To evaluate the performance of clutter detection algorithm, the combined data are formed by adding pure clutter data and pure weather data together. As the pure weather data have a blind range of 5.1 km, to ensure the two data sets seamlessly connected, the first effective range gate of the pure weather data is shifted from 5.1 km to 150 m. For both pure clutter data and pure weather data, the number of pulses in the dwell time is 256. As shown in Section 5.2, there is a difference in clutter detection between mechanical scan and electronic scan with CPPAR. Therefore, these two scan modes are discussed separately as below.

5.3.2 Discriminant Function and Simple Bayesian Classifier

To detect ground clutter with the CPPAR, a proper discriminant function is required that can differentiate weather from clutter. As is known, the wave backscattered from the randomly distributed hydrometeor particles produces a rapidly fluctuating phase due to the random size and location of scatterers, whereas the wave backscattered from ground clutter yields a slow fluctuation in the phase of received signals. Therefore, the phase structure function (PSF) of multiple lags in horizontal and vertical polarizations are introduced as a discriminant function to distinguish clutter from weather. They can be obtained from the average of phase difference between samples with certain lags apart for each resolution volume, as presented in (5-3) and (5-4) respectively,

$$PSF_{\mathrm{h}} = \frac{1}{M-l}\sum_{m=1}^{M-l}|\varphi_{\mathrm{h}}(m+l) - \varphi_{\mathrm{h}}(m)|^2 \tag{5-3}$$

$$PSF_{\mathrm{v}} = \frac{1}{M-l}\sum_{m=1}^{M-l}|\varphi_{\mathrm{v}}(m+l) - \varphi_{\mathrm{v}}(m)|^2 \tag{5-4}$$

where φ_{h} and φ_{v} are the phase of complex voltage sample for each resolution volume in horizontal and vertical polarization, respectively; M is the number of samples (pulses) in the dwell time, l is the number of lags. In addition, the cross-correlation coefficient between two consecutive scans, which can be easily obtained owing to the fast data update of electronic scan with the CPPAR, is also utilized and defined as [73]

$$\rho_{12\mathrm{h}} = \frac{\left|\frac{1}{M}\sum_{m=1}^{M} V_{\mathrm{h1}}^{*}(m)V_{\mathrm{h2}}(m)\right|}{\sqrt{\left|\frac{1}{M}\sum_{m=1}^{M} V_{\mathrm{h1}}^{*}(m)V_{\mathrm{h1}}(m)\right|\left|\frac{1}{M}\sum_{m=1}^{M} V_{\mathrm{h2}}^{*}(m)V_{\mathrm{h2}}(m)\right|}} \tag{5-5}$$

$$\rho_{12\mathrm{v}} = \frac{\left|\frac{1}{M}\sum_{m=1}^{M} V_{\mathrm{v1}}^{*}(m)V_{\mathrm{v2}}(m)\right|}{\sqrt{\left|\frac{1}{M}\sum_{m=1}^{M} V_{\mathrm{v1}}^{*}(m)V_{\mathrm{v1}}(m)\right|\left|\frac{1}{M}\sum_{m=1}^{M} V_{\mathrm{v2}}^{*}(m)V_{\mathrm{v2}}(m)\right|}} \tag{5-6}$$

where V_{h1} and V_{h2} represent complex voltage sample in horizontal polarization for the first and second scan, respectively; V_{v1} and V_{v2} represent complex voltage sample in vertical polarization for the first and second scan, respectively; M is the number of samples (pulses) in the dwell time. As $\rho_{12\mathrm{h}}$ and $\rho_{12\mathrm{v}}$ have almost the same probability density function (PDF), ρ_{12} is utilized as the average of them. Besides, polarimetric variables Z_{DR} and ρ_{hv} are also employed as discriminants.

In this work, a simple Bayesian classifier (SBC) is used to discriminate ground clutter from weather signals [70-71]. The SBC is based on applying Bayes' theorem with strong independence assumptions and is found to work quite well in practice. Using the SBC, radar returns are divided into two categories: one is ground clutter (c), the other is weather signal (w). X represents the 5-D attribute vector, $X = (PSF_{\mathrm{h}}, PSF_{\mathrm{v}}, Z_{\mathrm{DR}}, \rho_{12}, \rho_{\mathrm{hv}})$. For the current resolution volume, $X = X^{O}$(superscript 'O'

represents the observed discriminants) and $X^O = (PSF_{\mathrm{h}}^O, PSF_{\mathrm{v}}^O, Z_{\mathrm{DR}}^O, \rho_{12}^O, \rho_{\mathrm{hv}}^O)$. The SBC judges if the $X = X^O$ belongs to c or w. $X = X^O$ belongs to c only if $p(c|X = X^O) > p(w|X = X^O)$, where the function p is the probability density function. According to Bayes's theorem [74],

$$p(i|X = X^O) = p(X = X^O|i)p(i)/p(X = X^O), \text{ where } i = c, w. \tag{5-7}$$

$p(X = X^O) \equiv K$ is the probability the observation X^O occurs and is the same for both classes, where K is constant. As a result, $p(i|X = X^O)$ is proportional to $p(X = X^O|i)p(i)$. As the probability $p(i)$ are not known a priori, both classes are assumed equally likely, that is, $p(c) = p(w) = 1/2$. Then (5-7) becomes

$$p(i|X = X^O) = p(X = X^O|i)/2K \tag{5-8}$$

Therefore, the SBC assigns $X = X^O$ to c only if $p(X = X^O|c) > p(X = X^O|w)$. $p(X = X^O|i)$ is equal to:

$$p(X = X^O|i) = p(PSF_{\mathrm{h}} = PSF_{\mathrm{h}}^O, PSF_{\mathrm{v}} = PSF_{\mathrm{v}}^O, Z_{\mathrm{DR}} = Z_{\mathrm{DR}}^O, \rho_{12} = \rho_{12}^O, \rho_{\mathrm{hv}} = \rho_{\mathrm{hv}}^O|i) \tag{5-9}$$

In the SBC, the simple assumption of class-conditional independence is made [75]. Thus (5-7) can be rewritten as:

$$p(X = X^O|i) = p\left(PSF_{\mathrm{h}} = PSF_{\mathrm{h}}^O, PSF_{\mathrm{v}} = PSF_{\mathrm{v}}^O\middle|i\right) \times p(Z_{\mathrm{DR}} = Z_{\mathrm{DR}}^O|i) \times p(\rho_{12} = \rho_{12}^O, \rho_{\mathrm{hv}} = \rho_{\mathrm{hv}}^O|i) \tag{5-10}$$

In (5-8) the joint probability $p\left(PSF_{\mathrm{h}} = PSF_{\mathrm{h}}^O, PSF_{\mathrm{v}} = PSF_{\mathrm{v}}^O\middle|i\right)$ is used because PSF_{h} and PSF_{v} are highly correlated, especially for weather signals, and the joint probability $p\left(\rho_{12} = \rho_{12}^O, \rho_{\mathrm{hv}} = \rho_{\mathrm{hv}}^O\middle|i\right)$ is used because they have similar physical meaning. By doing so, it is expected that the SBC would have better classification between classes.

The conditional probability density functions of $p\left(PSF_{\mathrm{h}} = PSF_{\mathrm{h}}^{O}, PSF_{\mathrm{v}} = PSF_{\mathrm{v}}^{O} \middle| i\right)$, $p(Z_{\mathrm{DR}} = Z_{\mathrm{DR}}^{O}|i)$, and $p(\rho_{12} = \rho_{12}^{O}, \rho_{\mathrm{hv}} = \rho_{\mathrm{hv}}^{O}|i)$, for $i = c, w$ can be obtained from the controlled data sets (i.e., pure clutter data and pure weather data). Thus, the joint conditional probability density function $p(X = X^{O}|i)$ can be calculated for each class to make decisions as to the presence of ground clutter. It should be noted that $p(X = X^{O}|i)$ is dependent on the radar sites, radar characteristics, scan strategies, and environmental conditions [71].

The SBC can be summarized in the following steps:

(1) Calculate the SNR or CNR for the current resolution volume. If the SNR or CNR is less than 10dB, the current gate is considered as not having a significant weather signal or clutter compared to the noise power, then compute the SNR or CSR for the next range resolution volume. Otherwise, go to step (2).

(2) Calculate the discriminants PSF_{h}, PSF_{v}, Z_{DR}, ρ_{12}, and ρ_{hv}. Look up the conditional probability density functions $p(PSF_{\mathrm{h}}, PSF_{\mathrm{v}}|i)$, $p(Z_{\mathrm{DR}}|i)$, and $p(\rho_{12}, \rho_{\mathrm{hv}}|i)$ for $i = c, w$. These conditional probability density functions are obtained from the controlled data sets.

(3) If $p(X = X^{O}|c) > p(X = X^{O}|w)$, the current gate is clutter contaminated. Otherwise, the current gate is weather and return to step (1) for the next gate.

5.3.3 Clutter Detection Using Electronic Scan Data

5.3.3.1 Convective precipitation

The pure clutter data collected with the CPPAR in the electronic scan on 9 May 2020 are shown in Figure 5-4. The pure weather data from convective precipitation

collected with the CPPAR in the electronic scan on 15 May 2020 are shown in Figure 5-5. The combined data are shown in Figure 5-6. As shown in Figure 5-6, in the clutter-contaminated area of the combined data, the reflectivity increases, the radial velocity is biased toward zero, and all the polarimetric estimates are biased compared to those in Figure 5-5. The scatter plots of PSF_{h} and PSF_{v} at the lag of 1 to 4 for pure clutter data and pure weather data are shown in Figure 5-7.

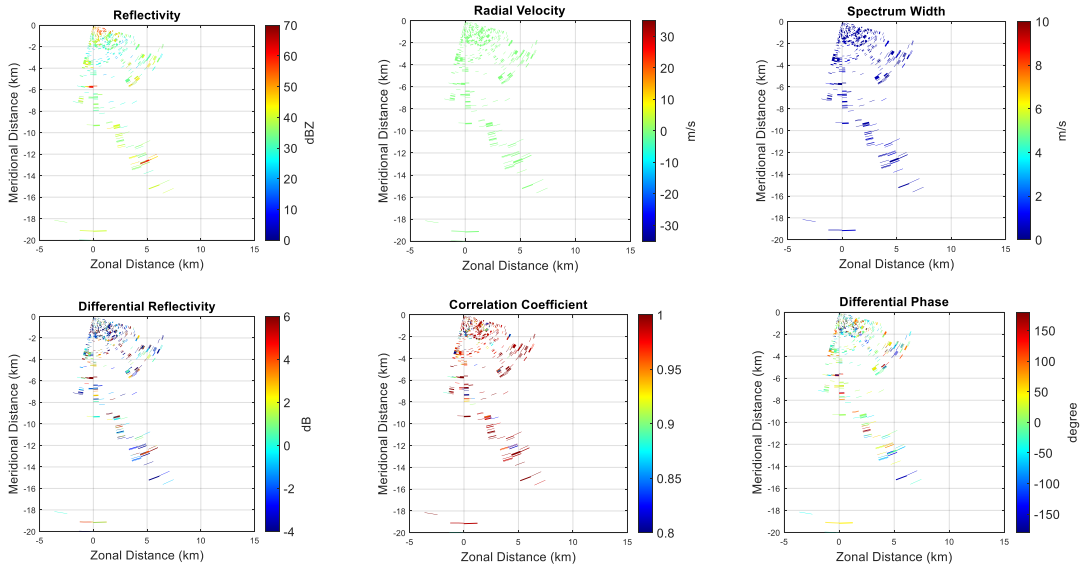

Figure 5-4 Clutter measurements with electronic scan at 15:43:08 UTC on 9 May 2020.

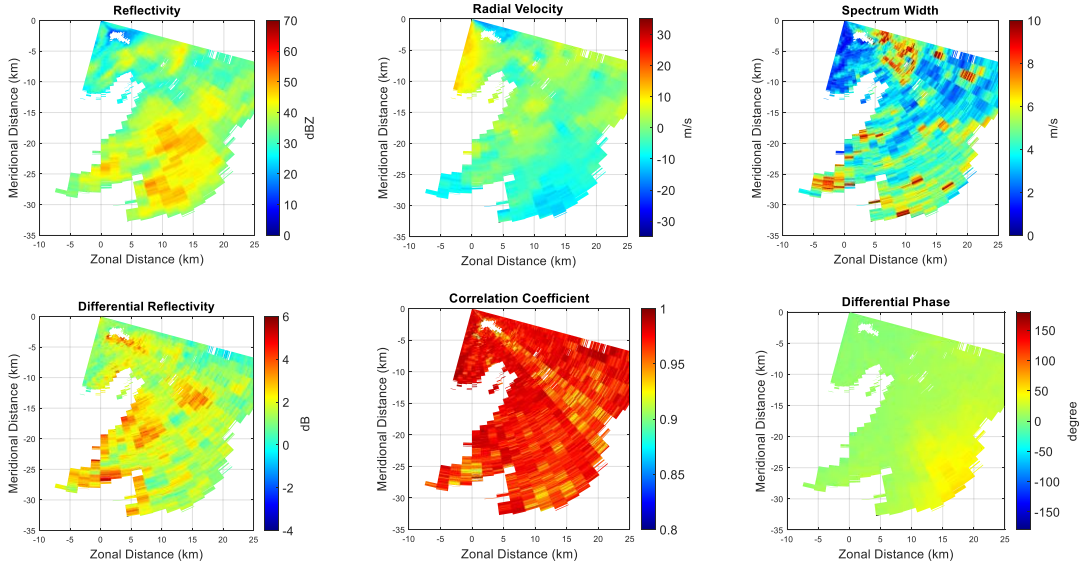

Figure 5-5 Weather measurements with electronic scan at 18:55:22 UTC on 15 May 2020.

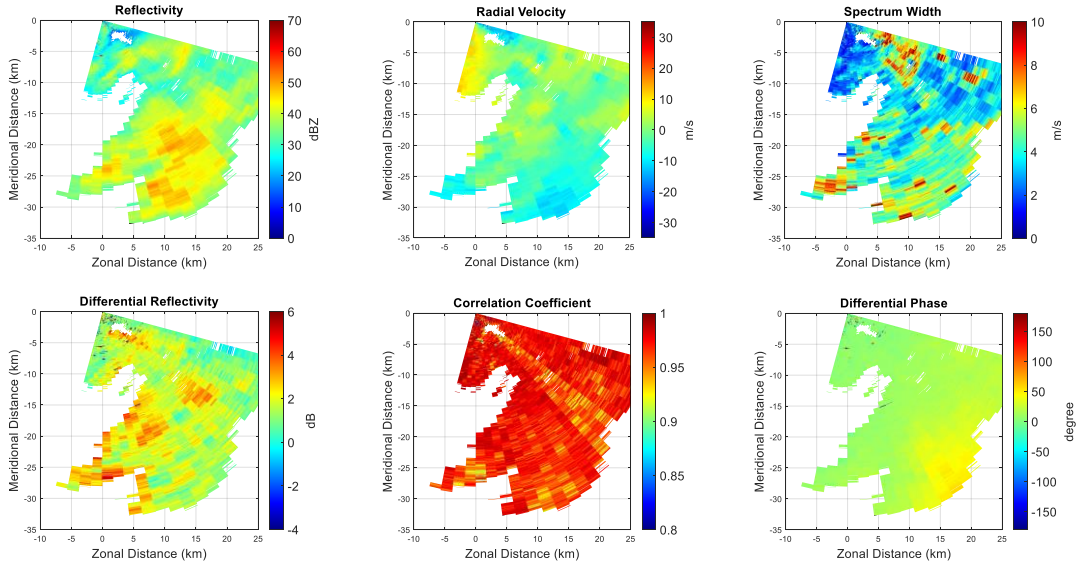

Figure 5-6 Combined clutter and weather measurements with electronic scan.

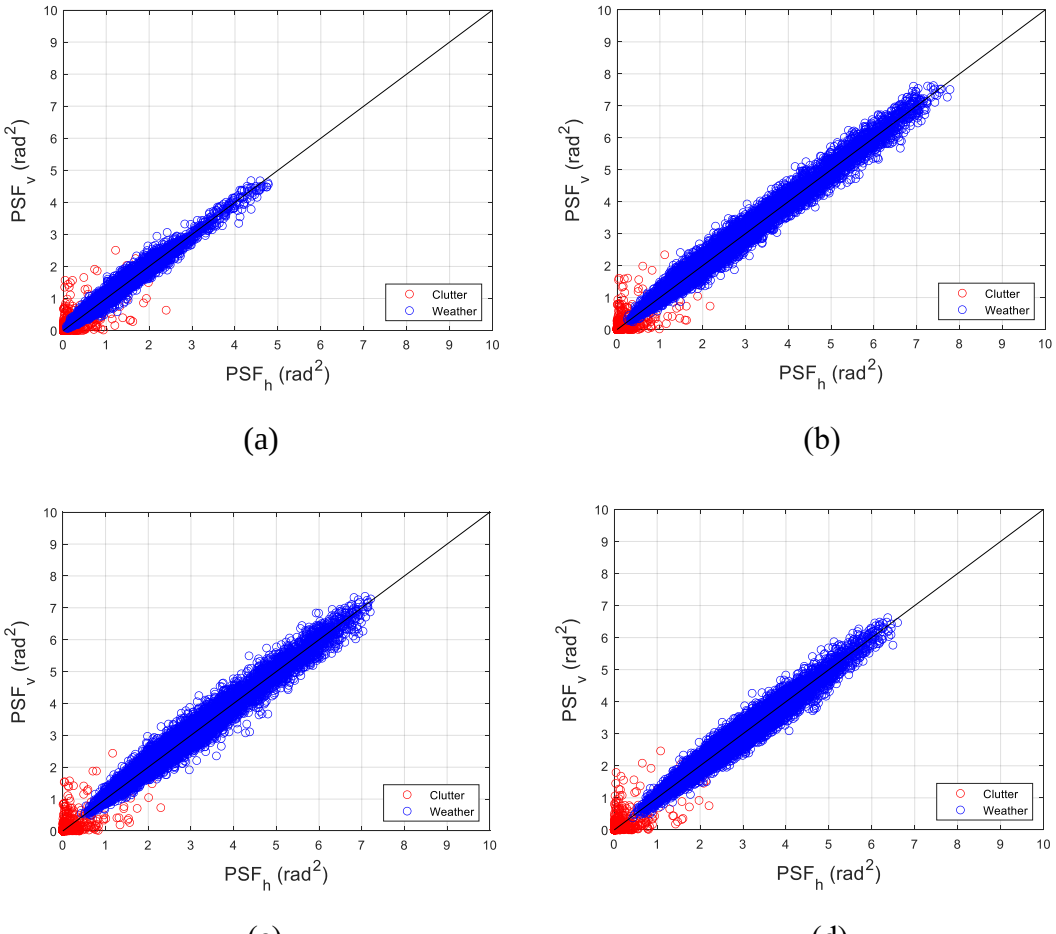

Figure 5-7 Scatter plots of PSF_h and PSF_v at multiple lags for the measurements in Figure 5-4 and Figure 5-5. (a) Lag=1. (b) Lag=2. (c) Lag=3. (d) Lag=4.

As shown in Figure 5-7, there is significant overlap between weather and clutter in case of PSF with lag=1. As a comparison, there is less overlap between weather and clutter in case of PSF with multiple lags.

The conditional probability density functions of $p(PSF_{\mathrm{h}}, PSF_{\mathrm{v}}|i)$ at various lags for clutter and weather are shown in Figure 5-8. The conditional probability density functions of $p(Z_{\mathrm{DR}}|i)$ and $p(\rho_{12}, \rho_{\mathrm{hv}}|i)$ for clutter and weather are shown in Figure 5-9.

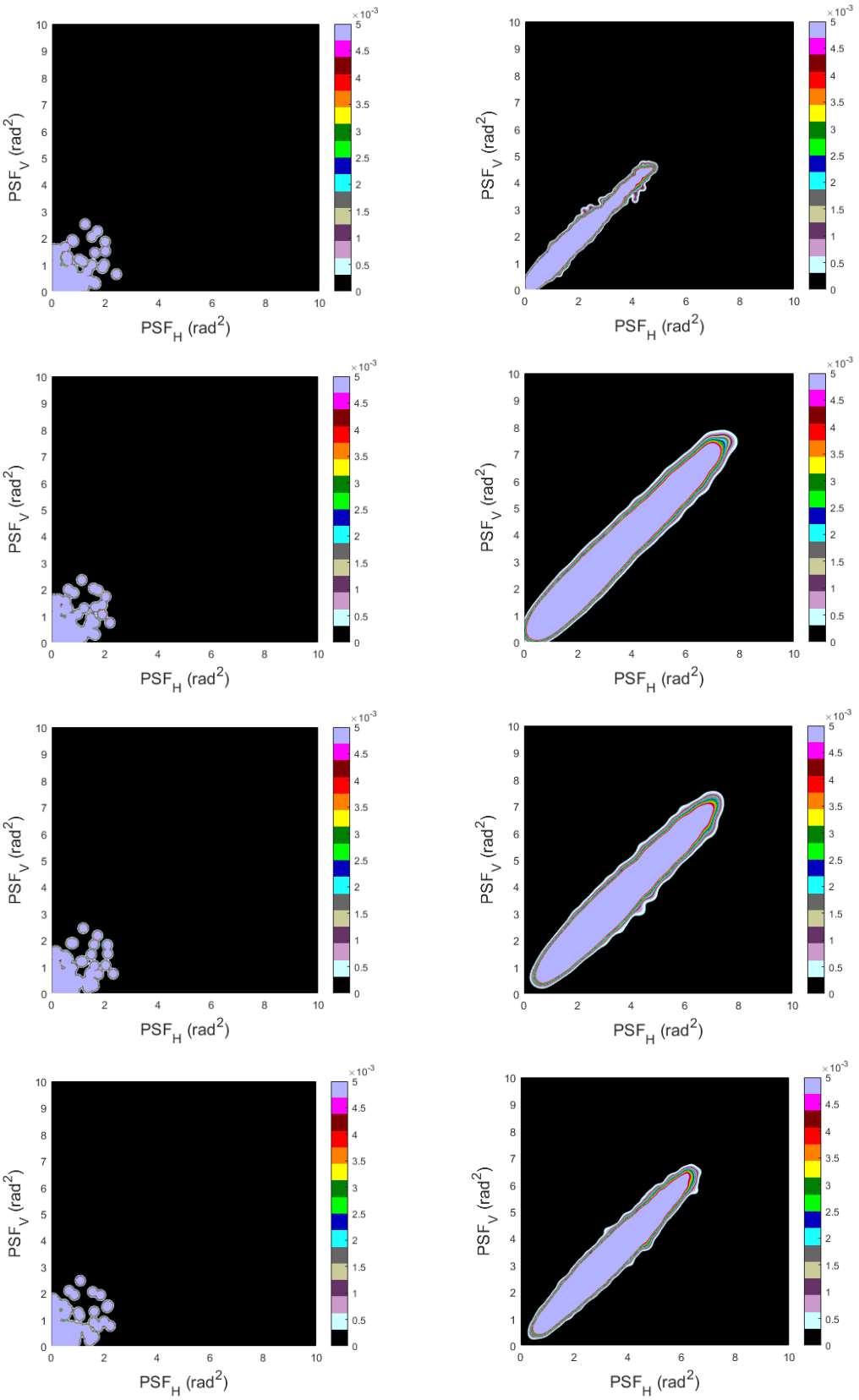

Figure 5-8 The joint conditional probability density functions of PSF_h and PSF_v given clutter (left column) and weather (right column) with electronic scan. Figures from top to bottom rows refer to the lag of 1, 2, 3, and 4 respectively.

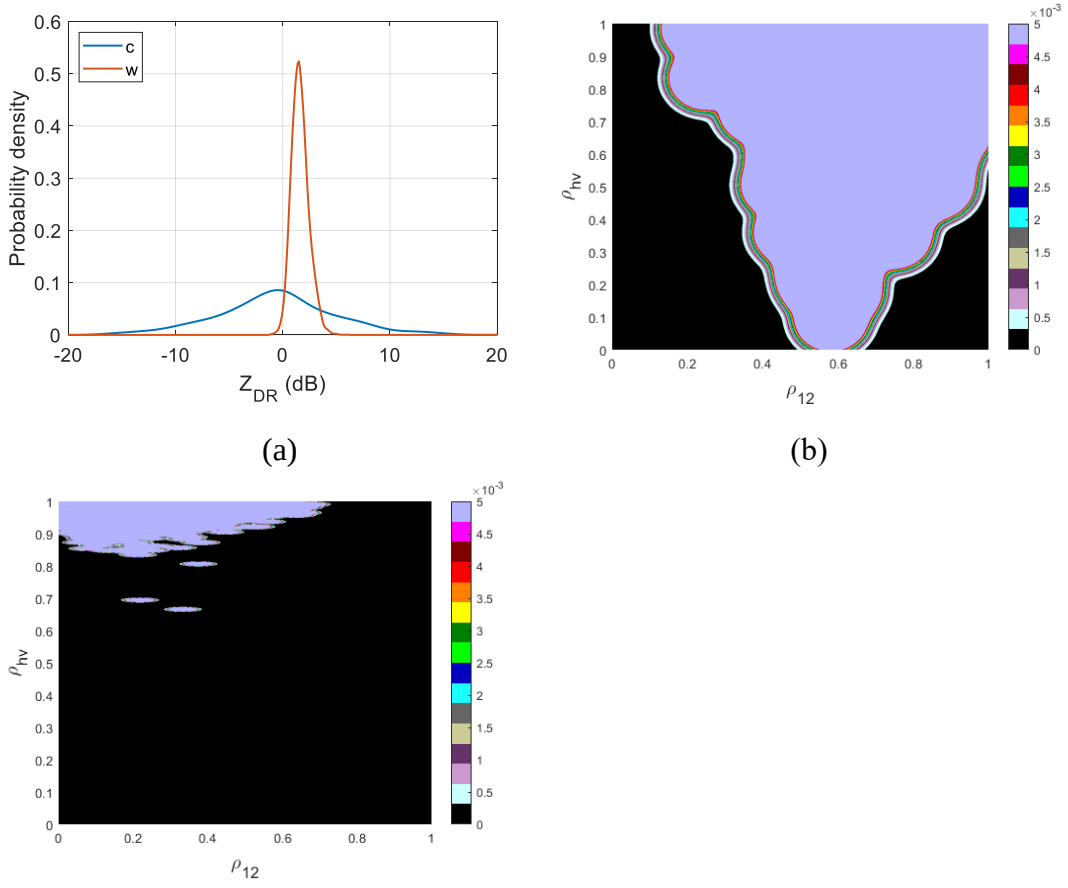

Figure 5-9 The conditional probability density functions with electronic scan. (a) The conditional probability density function of Z_{DR} given clutter and weather. (b) The joint conditional probability density function of ρ_{12} and ρ_{hv} given clutter. (c) The joint conditional probability density function of ρ_{12} and ρ_{hv} given weather.

Figure 5-8 shows that as the lag increases, the overlap between $p(PSF_{\mathrm{h}}, PSF_{\mathrm{v}}|c)$ and $p(PSF_{\mathrm{h}}, PSF_{\mathrm{v}}|w)$ reduces, which indicates that it is more likely to distinguish clutter from weather. On the other hand, the overlapped region is likely to be caused by narrow-band zero-velocity weather signals that have very similar properties as ground clutter. Figure 5-9 shows that both $p(Z_{\mathrm{DR}}|c)$ and $p(\rho_{12}, \rho_{\mathrm{hv}}|c)$ has a much larger spread than those for weather signals.

To evaluate the clutter detection performance, the ground truth clutter map should be obtained, which is done by finding those gates where clutter significantly

biases weather radar estimates. In this study, to be consistent with NEXRAD specifications for data quality, a resolution volume is considered to have weather signals contaminated by clutter only if ground clutter biases the weather signal's reflectivity estimates by more than 1 dB, or its radial velocity estimates by more than 1 m/s, or its spectrum width estimates by more than 1 m/s. Otherwise, even if ground clutter from a range bin is mixed with weather signal, the combined signal is still considered as weather signal because the clutter's effect on radar estimates can be neglected [70]. The above metrics apply to the case of 64 pulses per dwell. As mentioned above, there are 256 pulses per dwell for the CPPAR during data collection. As the standard deviation of radar estimates is inversely proportional to the square root of the number of samples (pulses), for 256 pulses per dwell, a resolution volume is considered to have weather signal contaminated by clutter only if ground clutter biases the weather signal's reflectivity estimates by more than 0.5 dB, or its radial velocity estimates by more than 0.5 m/s, or its spectrum width estimates by more than 0.5 m/s.

For quantitative assessment of the clutter detection performance, the probability of detection (POD), probability of false alarm rate (PFA), and critical success index (CSI) are computed, which are defined as [75]

$$POD = True\ Positives/(True\ Positives + False\ Negatives) \quad (5\text{-}11)$$

$$PFA = False\ Positives/(False\ Positives + True\ Negatives) \quad (5\text{-}12)$$

$$CSI = True\ Positives/(True\ Positives + False\ Negatives + False\ Positives) \quad (5\text{-}13)$$

where “Positive” means the detector classifies the location as clutter contaminated, and “Negative” means the detector classifies the location as weather; “True Positive (TP)” implies that the detector classifies the location as clutter-contaminated, and the truth is clutter-contaminated; “False Negative (FN)” denotes that the detector classifies the location as weather, whereas the truth is clutter-contaminated; “False Positive (FP)” denotes that the detector claims clutter, whereas the truth is weather; “True Negative (TN)” denotes that the detector claims weather, and the truth is weather.

The SBC clutter detection maps of the controlled data set for PSF_{h} and PSF_{v} at various lags, as well as the ground truth clutter map, are shown in Figure 5-10. The POD as a function of CSR for each lag are plotted in Figure 5-11. For example, in order to obtain the POD at CSR = 0 dB, all the gates contaminated by ground clutter having CSR larger than −0.5 dB but smaller than 0.5 dB are counted and summed to give the true number of gates having CSR = 0 dB, which is denoted as Nt. Next, the number of clutter contaminated gates (for CSR = 0 dB) detected by the algorithm is summed as Nd. Then the ratios of Nd/Nt is the POD for CSR = 0 dB [71]. The number of TP, FN, FP, TN, POD, PFA, and CSI for each lag are listed in Table 5-1. For an ideal clutter detector, we have POD=100%, PFA=0, FN=0, FP=0, and CSI=1.

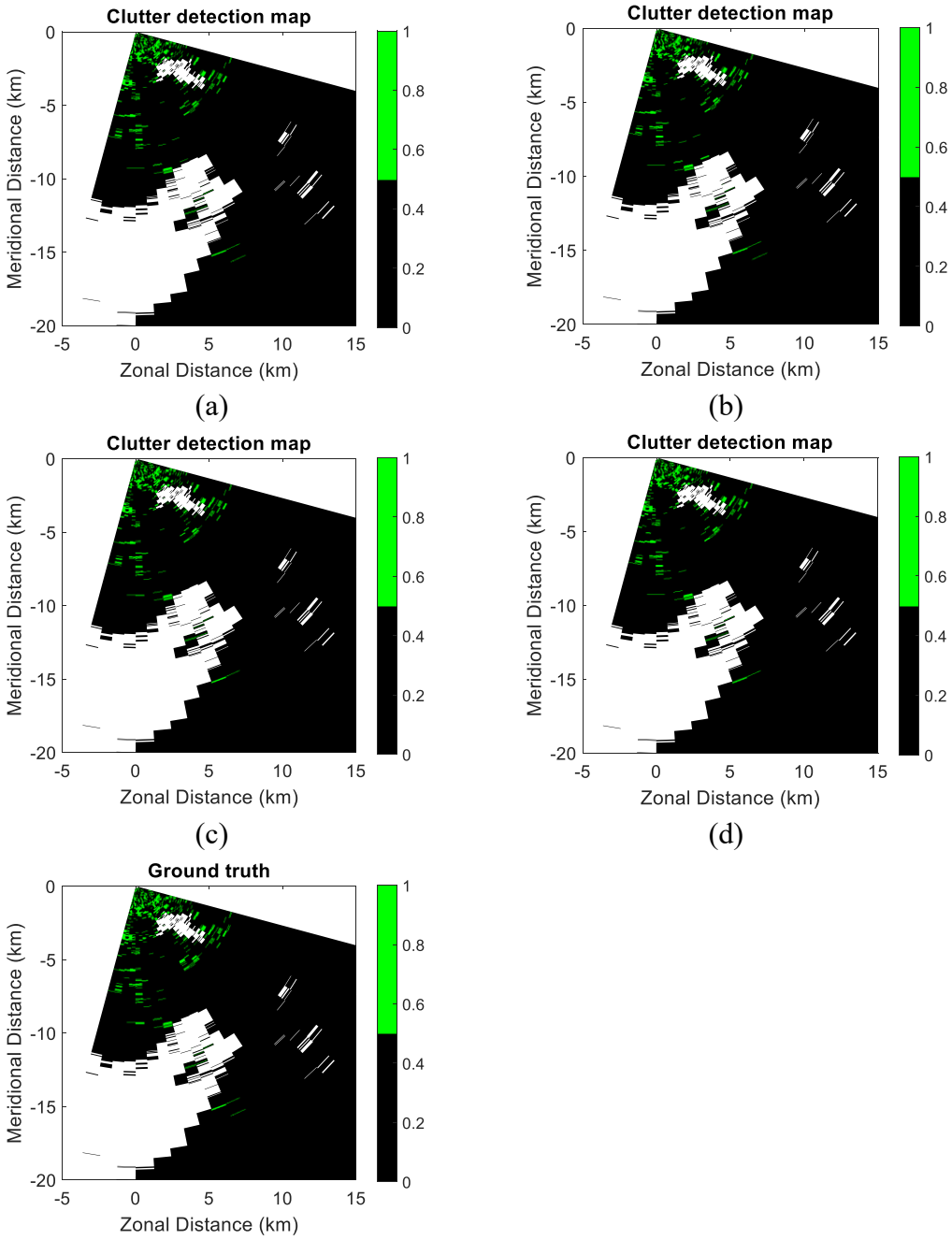

Figure 5-10 Detected clutter maps obtained using SBC with electronic scan. (a) Lag=1. (b) Lag=2. (c) Lag=3. (d) Lag=4. (e) Ground truth clutter map.

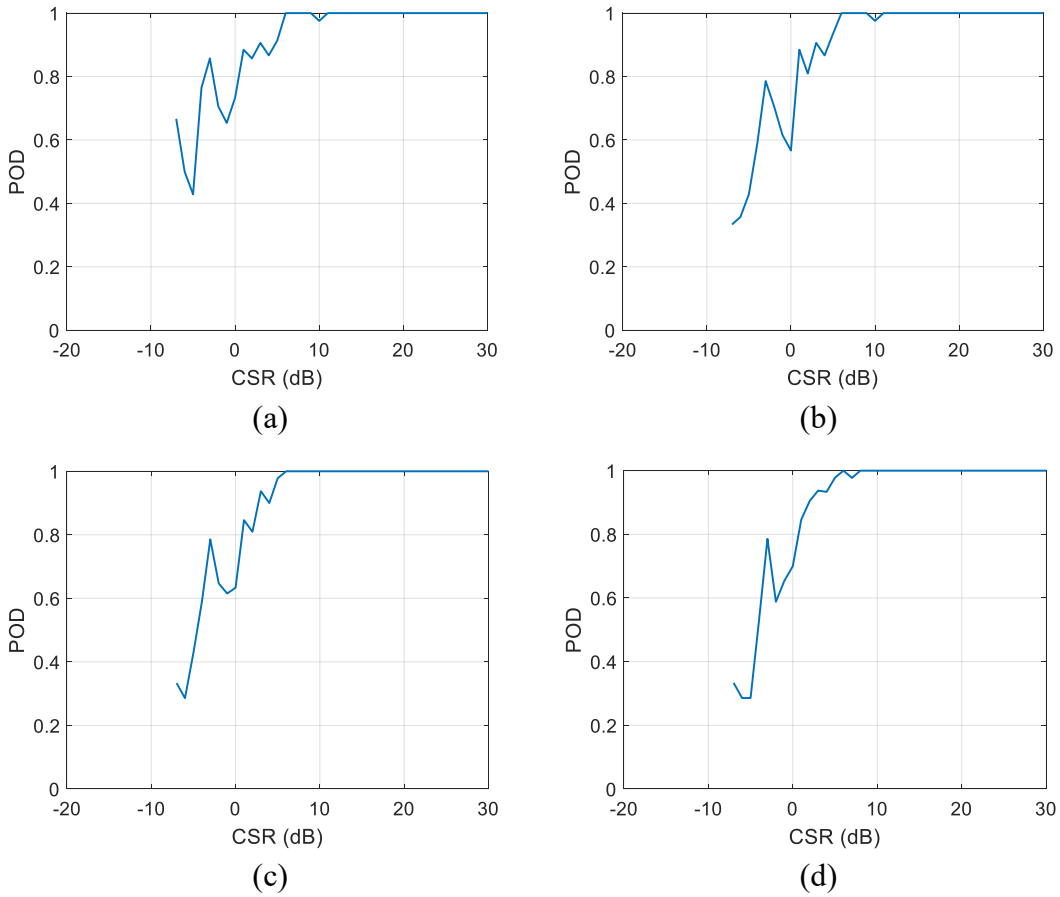

Figure 5-11 POD as a function of CSR with electronic scan. (a) Lag=1. (b) Lag=2. (c) Lag=3. (d) Lag=4.

Table 5-1 The number of TP, FN, FP, TN, POD, PFA, and CSI at various lags with electronic scan in convective precipitation

	TP	FN	FP	TN	POD	PFA	CSI
Lag 1	912	63	17	21622	93.54%	0.08%	0.92
Lag 2	897	78	10	21629	92.00%	0.05%	0.91
Lag 3	902	73	1	21638	92.51%	0.005%	0.92
Lag 4	904	71	5	21634	92.72%	0.02%	0.92

5.3.3.2 Stratiform precipitation

The pure clutter data collected with the CPPAR in the electronic scan on 30 May 2020 are shown in Figure 5-12. The pure weather data from stratiform precipitation collected with the CPPAR in the electronic scan on 25 May 2020 are shown in Figure 5-13. The combined data are shown in Figure 5-14. The scatter plots

of PSF_{h} and PSF_{v} at the lag of 1 to 4 for pure clutter data and pure weather data are shown in Figure 5-15.

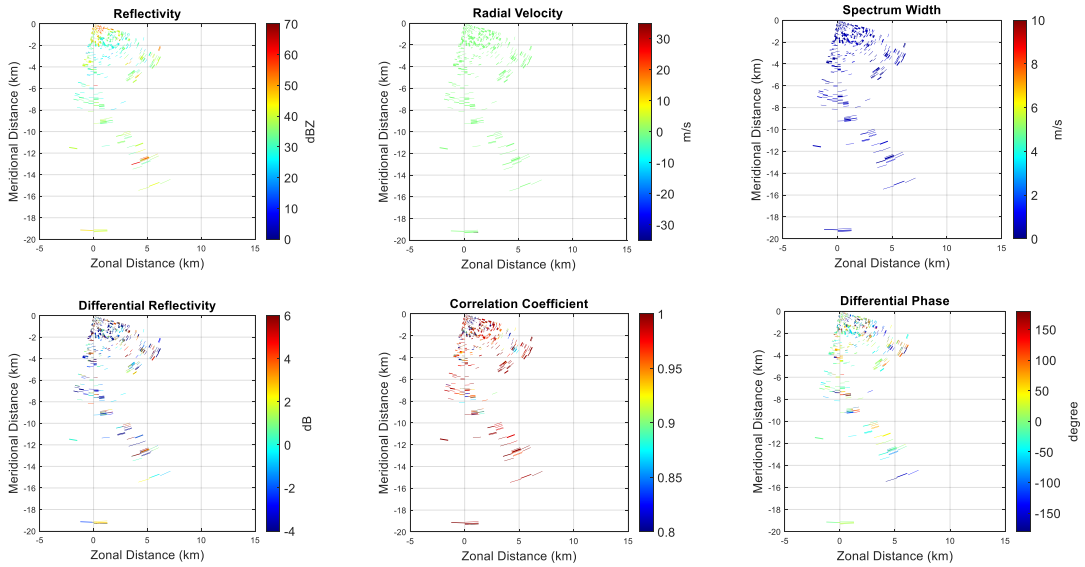

Figure 5-12 Clutter measurements with electronic scan at 22:04:19 UTC on 30 May 2020.

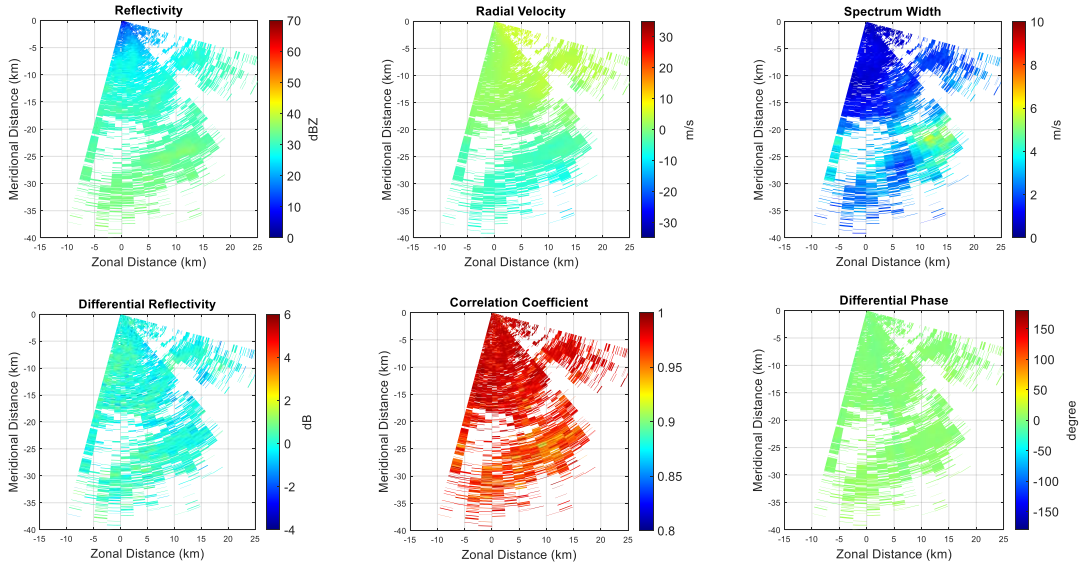

Figure 5-13 Weather measurements with electronic scan at 20:33:38 UTC on 25 May 2020.

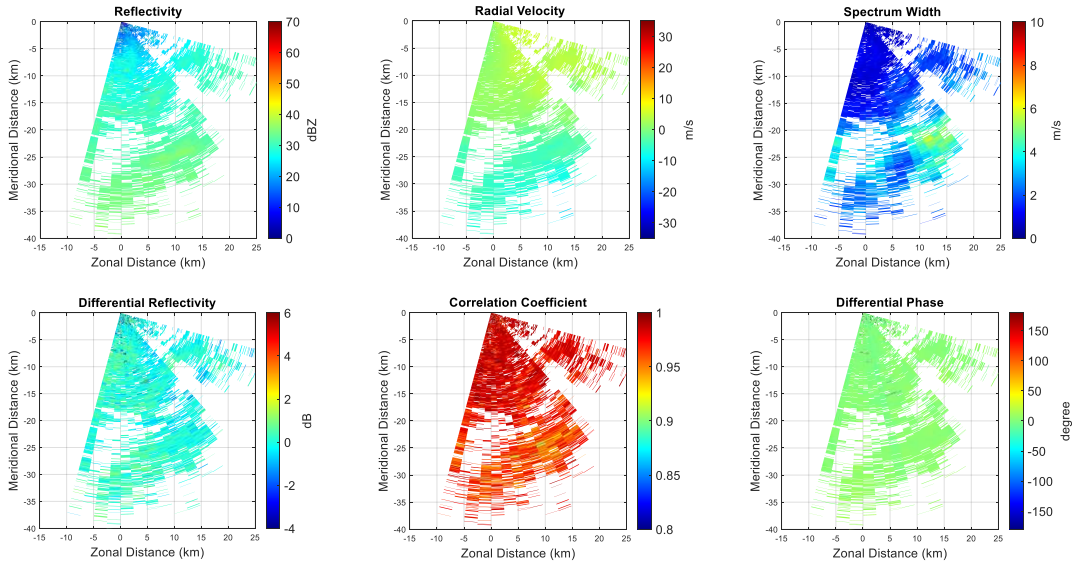

Figure 5-14 Combined clutter and weather measurements with electronic scan.

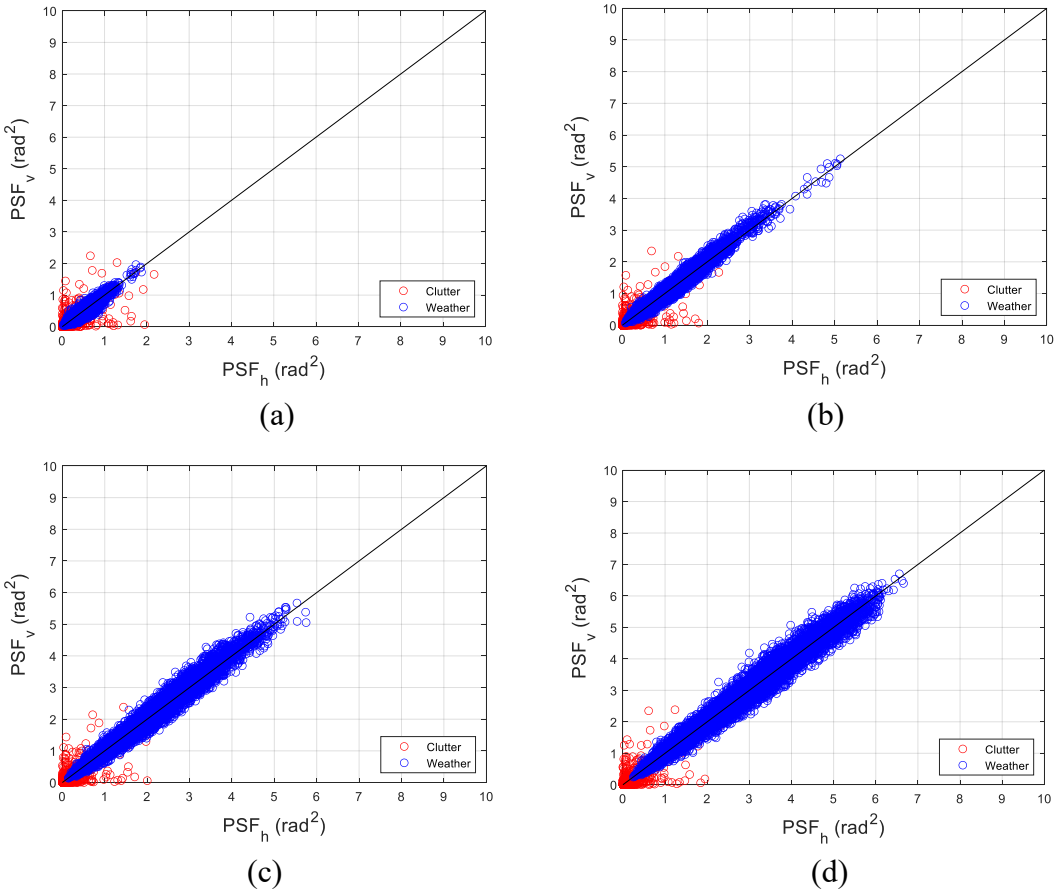

Figure 5-15 Scatter plots of PSF_h and PSF_v at multiple lags for the measurements in Figure 5-12 and Figure 5-13. (a) Lag=1. (b) Lag=2. (c) Lag=3. (d) Lag=4.

As shown in Figure 5-15, there is more overlap between weather and clutter in

case of PSF with lag=1. As a comparison, there is less overlap between weather and clutter in case of PSF with multiple lags.

The conditional probability density functions of $p(PSF_{\mathrm{h}}, PSF_{\mathrm{v}}|i)$ at various lags for clutter and weather are shown in Figure 5-16. The conditional probability density functions of $p(Z_{\mathrm{DR}}|i)$ and $p(\rho_{12}, \rho_{\mathrm{hv}}|i)$ for clutter and weather are shown in Figure 5-17.

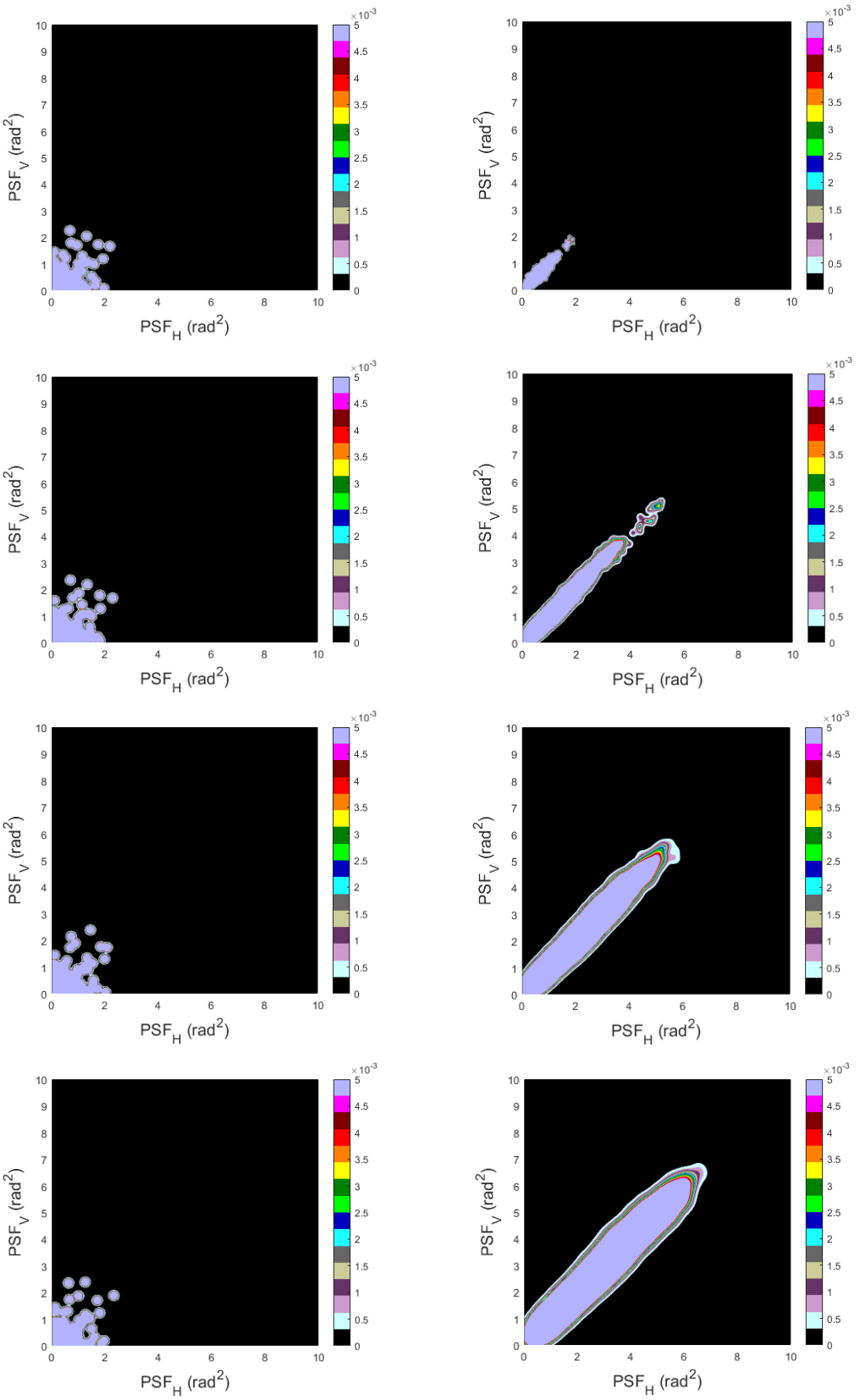

Figure 5-16 The joint conditional probability density functions of PSF_h and PSF_v given clutter (left column) and weather (right column) with electronic scan. Figures from top to bottom rows refer to the lag of 1, 2, 3, and 4 respectively.

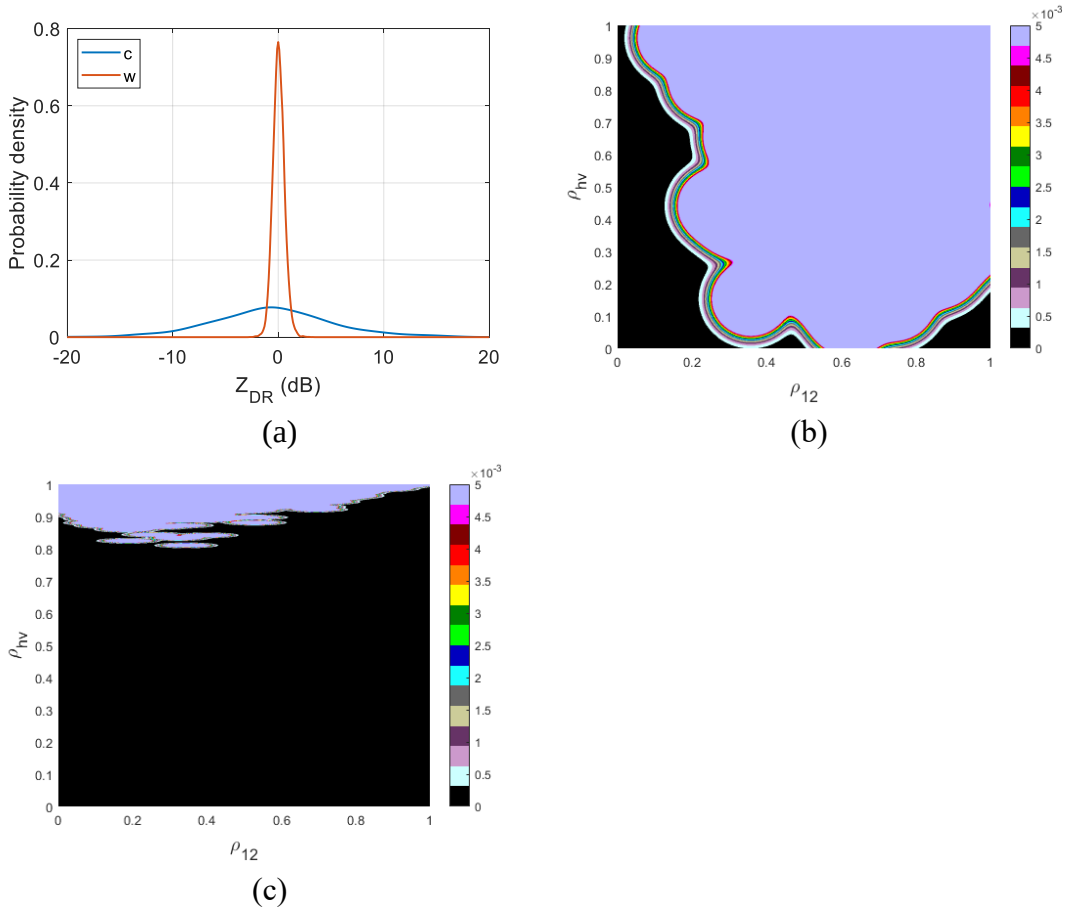

Figure 5-17 The conditional probability density functions with electronic scan. (a) The conditional probability density function of Z_{DR} given clutter and weather. (b) The joint conditional probability density function of ρ_{12} and ρ_{hv} given clutter. (c) The joint conditional probability density function of ρ_{12} and ρ_{hv} given weather.

Figure 5-16 shows that as lag increases, the overlap between $p(PSF_{\mathrm{h}}, PSF_{\mathrm{v}}|c)$ and $p(PSF_{\mathrm{h}}, PSF_{\mathrm{v}}|w)$ reduces, which indicates that it is more likely to distinguish clutter from weather. On the other hand, the overlapped region is likely to be caused by narrow-band zero-velocity weather signals that have very similar properties as ground clutter. Figure 5-17 shows that both $p(Z_{\mathrm{DR}}|c)$ and $p(\rho_{12}, \rho_{\mathrm{hv}}|c)$ has a much larger spread than those for weather signals.

The SBC clutter detection maps of the controlled data set for PSF_{h} and PSF_{v} at various lags as well as the ground truth clutter map are shown in Figure 5-18. The number of TP, FN, FP, TN, POD, PFA, and CSI for each lag are listed in Table 5-2.

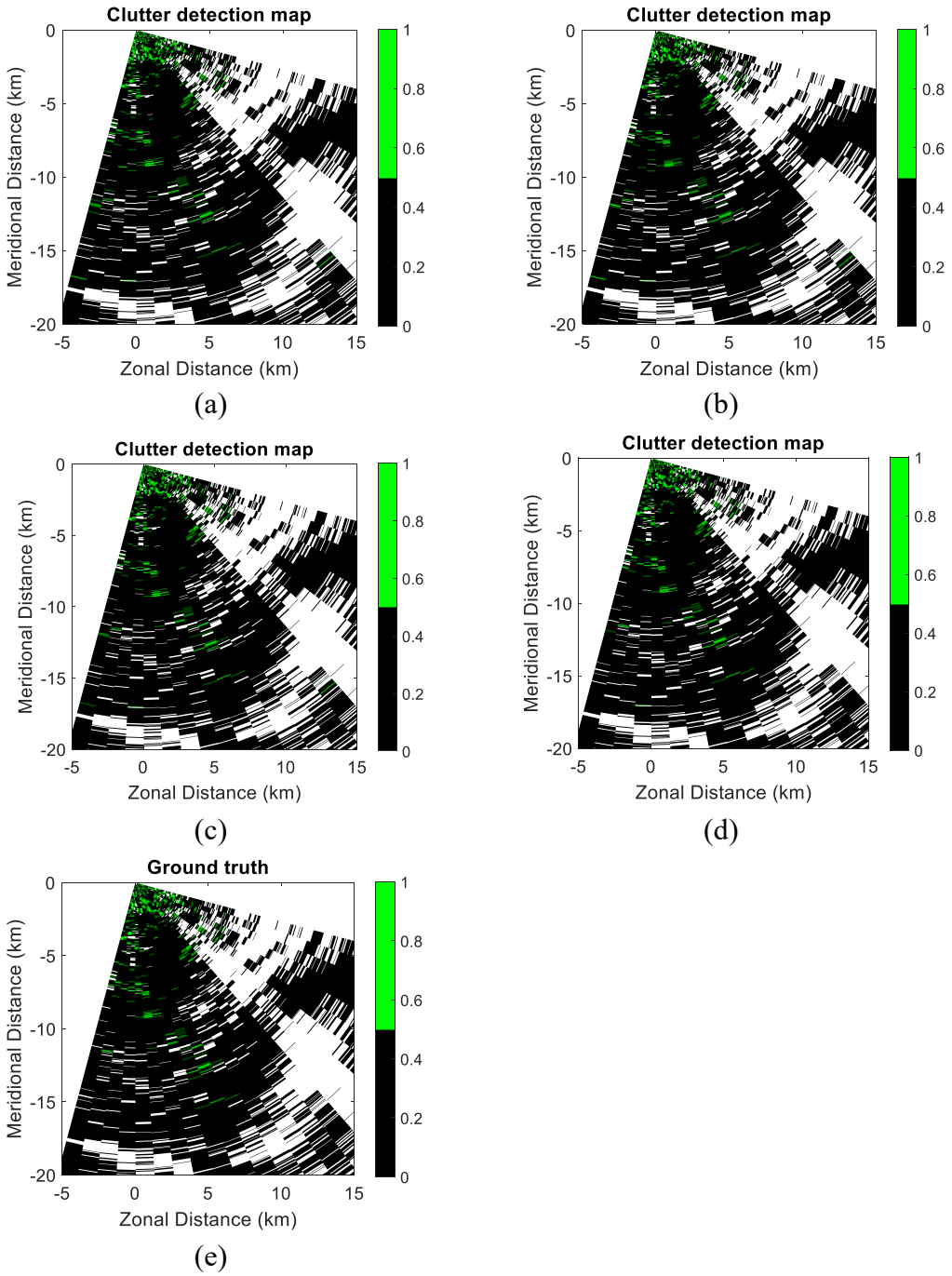

Figure 5-18 Detected clutter maps obtained using SBC with electronic scan. (a) Lag=1. (b) Lag=2. (c) Lag=3. (d) Lag=4. (e) Ground truth clutter map.

Table 5-2 The number of TP, FN, FP, TN, POD, PFA, and CSI at various lags with electronic scan in stratiform precipitation

	TP	FN	FP	TN	POD	PFA	CSI
Lag 1	844	31	126	16052	96.46%	0.78%	0.84
Lag 2	842	33	84	16094	96.23%	0.52%	0.88
Lag 3	846	29	63	16115	96.69%	0.39%	0.90
Lag 4	847	28	43	16135	96.80%	0.27%	0.92

Table 5-2 shows that clutter detection performance in stratiform precipitation becomes better as the number of lags increase, because more lags will have larger phase change, which is helpful for PSF_{h} and PSF_{v} to discriminate between weather and clutter. It validates that multi-lag PSF_{h} and PSF_{v} are more effective in clutter detection for stratiform precipitation.

5.3.4 Clutter Detection Using Mechanical Scan Data

5.3.4.1 Convective precipitation

The pure clutter data collected with the CPPAR in the mechanical scan on 17 May 2020 are shown in Figure 5-19. The pure weather data from convective precipitation collected with the CPPAR in the mechanical scan on 15 May 2020 are shown in Figure 5-20. The combined data are shown in Figure 5-21. The scatter plots of PSF_{h} and PSF_{v} at the lag of 1 to 4 for pure clutter data and pure weather data are shown in Figure 5-22.

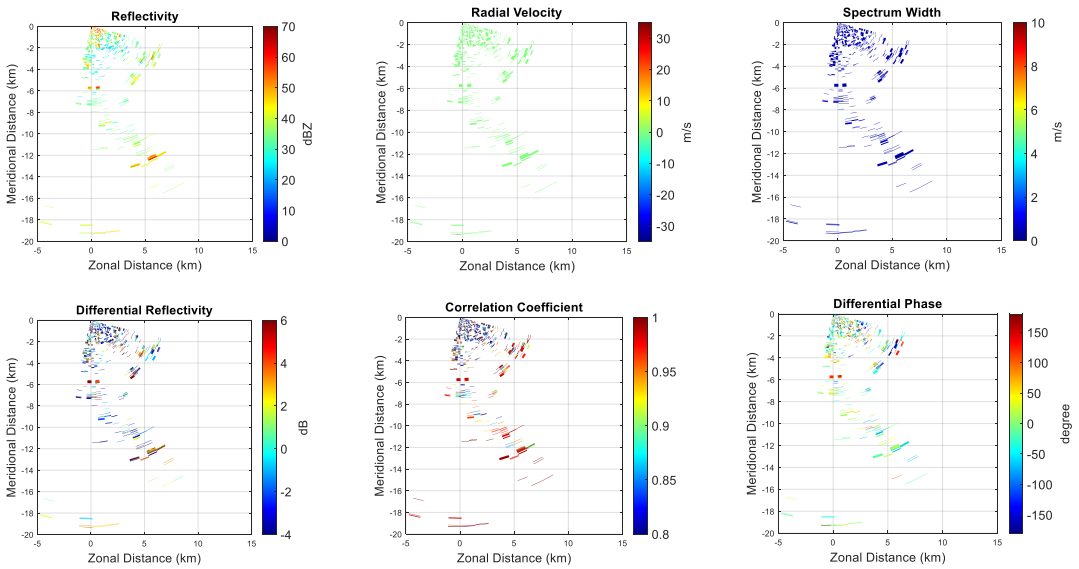

Figure 5-19 Clutter measurements with mechanical scan at 23:00:20 UTC on 17 May 2020.

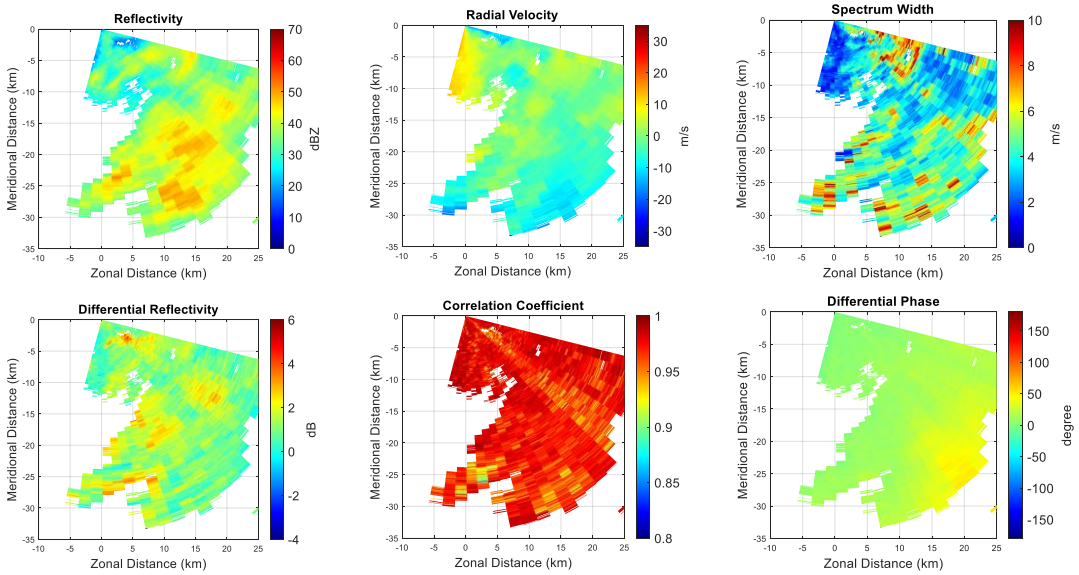

Figure 5-20 Weather measurements with mechanical scan at 18:56:43 UTC on 15 May 2020.

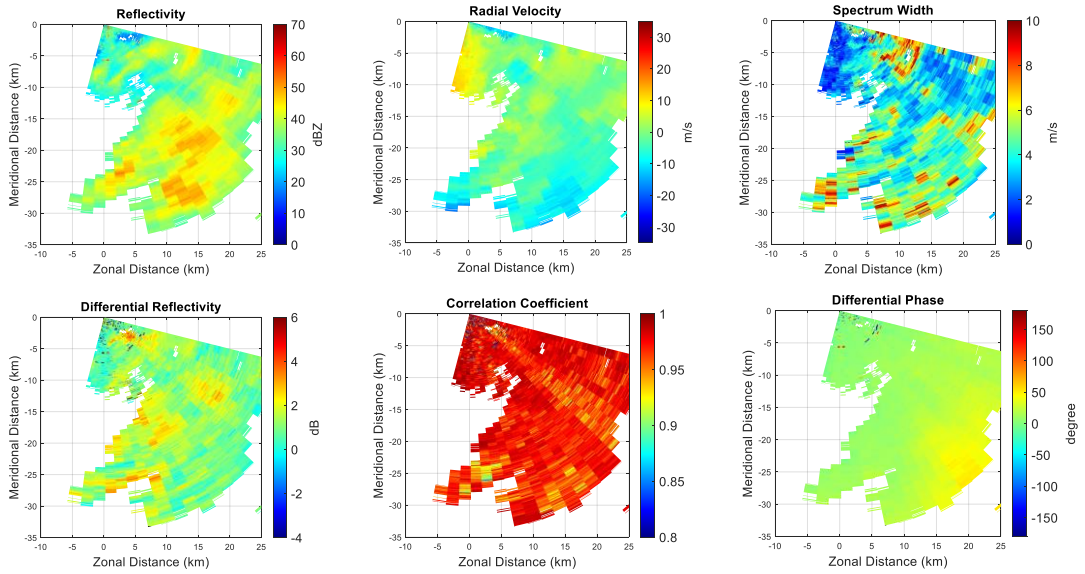

Figure 5-21 Combined clutter and weather measurements with mechanical scan.

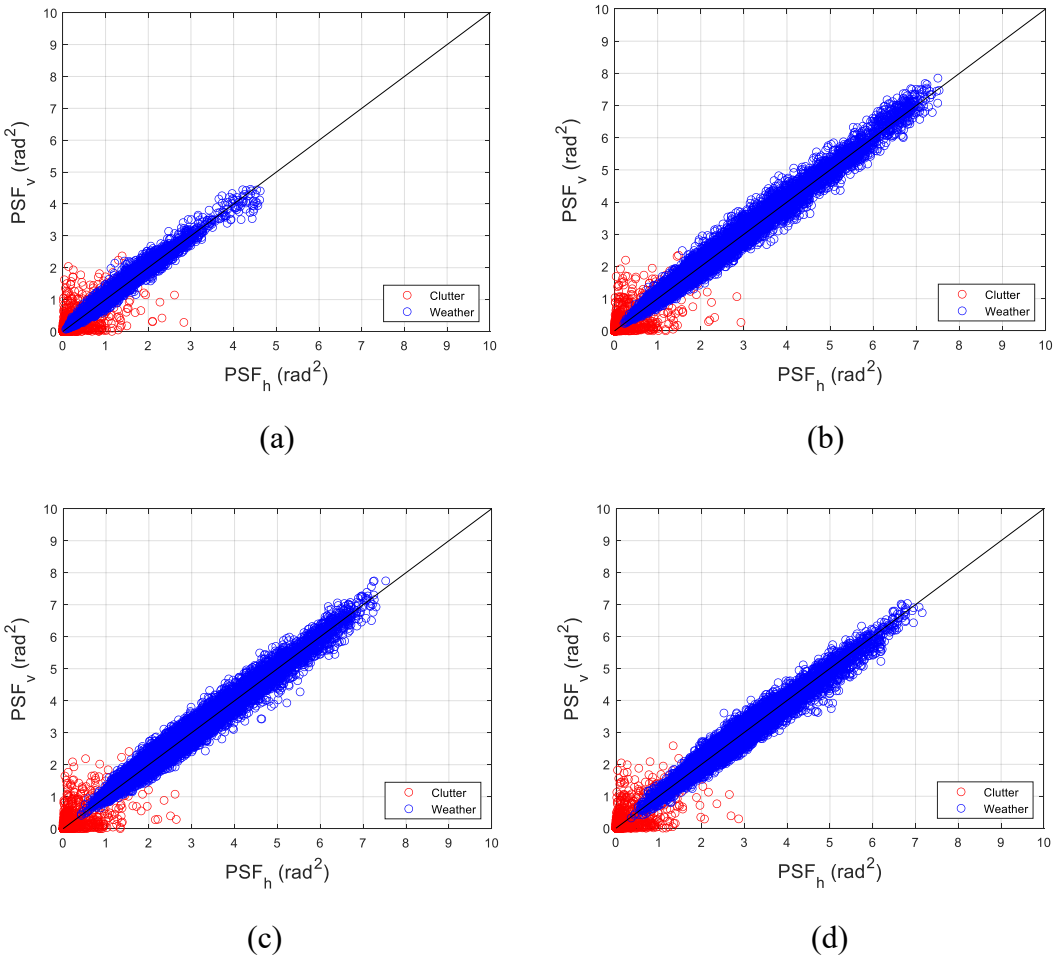

Figure 5-22 Scatter plots of PSF_h and PSF_v at multiple lags for the measurements in Figure 5-19 and Figure 5-20. (a) Lag=1. (b) Lag=2. (c) Lag=3. (d) Lag=4.

As shown in Figure 5-22, there is more overlap between weather and clutter in

case of PSF with lag=1. As a comparison, there is less overlap between weather and clutter in case of PSF with multiple lags.

The conditional probability density functions of $p(PSF_{\mathrm{h}}, PSF_{\mathrm{v}}|i)$ at various lags for clutter and weather are shown in Figure 5-23. The conditional probability density functions of $p(Z_{\mathrm{DR}}|i)$ and $p(\rho_{12}, \rho_{\mathrm{hv}}|i)$ for clutter and weather are shown in Figure 5-24.

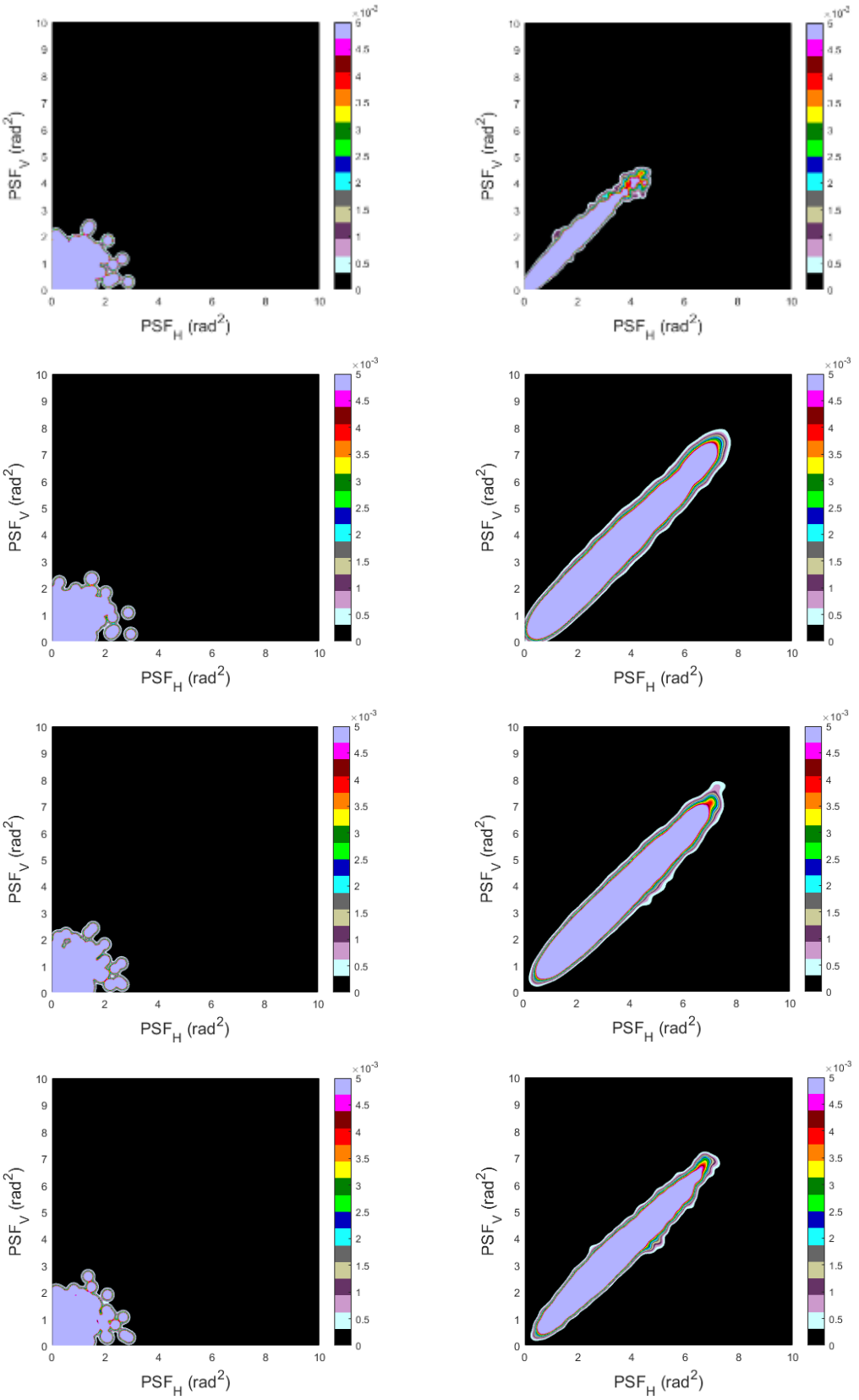

Figure 5-23 The joint conditional probability density functions of PSF_h and PSF_v given clutter (left column) and weather (right column) with mechanical scan. Figures from top to bottom rows refer to the lag of 1, 2, 3, and 4 respectively.

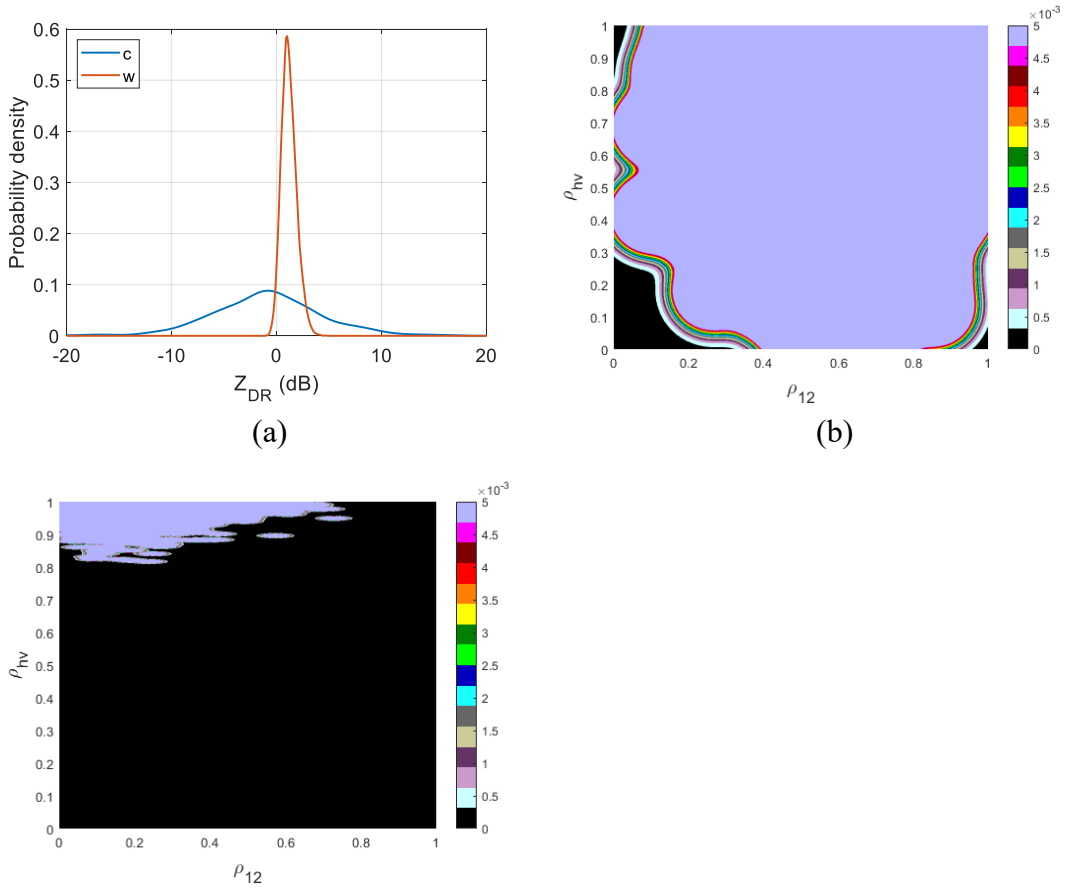

Figure 5-24 The conditional probability density functions with mechanical scan. (a) The conditional probability density function of Z_{DR} given clutter and weather. (b) The joint conditional probability density function of ρ_{12} and ρ_{hv} given clutter. (c) The joint conditional probability density function of ρ_{12} and ρ_{hv} given weather.

Figure 5-23 shows that as lag increases, the overlap between $p(PSF_{\mathrm{h}}, PSF_{\mathrm{v}}|c)$ and $p(PSF_{\mathrm{h}}, PSF_{\mathrm{v}}|w)$ reduces, which indicates that it is more likely to distinguish clutter from weather. On the other hand, the overlapped region is likely to be caused by narrow-band zero-velocity weather signals that have very similar properties as ground clutter. Figure 5-24 shows that both $p(Z_{\mathrm{DR}}|c)$ and $p(\rho_{12}, \rho_{\mathrm{hv}}|c)$ has a much larger spread than those for weather signals.

The SBC clutter detection maps of the controlled data set for PSF_{h} and PSF_{v} at various lags as well as the ground truth clutter map are shown in Figure 5-25. The

POD as a function of CSR for each lag are plotted in Figure 5-26. The number of TP, FN, FP, TN, POD, PFA, and CSI for each lag are listed in Table 5-3.

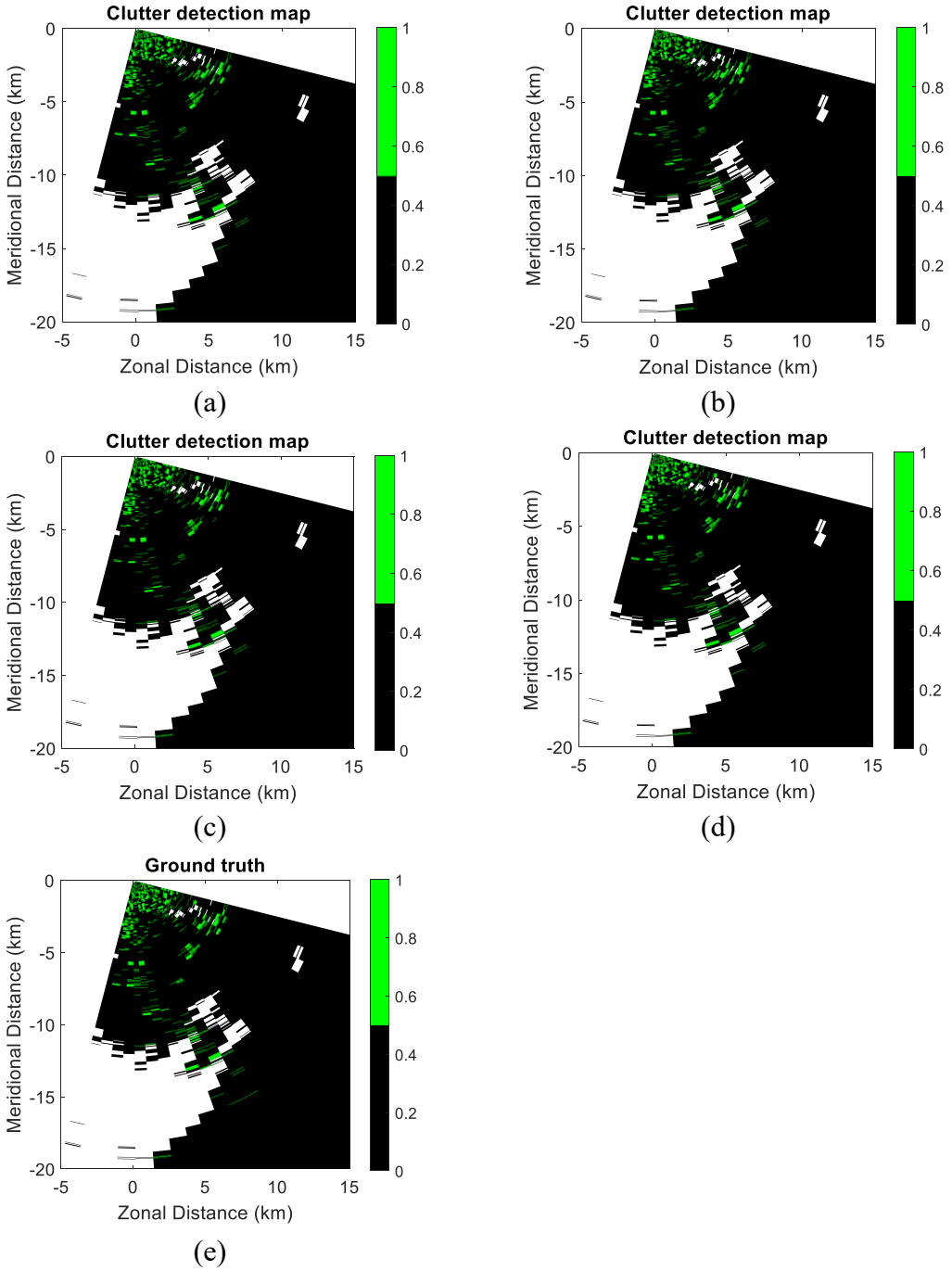

Figure 5-25 Detected clutter maps obtained using SBC with mechanical scan. (a) Lag=1. (b) Lag=2. (c) Lag=3. (d) Lag=4. (e) Ground truth clutter map.

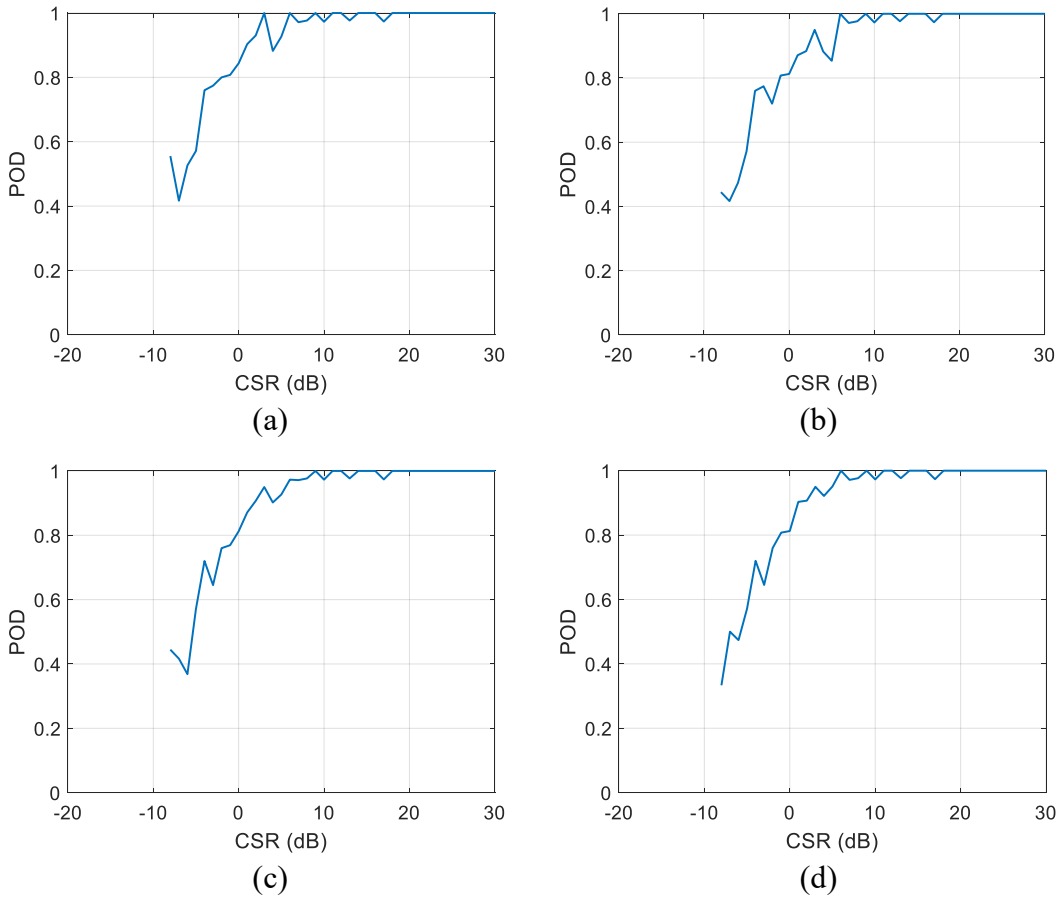

Figure 5-26 POD as a function of CSR with mechanical scan. (a) Lag=1. (b) Lag=2. (c) Lag=3. (d) Lag=4.

Table 5-3 The number of TP, FN, FP, TN, POD, PFA, and CSI at various lags with mechanical scan in convective precipitation

	TP	FN	FP	TN	POD	PFA	CSI
Lag 1	1149	76	36	21817	93.80%	0.16%	0.91
Lag 2	1136	89	33	21820	92.73%	0.15%	0.90
Lag 3	1133	92	24	21829	92.49%	0.11%	0.91
Lag 4	1140	85	23	21830	93.06%	0.11%	0.91

5.3.4.2 Stratiform precipitation

The pure clutter data collected with the CPPAR in the mechanical scan on 30 May 2020 are shown in Figure 5-27. The pure weather data from stratiform precipitation collected with the CPPAR in the mechanical scan on 25 May 2020 are shown in Figure 5-28. The combined data are shown in Figure 5-29. The scatter plots

of PSF_{h} and PSF_{v} at the lag of 1 to 4 for pure clutter data and pure weather data are shown in Figure 5-30.

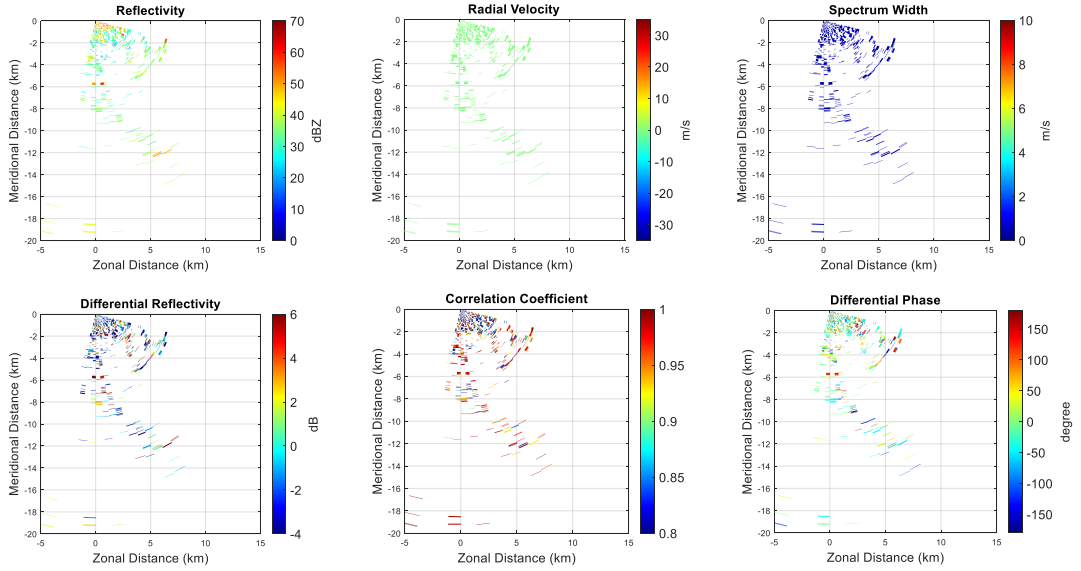

Figure 5-27 Clutter measurements with mechanical scan at 22:05:51 UTC on 30 May 2020.

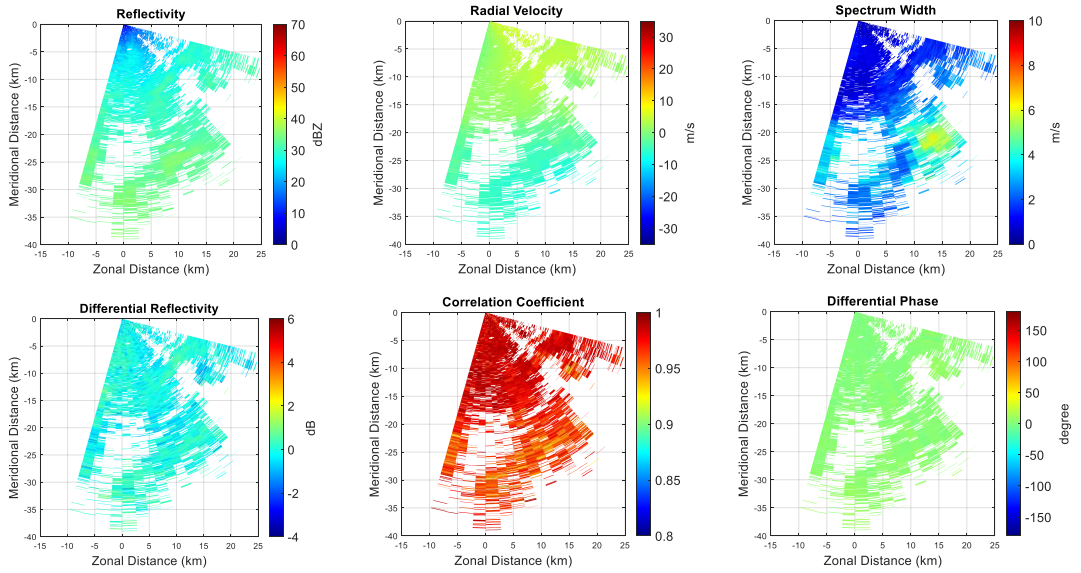

Figure 5-28 Weather measurements with mechanical scan at 20:35:51 UTC on 25 May 2020.

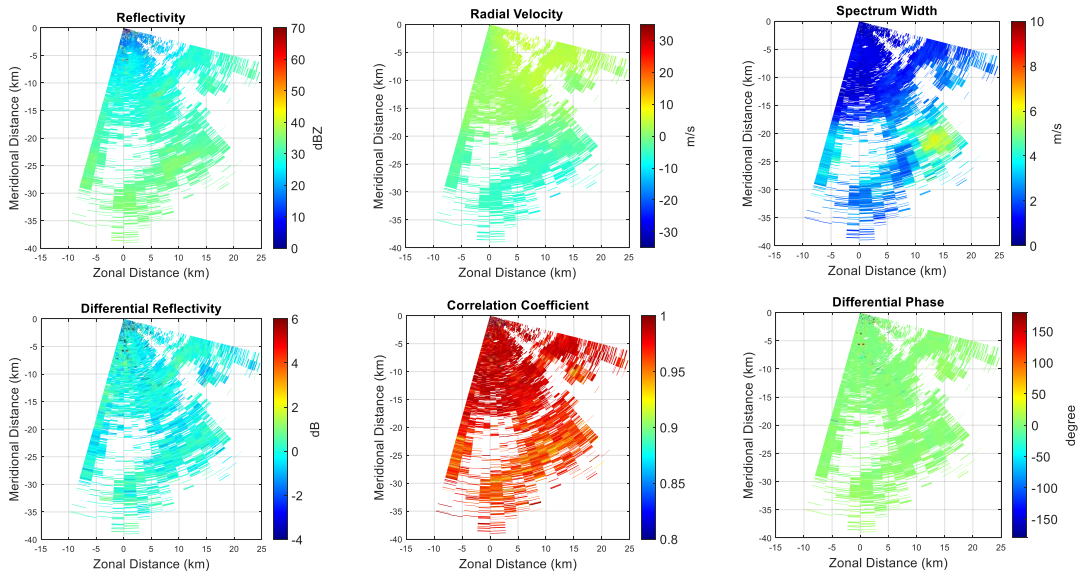

Figure 5-29 Combined clutter and weather measurements with mechanical scan.

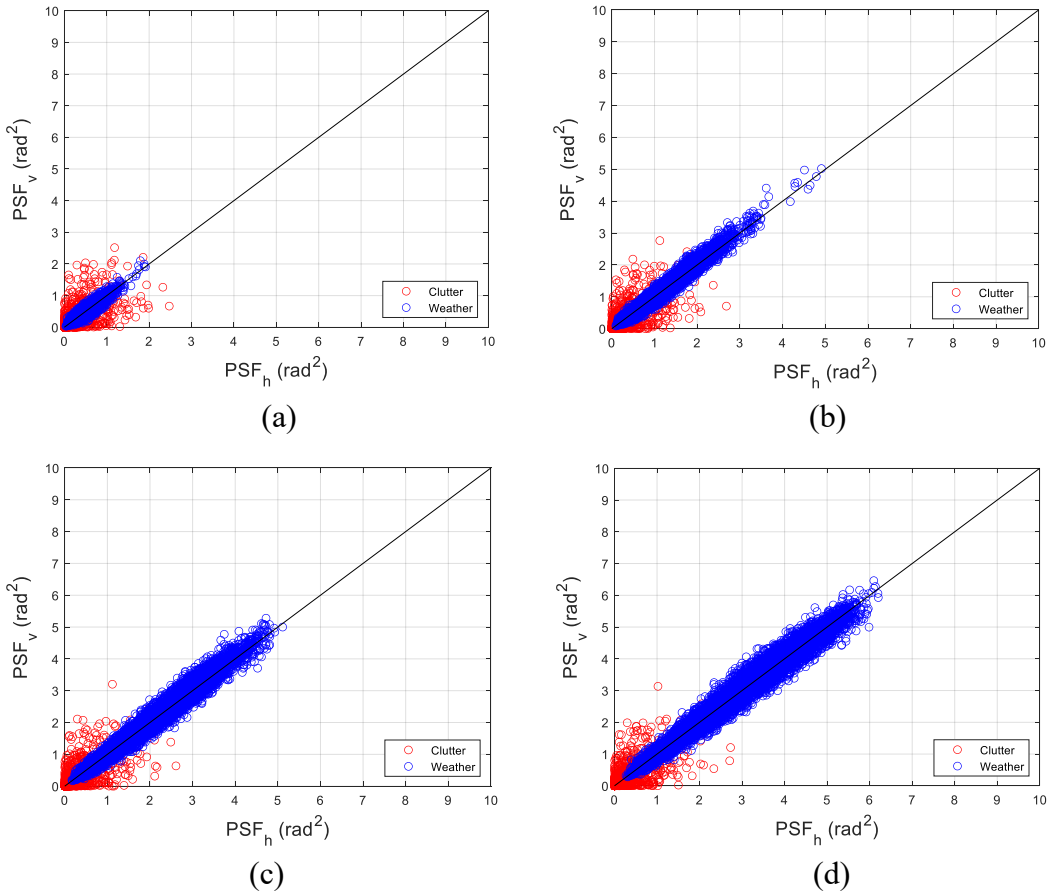

Figure 5-30 Scatter plots of PSF_h and PSF_v at multiple lags for the measurements in Figure 5-27 and Figure 5-28. (a) Lag=1. (b) Lag=2. (c) Lag=3. (d) Lag=4.

As shown in Figure 5-30, there is more overlap between weather and clutter in

case of PSF with lag=1. As a comparison, there is less overlap between weather and clutter in case of PSF with multiple lags.

The conditional probability density functions of $p(PSF_{\mathrm{h}}, PSF_{\mathrm{v}}|i)$ at various lags for clutter and weather are shown in Figure 5-31. The conditional probability density functions of $p(Z_{\mathrm{DR}}|i)$ and $p(\rho_{12}, \rho_{\mathrm{hv}}|i)$ for clutter and weather are shown in Figure 5-32.

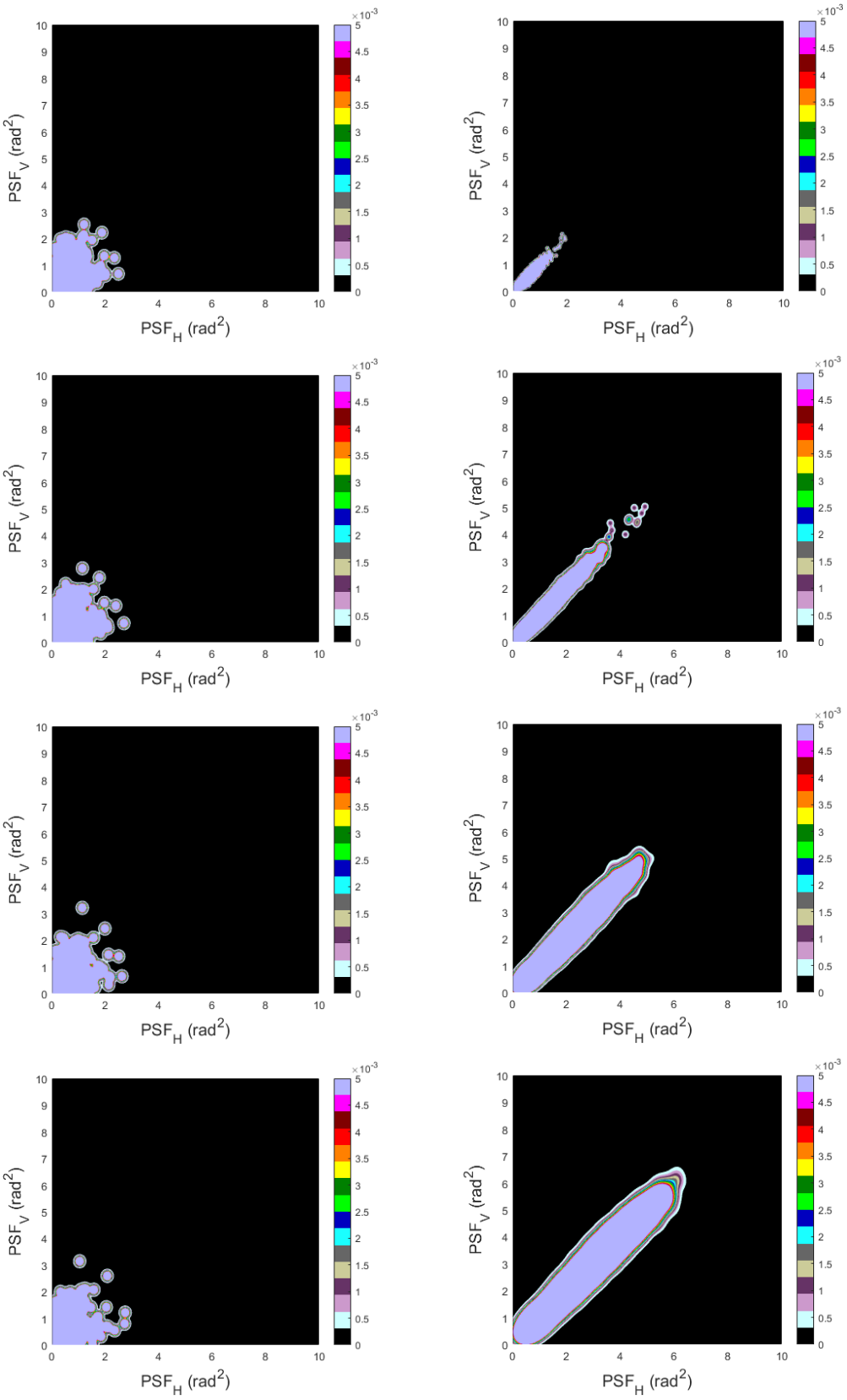

Figure 5-31 The joint conditional probability density functions of PSF_h and PSF_v given clutter (left column) and weather (right column) with mechanical scan. Figures from top to bottom rows refer to the lag of 1, 2, 3, and 4 respectively.

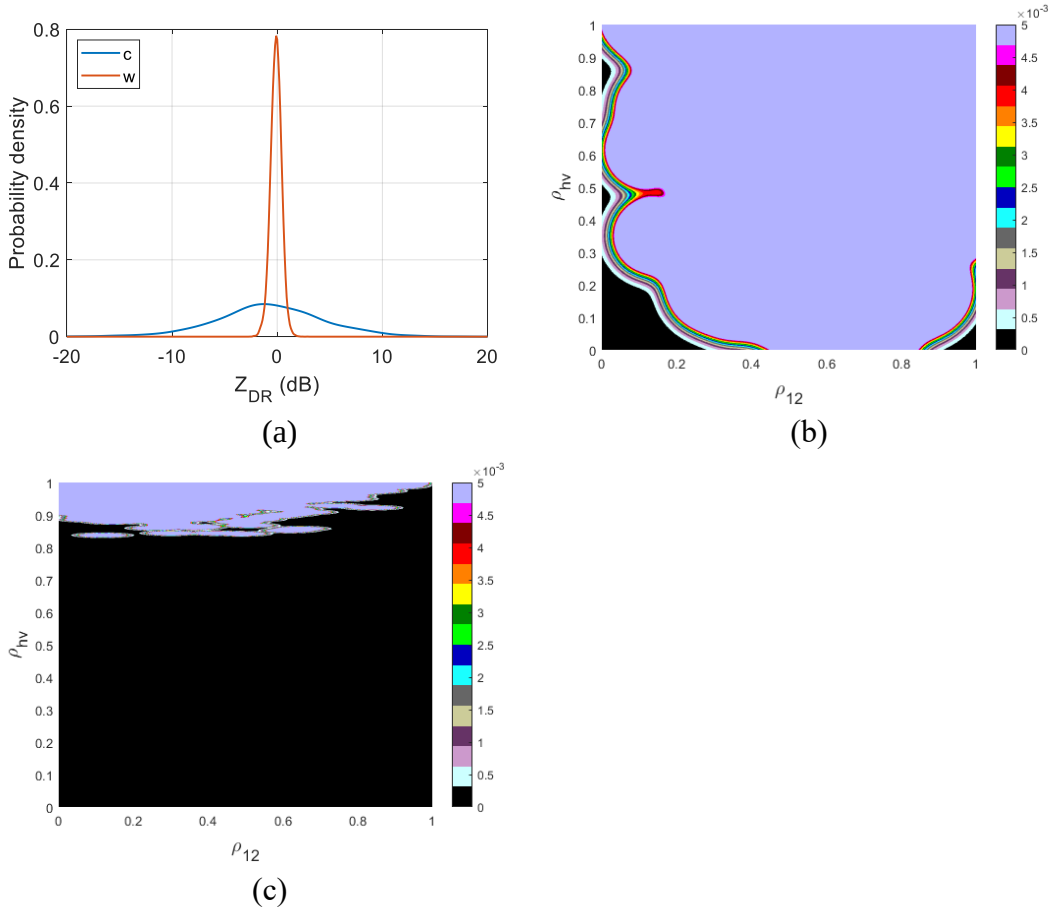

Figure 5-32 The conditional probability density functions with mechanical scan. (a) The conditional probability density function of Z_{DR} given clutter and weather. (b) The joint conditional probability density function of ρ_{12} and ρ_{hv} given clutter. (c) The joint conditional probability density function of ρ_{12} and ρ_{hv} given weather.

Figure 5-31 shows that as lag increases, the overlap between $p(PSF_{\mathrm{h}}, PSF_{\mathrm{v}}|c)$ and $p(PSF_{\mathrm{h}}, PSF_{\mathrm{v}}|w)$ reduces, which indicates that it is more likely to distinguish clutter from weather. On the other hand, the overlapped region is likely to be caused by narrow-band zero-velocity weather signals that have very similar properties as ground clutter. Figure 5-32 shows that both $p(Z_{\mathrm{DR}}|c)$ and $p(\rho_{12}, \rho_{\mathrm{hv}}|c)$ has a much larger spread than those for weather signals.

The SBC clutter detection maps of the controlled data set for PSF_{h} and PSF_{v} at various lags as well as the ground truth clutter map are shown in Figure 5-33. The number of TP, FN, FP, TN, POD, PFA, and CSI for each lag are listed in Table 5-4.

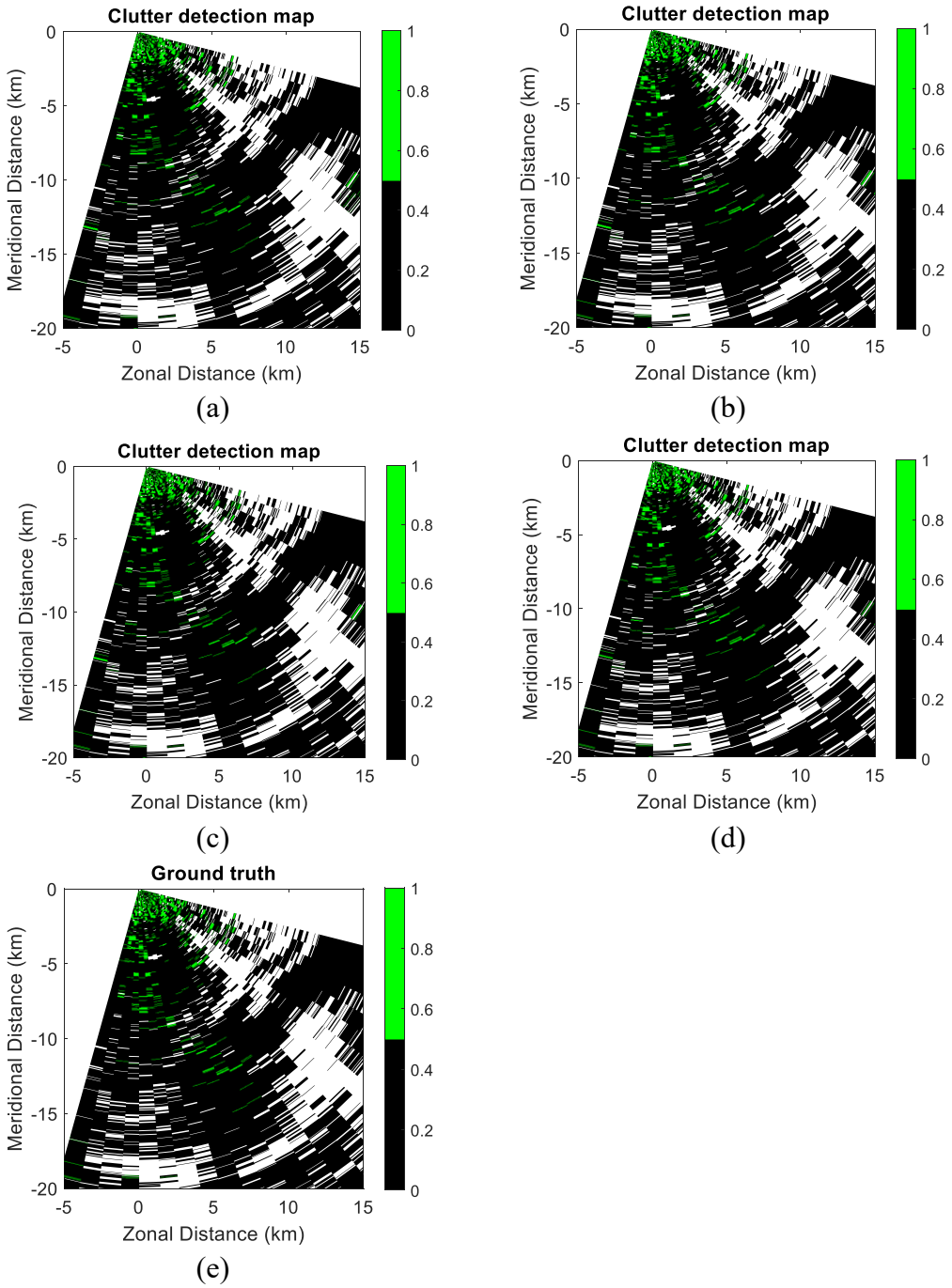

Figure 5-33 Detected clutter maps obtained using SBC with mechanical scan. (a) Lag=1. (b) Lag=2. (c) Lag=3. (d) Lag=4. (e) Ground truth clutter map.

Table 5-4 The number of TP, FN, FP, TN, POD, PFA, and CSI at various lags with mechanical scan in stratiform precipitation

	TP	FN	FP	TN	POD	PFA	CSI
Lag 1	1242	29	88	16317	97.72%	0.54%	0.91
Lag 2	1235	36	71	16334	97.17%	0.43%	0.92
Lag 3	1235	36	58	16347	97.17%	0.35%	0.93
Lag 4	1237	34	54	16351	97.32%	0.33%	0.93

Table 5-4 shows that clutter detection performance in stratiform precipitation becomes better as the number of lags increase, because more lags will have larger phase change, which is helpful for PSF_{h} and PSF_{v} to discriminate between weather and clutter. It validates that multi-lag PSF_{h} and PSF_{v} are more effective in clutter detection for stratiform precipitation.

In addition, by comparison of Table 5-2 and Table 5-4, it can be found that the mechanical scan has higher POD and CSI as well as lower PFA than the corresponding electronic scan. This is likely caused by the clutter feature in electronic scan where clutter has similarly high ρ_{hv} as weather returns and hence imposes difficulties in clutter detection. In future work, more study is needed for various weather conditions and clutter types.

It should be noted that all the statistics presented in Table 5-1 to Table 5-4 are based on controlled dataset. If a test data set from a different weather scenario is used, then the clutter detection performance is expected to reduce a little bit because of the difference in PDF between the test data set and the controlled data set.

Chapter 6 Conclusions and Future Work

6.1 Conclusions

In this dissertation, initial weather measurements using a CPPAR demonstrator developed at the University of Oklahoma are presented to show the performance and polarimetric data quality that could be achieved by a cylindrical polarimetric array radar. The system specifications and field tests of the CPPAR demonstrator are introduced, including system overview, waveform design and verification, pattern optimization and far-field tests. Besides, three methods of system calibration are described and compared, including calibration with an external source, calibration with single beam weather measurements, and calibration with ground clutter. It is found that calibration with single beam weather measurements has the best performance and it is applied on the CPPAR demonstrator for the first time, which improves the beam-to-beam consistency and radar data quality in commutating beam electronic scan by minimizing gain and beamwidth variations.

To evaluate the CPPAR performance, an end-to-end phased array radar system simulator is developed. The simulation framework, weather returns modeling, antenna pattern, and channel electronics are introduced. Simulation results of uniform weather truth fields and convective precipitation with CPPAR and TPD are provided and compared. Then, actual weather measurements of several convective precipitation cases and a stratiform precipitation case made by the CPPAR demonstrator, with single beam mechanical scan and commutating beam electronic scan are presented. The measurements are first compared qualitatively with KTLX, and then the two scan

modes of the CPPAR are compared quantitatively, from which error statistics are derived and discussed. Both simulation and weather measurements show the CPPAR's scan-invariant beam characteristics in azimuth and polarization purity, which simplifies the calibration and allows high quality polarimetric weather measurements. Moreover, a theoretical explanation of features of commutating beam electronic scan in clutter detection that is different from mechanical scan is presented and verified by observations in a clear air condition with the CPPAR. Furthermore, clutter detection with the CPPAR based on multi-lag phase structure function, dual-scan cross-correlation coefficient, copolar correlation coefficient, and differential reflectivity in both electronic scan and mechanical scan modes are provided, which are especially effective in stratiform precipitation.

The contributions of the work presented in this dissertation are summarized as below. First of all, three system calibration methods are applied on the CPPAR demonstrator, which take both antenna pattern and channel electronics into account. Especially, the calibraion using single beam weather measurements has effectively improved the beam-to-beam consistency and radar data quality in commutating beam electronic scan by minimizing gain and beamwidth variations, which can be employed in other polarimetric phased array radars. Second, in PASIM, ρ_{hv} reduction is taken into account in the weather returns modeling for the first time, which considers the random scattering phase difference that causes decorrelation in the case of melting snow, hail, and distributed ground clutter. Third, the system gain of the CPPAR is estimated using a novel method based on noise power measurement, which proves to

be effective. In addition, the concepts of global standard deviation and local standard deviation are put forward to differentiate between the sampling error from random fluctuation and the error from the inhomogeneity of weather scatterers due to temporal and spatial difference of two scans. These concepts can be used in the error analysis of weather radar measurements. Fourth, a theoretical explanation of a feature of the commutating beam electronic scan in clutter detection that is different from mechanical scan is presented and verified by measurements in clear air conditions with the CPPAR for the first time. Also, clutter detection results based on multi-lag phase structure function are provided and prove to be effective in stratiform precipitation.

6.2 Future Work

Currently, efforts are underway to improve the calibration for the commutating beam electronic scan mode by enhancing the beam-to-beam stability and minimizing gain and beamwidth variations. Besides, advanced signal processing such as multi-lag correlation estimators will be implemented in CPPAR to further improve the polarimetric radar data quality.

On the other hand, to improve the fidelity of PASIM, better modeling of beam and channel mismatch between horizontal and vertical polarizations is being developed. In addition, optimized NLFM waveform and super-resolution algorithm may be implemented in simulations first. Further, to characterize the microphysical properties of precipitation, more realistic drop size distribution model such as Gamma distribution may be included in weather returns simulation. Further validation of PASIM using more measured weather data under various weather scenarios will be investigated.

For clutter detection, when scanning with multiple elevations is activated, weather measurement can be obtained in stratiform and convective precipitation at higher elevation angles with less clutter effects. As a result, the collected weather data will include both narrow-band zero-velocity weather signals and non-zero velocity weather signals, which will be more realistic and effective to evaluate the performance of clutter detection algorithms in electronic scan.

References

[1] R. J. Doviak and D. S. Zrnić, *Doppler Radar and Weather Observations*. 2nd ed. New York: Academic, 1993. Reprinted by Dover publications, 2006.

[2] G. Zhang, *Weather Radar Polarimetry*. Boca Raton: CRC Press, 2016.

[3] A. V. Ryzhkov and D. S. Zrnić. *Radar Polarimetry for Weather Observations*. Basel: Springer, 2019.

[4] V. N. Bringi and V. Chandrasekar, *Polarimetric Doppler Weather Radar*: *Principles and Applications*. Cambridge University Press, 2001.

[5] T. A. Seliga, and V. N. Bringi, "Potential use of radar differential reflectivity measurements at orthogonal polarizations for measuring precipitation," *J. Appl. Meteor.*, vol. 15, no.1, pp. 69-76, Jan. 1976.

[6] T. A. Seliga, V. N. Bringi, and H. H. Al-Khatib, "Differential reflectivity measurements in rain: First experiments," *IEEE Trans. Geosci. Remote Sens.*, vol. 17, no.4, 240 – 244, Oct. 1979.

[7] D. S. Zrnić, and A. V. Ryzhkov, "Polarimetry for weather surveillance radars," *Bull. Amer. Meteor. Soc.*, vol. 80, no.3, pp. 389-406, Mar. 1999.

[8] G. Zhang, *et al.*, "Current status and future challenges of weather radar polarimetry: bridging the gap between radar meteorology/hydrology/engineering and numerical weather prediction," *Adv. Atmos. Sci.*, vol. 36, pp. 571-588, Jun. 2019.

[9] R. J. Doviak, V. Bringi, A. Ryzhkov, A. Zahrai, and D. S. Zrnić, "Considerations for polarimetric upgrades to operational WSR-88D radars," *J. Atmos. Oceanic Technol.*, vol. 17, no.3, pp. 257-278, Mar. 2000.

[10] H. B. Bluestein, *et al.*, "Radar in atmospheric sciences and related research: current systems, emerging technology, and future needs," *Bull. Amer. Meteor. Soc.*, vol. 95, no.12, pp. 1850-1861, Dec. 2014.

[11] M. E. Weber, J. Y. N. Cho, J. S. Herd, J. M. Flavin, W. E. Benner, and G. S. Torok, "The next-generation multimission U.S. surveillance radar network," *Bull. Amer. Meteor. Soc.*, vol. 88, no.11, pp. 1739-1752, Nov. 2007.

[12] D. S. Zrnić, *et al.*, "Agile-beam phased array radar for weather observations," *Bull. Amer. Meteor. Soc.*, vol. 88, no.11, pp. 1753-1766, Nov. 2007.

[13] P. L. Heinselman, and S. M. Torres, "High-temporal-resolution capabilities of the national weather radar testbed phased-array radar," *J. Appl. Meteor. Climatol.*, vol. 50, no.3, pp. 579-593, Mar. 2011.

[14] P. L. Heinselman, D. L. Priegnitz, K. L. Manross, T. M. Smith, and R. W. Adams, "Rapid sampling of severe storms by the national weather radar testbed phased array radar," *Wea. Forecasting*, vol. 23, no.5, pp. 808-824, Oct. 2008.

[15] J. E. Stailey, and K. D. Hondl, "Multifunction phased array radar for aircraft and weather surveillance," *Proc. IEEE*, vol. 104, no. 3, pp. 649 – 659, Mar. 2016.

[16] G. Zhang, R. J. Doviak, D. S. Zrnić, J. Crain, D. Staiman, and Y. Al-Rashid, "Phased array radar polarimetry for weather sensing: A theoretical formulation for

bias corrections," *IEEE Trans. Geosci. Remote Sens.*, vol. 47, no.11, pp. 3679–3689, Nov. 2009.

[17] A. P. Hopf, *et al.*, "CASA phased array radar system description, simulation and products," in *Proc. IEEE Int. Geosci. Remote Sens. Symp. (IGARSS)*, Cape Town, South Africa, Jul. 2009, pp. 968–971.

[18] J. L. Salazar, E. J. Knapp, and D. J. McLaughlin, "Dual-polarization performance of the phase-tilt antenna array in a casa dense network radar," in *Proc. IEEE Int. Geosci. Remote Sens. Symp. (IGARSS)*, Honolulu, HI, USA, Jul. 2010, pp. 3470–3473.

[19] H. Kikuchi, E. Yoshikawa, T. Ushio, F. Mizutani, and M. Wada, "Application of adaptive digital beamforming to Osaka university phased array weather radar," *IEEE Trans. Geosci. Remote Sens.*, vol. 55, no.7, pp. 3875–3884, Jul. 2017.

[20] I. R. Ivić and A. D. Byrd, "A first look at the MPAR dual-polarization phased-array-radar mobile demonstrator," in *Proc. 37th Conf. Radar Meteorol.*, Norman, OK, USA, Sep. 2015.

[21] I. R. Ivić, *et al.*, "An overview of weather calibration for the Advanced Technology Demonstrator," in *Proc. IEEE Int. Symp. Phased Array Syst. Technol.*, Waltham, MA, USA, Oct. 2019, pp. 1–7.

[22] G. Zhang, R. J. Doviak, D. S. Zrnić, R. D. Palmer, L. Lei, and Y. Al-Rashid, "Polarimetric phased-array radar for weather measurement: a planar or cylindrical configuration?" *J. Atmos. Ocean. Technol.*, vol. 28, pp. 63–72, Jan. 2011.

[23] D. S. Zrnić, G. Zhang, and R. J. Doviak, "Bias correction and Doppler measurement for polarimetric phased-array radar," *IEEE Trans. Geosci. Remote Sens.*, vol. 49, no. 2, pp. 843–853, Feb. 2011.

[24] R. J. Doviak, L. Lei, G. Zhang, J. Meier, and C. Curtis, "Comparing theory and measurements of cross-polar fields of a phased-array weather radar," *IEEE Geosci. Remote Sens. Lett.*, vol. 8, no. 5, pp. 1002–1006, Sep. 2011.

[25] L. Lei, G. Zhang, R. J. Doviak, and S. Karimkashi, "Comparison of theoretical biases in estimating polarimetric properties of precipitation with weather radar using parabolic reflector, or planar and cylindrical arrays," *IEEE Trans. Geosci. Remote Sens.*, vol. 53, no. 8, pp. 4313–4327, Aug. 2015.

[26] Y. Wang, and V. Chandrasekar, "Polarization isolation requirements for linear dual-polarization weather radar in simultaneous transmission mode of operation," *IEEE Trans.Geosci. Remote Sens.*, vol.44, no. 8, pp. 2019–2028, Aug. 2006.

[27] L. Lei, "Theoretical analysis and bias correction for planar and cylindrical polarimetric phased array weather radar," Ph.D. dissertation, School Elect. Comput. Eng., Univ. Oklahoma, Norman, OK, USA, 2014.

[28] L. Borowska, D. S. Zrnić, Y. Zhang, G. Zhang, J. Jackson, and C. Davis. (2018). "Weather observations with the Omni Directional Weapon Location (OWL) Radar." NOAA Nat. Severe Storms Lab., Norman, OK, USA. Tech. Rep., p. 14.

[29] S. Karimkashi, and G. Zhang, "A dual-polarized series-fed microstrip antenna array with very high polarization purity for weather measurements," *IEEE Trans. Antennas Propag.,* vol. 61, no. 10, pp. 5315-5319. Oct. 2013.

[30] C. Fulton, *et al.,* "Cylindrical polarimetric phased array radar: beamforming and calibration for weather applications," *IEEE Trans. Geosci. Remote Sens.*, vol. 55, no. 5, pp. 2827–2841, May 2017.

[31] A. Byrd, C. Fulton, R. Palmer, S. Islam, D. Zrnić, R. Doviak, R.Zhang, and G. Zhang. (2017). "First weather observations with a cylindrical polarimetric phased array radar." University of Oklahoma, Norman, OK, USA. Internal Technical Report.

[32] H. Saeidi-Manesh, M. Mirmozafari, and G. Zhang, "Low cross-polarisation high-isolation frequency scanning aperture coupled microstrip patch antenna array with matched dual-polarisation radiation patterns," *Electron. Lett.*, vol. 53, no. 14, pp. 901–902, Jul. 2017.

[33] J. M. Kurdzo, B. L. Cheong, R. D. Palmer, G. Zhang, and J. B. Meier, "A pulse compression waveform for improved-sensitivity weather radar observations," *J. Atmos. Ocean. Technol.*, vol. 31, no. 12, pp. 2713–2731, Dec. 2014.

[34] M.-H. Golbon-Haghighi, H. Saeidi-Manesh, G. Zhang, and Y. Zhang, "Pattern synthesis for the cylindrical polarimetric phased array radar (CPPAR)," *Prog. Electromagn. Res. M*, vol. 66, pp. 87–98, Mar. 2018.

[35] D. S. Zrnić, R. J. Doviak, G. Zhang, and A. V. Ryzhkov, "Bias in differential reflectivity due to cross coupling through the radiation patterns of polarimetric weather radars," *J. Atmos. Ocean. Technol.*, vol. 27, no. 10, pp. 1624–1637, Oct. 2010.

[36] D. S. Zrnić, "Simulation of weatherlike Doppler spectra and signals," *J. Appl. Meteorol.*, vol. 14, no. 4, pp. 619–620, Jun. 1975.

[37] G. Galati and G. Pavan, "Computer simulation of weather radar signals," *Simul. Pract. Theory*, vol. 3, no. 1, pp. 17–44, Jul. 1995.

[38] S. M. Torres, "Estimation of Doppler and polarimetric variables for weather radars," Ph.D. dissertation, School Elect. Comput. Eng., Univ. Oklahoma, Norman, OK, USA, 2001.

[39] B. L. Cheong,; R. D. Palmer, and M. Xue, "A time series weather radar simulator based on high-resolution atmospheric models," *J. Atmos. Ocean. Technol.*, vol. 25, no. 2, pp. 230–243, Feb. 2008.

[40] A. D. Byrd, I. R. Ivić, R. D. Palmer, B. M. Isom, B. L. Cheong, A. D. Schenkman, and M. Xue, "A weather radar simulator for the evaluation of polarimetric phased array performance," *IEEE Trans. Geosci. Remote Sens.*, vol. 54, no. 7, pp. 4178–4189, Jul. 2016.

[41] I. R. Ivić, "An approach to simulate the effects of antenna patterns on polarimetric variable estimates," *J. Atmos. Ocean. Technol.*, vol. 34, no. 9, pp. 1907–1934, Sep. 2017.

[42] E. Barcaroli, A. Lupidi, L. Facheris, F. Cuccoli, H. Chen, and V. Chandrasekar, "A validation procedure for a polarimetric weather radar signal simulator," *IEEE Trans. Geosci. Remote Sens.*, vol. 57, no. 1, pp. 609–622, Jan. 2019.

[43] D. Schvartzman, and C.D.Curtis, "Signal processing and radar characteristics (SPARC) simulator: a flexible dual-polarization weather-radar signal simulation framework based on preexisting radar-variable data," *IEEE J. Sel. Topics Appl. Earth Observ. Remote Sens.*, vol. 12, no. 1, pp. 135–150, Jan. 2019.

[44] S. Wang, "Waveform and transceiver optimization for multi-functional airborne radar through adaptive processing," Ph.D. dissertation, School Elect. Comput. Eng., Univ. Oklahoma, Norman, OK, USA, 2013.

[45] C. G. Tua, T. Pratt, and A. I. Zaghloul, "A study of interpulse instability in gallium nitride power amplifiers in multifunction radars," *IEEE Trans. Microw. Theory Techn.*, vol. 64, no. 11, pp. 3732–3747, Nov. 2016.

[46] Z. Li, S. Perera, Y. Zhang, G. Zhang, and R. J. Doviak, "Time-domain system modeling and applications for multi-function array radar weather measurements," in *Proc. IEEE Radar Conf. (RadarCon)*, Oklahoma City, OK, USA, Apr. 2018, pp. 1049–1054.

[47] Z. Li, S. Perera, Y. Zhang, G. Zhang, and R. J. Doviak, "Phased-array radar system simulator (PASIM): development and simulation result assessment," *Remote Sens.*, vol. 11, no. 4, pp. 1–22, Feb. 2019.

[48] Z. Li, S. Perera, Y. Zhang, G. Zhang, R. J. Doviak, and I. Ivić, "Evaluation of the impacts of system modules on polarimetric radar data quality using a phased array weather radar system simulator," in *Proc. IEEE Int. Symp. Phased Array Syst. Technol.*, Waltham, MA, USA, Oct. 2019, pp. 1–5.

[49] H. Chen, and R. Gentile, "Phased array system simulation," in *IEEE Int. Symposium on Phased Array Systems and Technology (PAST)*, Waltham, MA, USA, Oct. 2016.

[50] R. Nepal, Y. Zhang, and W. Blake, "Sense and avoid airborne radar implementations on a low-cost weather radar platform," *Aerospace*, vol. 4, no. 1, pp. 1–18, Mar. 2017.

[51] J. J. Helmus, and S. M. Collis, "The Python ARM Radar Toolkit (Py-ART), a library for working with weather radar data in the Python programming language," *J. Open Res. Softw.*, vol. 4, no. 1, pp. e25, Jul. 2016.

[52] M. Heistermann, *et al.*, "The emergence of open-source software for the weather radar community," *Bull. Amer. Meteor. Soc.*, vol. 96, no. 1, pp. 117–128, Jan. 2015.

[53] H. Meikle, *Modern Radar Systems*. 2nd ed. Norwood: Artech House, 2008.

[54] A. A. M. Saleh, "Frequency-independent and frequency-dependent nonlinear models of TWT amplifiers," *IEEE Trans. Commun.*, vol. 29, no. 11, pp. 1715–1720, Nov. 1981.

[55] Z. Li, Y. Zhang, L. Borowska, *et al.*, "Polarimetric phased array weather radar data quality evaluation through combined analysis, simulation, and measurements," *IEEE Geosci. Remote Sens. Lett.*, doi: 10.1109/LGRS.2020.2990334.

[56] D. Mirković and D. S. Zrnić. (2019). "Computational electromagnetic tools applied to the polarimetric phased array antenna." NOAA Nat. Severe Storms Lab., Norman, OK, USA. Tech. Rep., p. 42.

[57] V. M. Melnikov and D. S. Zrnić, "Autocorrelation and cross-correlation estimators of polarimetric variables," *J. Atmos. Ocean. Technol.*, vol. 24, no. 8, pp. 1337–1350, Aug. 2007.

[58] D. S. Zrnić and R. J. Doviak. (2005). "System Requirements for Phased Array Weather Radar." NOAA Nat. Severe Storms Lab., Norman, OK, USA. Tech. Rep., p. 24.

[59] V. M. Melnikov. (2004). "Simultaneous Transmission Mode for the Polarimetric WSR-88D." NOAA Nat. Severe Storms Lab., Norman, OK, USA. Tech. Rep., p. 84.

[60] Z. Li, G. Zhang, M.-H. Golbon-Haghighi, H. Saeidi-Manesh, M. Herndon, and H. Pan, "Initial observations with electronic and mechanical scans using a cylindrical polarimetric phased array radar," *IEEE Geosci. Remote Sens. Lett.*, doi: 10.1109/LGRS.2020.2971471.

[61] Z. Li and G. Zhang, "Weather measurements using a cylindrical polarimetric phased array radar," in *Proc. 39th Int. Conf. Radar Meteorol.*, Nara, Japan, Sep. 2019.

[62] Q. Cao, G. Zhang, R. D. Palmer, M. Knight, R. May, and R. J. Stafford, "Spectrum-time estimation and processing (STEP) for improving weather radar data quality," *IEEE Trans. Geosci. Remote Sens.*, vol. 50, no. 11, pp. 4670–4683, Nov. 2012.

[63] H. L.Groginsky and K. M. Glover, "Weather radar canceller design," in *Proc. 19th Conf. Radar Meteorol.*, Miami Beach, FL, USA, Apr. 1980.

[64] A. D. Siggia and R. E. Passarelli, "Gaussian model adaptive processing (GMAP) for improved ground clutter cancellation and moment calculation," in *Proc. 3rd Eur. Conf. Radar Meteorol. Hydrol. (ERAD)*, Visby, Sweden, Sep. 2004.

[65] P. Meischner, *Weather Radar: Principles and Advanced Applications*. New York: Springer, 2004.

[66] J. C. Hubbert, M. Dixon, S. M. Ellis, and G. Meymaris, "Weather radar ground clutter. Part I: Identification, modeling, and simulation," *J. Atmos. Ocean. Technol.*, vol. 26, no. 7, pp. 1165–1180, Jul. 2009.

[67] J. C. Hubbert, M. Dixon, and S. M. Ellis, "Weather radar ground clutter. Part II: Real-time identification and filtering," *J. Atmos. Ocean. Technol.*, vol. 26, no. 7, pp. 1181–1197, Jul. 2009.

[68] S. M. Torres and D. A. Warde, "Ground clutter mitigation for weather radars using the autocorrelation spectral density," *J. Atmos. Ocean. Technol.*, vol. 31, no. 10, pp. 2049–2066, Oct. 2014.

[69] D. A. Warde and S. M. Torres, "The autocorrelation spectral density for Doppler-weather-radar signal analysis," *IEEE Trans. Geosci. Remote Sens.*, vol. 52, no. 1, pp. 508–518, Jan. 2014.

[70] Y. Li, G. Zhang, and R. J. Doivak, "Ground clutter detection using the statistical properties of signals received with a polarimetric radar," *IEEE Trans. Signal Process.*, vol. 62, no. 3, pp. 597–606, Feb. 2014.

[71] Y. Li, G. Zhang, R. J. Doivak, L. Lei, and Q. Cao, "A new approach to detect ground clutter mixed with weather signals," *IEEE Trans. Geosci. Remote Sens.*, vol. 51, no. 4, pp. 2373–2387, Apr. 2013.

[72] M.-H. Golbon-Haghighi, G. Zhang, and R. J. Doivak, "Ground clutter detection for weather radar using phase fluctuation index," *IEEE Trans. Geosci. Remote Sens.*, vol. 57, no. 5, pp. 2889–2895, May 2019.

[73] M.-H. Golbon-Haghighi and G. Zhang, "Detection of ground clutter for dual-polarization weather radar using a novel 3D discriminant function," *J. Atmos. Ocean. Technol.*, vol. 36, no. 7, pp. 1285–1296, Jul. 2019.

[74] A. Papoulis, *Probability, Random Variables, and Stochastic Processes*. New York: Mcgraw Hill College, 1991.

[75] J. Han, M. Kamber, and J. Pei, *Data Mining Concepts and Techniques*. 3rd ed. San Mateo, CA: Morgan Kaufmann, 2011.